Peculiar Flow Fields in the Zone of Avoidance from the Near-infrared Tully-Fisher relation

Khaled Said Ahmed Soliman

March 2017

A dissertation submitted in partial fulfillment of the requirements for the
degree of
Doctor of Philosophy
in
Astronomy
Department of Astronomy
UNIVERSITY OF CAPE TOWN

Supervisors: Profs. R. C. Kraan-Korteweg, T. H. Jarrett, and L. Staveley-Smith

Abstract

In this thesis, we investigate the flow field in and around the major large-scale structures in the southern Zone of Avoidance as derived from peculiar motions of galaxies. The peculiar velocities were derived from a galaxy sample based on the systematic deep Parkes H I Zone of Avoidance survey (HIZOA) using a newly optimized Near InfraRed (NIR) Tully-Fisher (TF) relation. The NIR imaging data of the HIZOA galaxies were obtained with the Infrared Survey Facility (IRSF) on the 1.4-m telescope at the South African Astronomical Observatory, which allows simultaneous three-colour (J, H, and K_s) imaging.

We first calibrate the NIR Tully-Fisher relation for isophotal magnitudes, using the same 888 calibrator galaxies that were used for the derivation of the 2MASS TF relation for total magnitudes. The isophotal NIR TF relation allows for a significant improvement in the scatter of low surface brightness galaxies, and galaxies obscured by dust. We also simulate the effect of dust extinction on the shape of galaxies and derive a correction model. We show the ability of this model to reproduce the intrinsic axial ratio from the observed parameters up to extinction levels of $A_V \sim 11$ mag.

We present new narrow-band H I 21-cm observations for 394 selected galaxies from the HIZOA survey with improved velocity resolution. These new observations with high resolution allow a robust measurement of five different types of linewidth. We used a Bayesian mixture model to derive conversion equations between these five widths, which will be used to combine data sets of differently-derived line-widths.

We present deep near-infrared (J, H, and K_s bands) observations of 1108 detections from the HIZOA survey. The average seeing, sky background and the isophotal magnitude errors are 1.38 arcsec, 20.1 mag, and 0.02 mag respectively, which are of sufficient accuracy for a Tully-Fisher analysis. Through comparisons with 2MASS and UKIDSS images we demonstrate the reliability of the IRSF photometry.

We use these data and the isophotal Tully-Fisher relation to measure distances and peculiar velocities for 287 galaxies, which covers the whole southern ZOA. We derive the H I mass function to make predictions for the Malmquist bias, thus enabling us to correct the measured distances accordingly. The slope of the H I mass function agrees with both HIPASS Bright Galaxy Catalog (BGC) and ALFALFA, whereas the characteristic H I mass aligns more closely with ALFALFA than the HIPASS BGC.

We map the velocity field around the major large-scale structures in the southern ZOA, such as the Great Attractor (GA), the Local Void (LV), and the Puppis region. In the GA region, we find a clear infall into the GA from both sides. Our analysis of the LV shows that the void galaxies are moving away from the center which confirms the recent results which show the draining of the LV. We also find outflow from the Puppis region.

We present comparisons between the velocity field derived in this thesis, the 2MASS Tully–Fisher observations (2MTF), the 2MASS Redshift Survey (2MRS), as well as the *IRAS* Point Source Catalog Redshift Survey (PSCz) reconstructions. We find good agreement at low redshift with the 2MTF observations, better than the 2MRS and the PSCz reconstructions. At high redshift, our results disagree with the 2MTF observations, the 2MRS, and the PSCz reconstructions.

Acknowledgments

I would like to acknowledge my supervisors, Prof. Renée C. Kraan-Korteweg, Prof. Tom Jarrett, and Prof. Lister Staveley-Smith for their help and support throughout my thesis.

I would like also to acknowledge many collaborators for their help and guidance, including Dr. Wendy Williams, Mpati Ramatsoku, and Dr. Chris Springob. I acknowledge the HIZOA survey team for early access to the data.

I am also grateful to my colleagues, astronomers, and staff in the Astronomy Department at UCT for making this so great environment for work.

Finally, I would like to thank my family for their unconditional love and support.

This work is based upon research supported by the Faculty of Science at the University of Cape Town, the ARC Centre of Excellence for All-sky Astrophysics, CAASTRO at the University of Western Australia through project number CE110001020, and the South African National Research Foundation and Department of Science and Technology.

This thesis makes use of data products from the Two Micron All Sky Survey, which is a joint project of the University of Massachusetts and the Infrared Processing and Analysis Center, funded by the National Aeronautics and Space Administration and the National Science Foundation.

Preface

This thesis is approved by the Doctoral Degrees Board Chair, Professor Visser and the Dean of Science Prof. La Roex to be submitted as a series of publications as follows:

Chapter 1: Is a review of the literature.

Chapter 2: Khaled Said, Renée C. Kraan-Korteweg and T. H. Jarrett, "NIR Tully-Fisher in the Zone of Avoidance. – I. On how to extend the NIR Tully Fisher relation to be truly all-sky," 2015, MNRAS, 447, 1618

This chapter has been published in the Monthly Notices of the Royal Astronomical Society Journal. In this chapter I simulate the effect of dust extinction on the geometrical properties of galaxies and derive correction models to reproduce the intrinsic axial ratio from the observed value. I also re-calibrate the Tully-Fisher relation to work in the Zone of Avoidance. I have done all the work and the write-up of this paper under the supervision of my supervisors.

Chapter 3: Khaled Said, Renée C. Kraan-Korteweg, Lister Staveley-Smith, Wendy L. Williams, T. H. Jarrett and Christopher M. Springob, NIR Tully-Fisher in the Zone of Avoidance. -– II. 21 cm H I-line spectra of southern ZOA galaxies., 2016, MNRAS, 457, 2366

This chapter has been published in the Monthly Notices of the Royal Astronomical Society Journal. In this chapter I present high-accuracy H I profiles and linewidths for inclined spiral galaxies in the southern Zone of Avoidance. These galaxies define a sample for use in the determinations of peculiar velocities using the near-infrared Tully–Fisher relation. This chapter contains radio observations of 394 galaxies in the southern zone of avoidance where I did the observations of 312 (80%) of them and the other 82 galaxies (20%) were observed by Dr. Wendy L. Williams, who is a co-author of this paper. All data reduction, calibration, analysis, and write-up were done by myself under the supervision of my supervisors.

Chapter 4: Khaled Said, Renée C. Kraan-Korteweg, T. H. Jarrett, Lister Staveley-Smith and Wendy L. Williams,"NIR Tully-Fisher in the Zone of Avoidance. – III. Deep NIR catalog of the HIZoA galaxies.," 2016, MNRAS, 462, 3386

This chapter has been published in the Monthly Notices of the Royal Astronomical Society Journal. In this chapter, I present a deep near-infrared photometric catalogue of sources from the Parkes HI Zone of Avoidance (HIZOA) survey, which forms the basis for an investigation of the matter distribution in the Zone of Avoidance. This chapter contains near-infrared observations of 1108 galaxies in the southern Zone of Avoidance. Half of these galaxies were previously observed and published by Williams, Kraan-Korteweg & Woudt (2014). I observed the other half and, for consistency, reduced the whole sample using the exact same method. The analysis and write-up were done by myself under the supervision of my supervisors.

Chapter 5: H I mass function and Peculiar velocities in the southern ZOA.

In this chapter, I derive the H I mass function of galaxies in the Zone of Avoidance which is required to calculate accurate distances to galaxies in the Zone of Avoidance. I use all the tools and data published in the previous chapters to calculate the the distances and peculiar velocities of galaxies in the Zone of Avoidance. I use these distances and peculiar velocities to describe the motion of galaxies around the major large-scale structures in the southern Zone of Avoidance. The work of this chapter is done by myself under the supervision of my supervisors.

Chapter 6: Conclusions and future work.

While all chapters are related, each chapter contains all the information to be read independently in a single sitting. We modified the introduction of each chapter to avoid any duplication.

Throughout this thesis we assume $H_0 = 75$ km s^{-1} Mpc^{-1}.

Plagiarism Declaration

I, Khaled Said, know the meaning of plagiarism and declare that all of the work in the document, save for that which is properly acknowledged, is my own.

Contents

List of Figures

List of Tables

Chapter 1

Introduction

1.1 Peculiar velocity fields

1.1.1 Theoretical Background

The Cosmological Principal states that matter on large scales is uniformly distributed in space. This means that the universe is homogeneous and isotropic. However, what the observers see today are galaxies that tend to accumulate in clustering patterns, creating the so-called cosmic web. Figure 1.1 shows the distribution of galaxies from the 2MASS extended source catalogue (Jarrett et al. 2000) with measured redshifts either from spectroscopic measurements or based on the 2MASS photometric determinations.

The current theoretical models for structure formation explain this being due to the gravitational instability of small perturbations in this uniform background, out of which over-dense regions formed and evolved with time. The gravity of these over-dense regions causes galaxies to deviate from the Hubble expansion. In linear perturbation theory these peculiar velocities are directly proportional to the gravitational acceleration and can be written in an integral form (Peebles 1980; 1993, Strauss & Willick 1995) as:

$$v(r) = \frac{f}{4\pi} \int d^3r' \delta(r') \frac{r' - r}{|r' - r|^3}, \tag{1.1}$$

where $v(r)$ is the peculiar velocity field, f is the growth rate of the perturbations, and $\delta(r)$ is the mass density contrast. Measuring distances in velocity

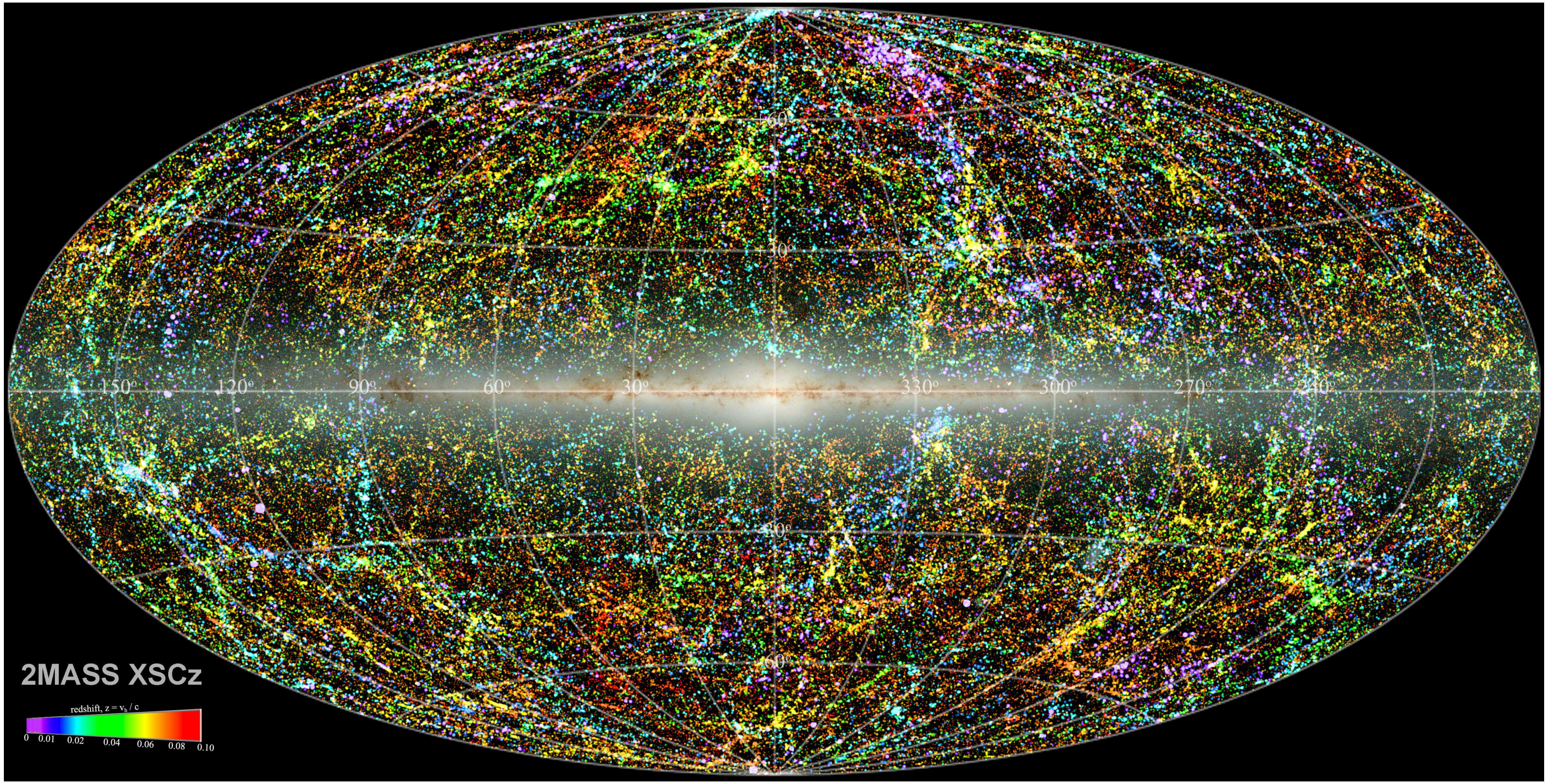

Figure 1.1: The distribution of 2MASS XSCz galaxy catalogue (Jarrett et al. 2000) shown in an Aitoff projection. Redshifts are either spectroscopic or photometric measurements. This image is created by Tom Jarrett.

units (km s^{-1}) makes this equation independent of the Hubble constant. The latter is still a source of uncertainty. The peculiar velocities, therefore can be used to measure the fluctuation of the mass itself and probe the dark matter distribution. Furthermore, they can be used to measure the growth rate of the perturbations.

In the next subsections, we will review the techniques that are used to measure peculiar velocities and will discuss results from some of the most recent peculiar velocity surveys.

1.1.2 Techniques of Measurement

The total radial observed velocity of a galaxy is a combination of the expansion velocity due to the Hubble expansion and the peculiar velocity induced by the fluctuations in the matter distribution. Distance indicators are the tools that measure the distance independent of redshift. Therefore, the Hubble velocity can be calculated and the difference between the total observed velocity and the Hubble velocity will be the peculiar velocity.

There are two types of distance indicators: primary distance indicator such as the Cepheid variable stars (Fernie 1969), and secondary distance indicators such as, the Tully-Fisher (TF) relation (Tully & Fisher 1977) and the Fundamental Plane (FP) relation (Djorgovski & Davis 1987). As the name of each method indicates, primary distance indicators do not require calibration from other methods, however, secondary distance indicators require a primary calibration. Although Cepheid variable stars give the most accurate measurements of distances, they become very faint beyond ~ 20 Mpc and other distance indicators have to be used. In this subsection, we do not intend to give a review on all distance indicators, instead we will focus only on TF and FP (for a comprehensive review, see Jacoby et al. 1992)

In the last few decades, the secondary distance indicators TF (Tully & Fisher 1977) for spirals and FP (Djorgovski & Davis 1987) for ellipticals have been adopted as the workhorses for the large peculiar velocity surveys in the nearby Universe ($v \leq 16000$) km s^{-1}. Type Ia supernovae (SNe Ia) is one of the very promising distance indicators (Turnbull et al. 2012) in the era of the

Large Synoptic Survey Telescope (LSST)*. Although only $\sim 10^3$ supernova have been discovered in the whole history, LSST will be able to discover $\sim 10^7$ during the first ten years of its survey (LSST Science Collaboration et al. 2009). At the moment, only TF and FP relations have proven their ability to measure peculiar velocities for thousands of galaxies. The main idea behind these relations is to have a correlation between two or three parameters, where one of them depends on distance and the other does not. Thus, the first application is to infer the distances from the relation, and subsequently the peculiar velocities.

During the Great Debate, the correlation between the observed rotational velocity and the absolute magnitude was used by Opik (1922) to prove that Andromeda was extragalactic. Almost half a century later, Balkowski et al. (1974) used a sample of spiral and irregular dwarf galaxies to describe the correlation between the line-width and the luminosity without applying it as a distance indicator. Soon after, Tully & Fisher (1977) used a sample of inclined spiral galaxies to describe this correlation as a linear relation and propose its use as a distance indicator. As an attempt to explain the origin of the TF relation, Aaronson et al. (1979) calibrated the TF relation using the near infrared $H-$band ($1.6\mu m$) because it is more sensitive to the old stellar population, and therefore more consistent with the equation of the centrifugal equilibrium than the original $B-$band TF.

This correlation got the attention of the cosmology community due to its relatively low scatter, especially after the advent of the CCD detectors ($0.1-0.3$ mag, e.g., Pierce & Tully 1988, Willick 1990, Courteau et al. 1993, Bernstein et al. 1994). Since then, this relation has been used widely to carry out large peculiar velocity surveys for spiral galaxies in the nearby universe with errors ($\sim 15-20\%$), such as the Spiral Field and Cluster I-band TF (SFI++; Masters et al. 2006, Springob et al. 2007), Cosmic Flows (Tully et al. 2009, Courtois et al. 2011), and the 2MASS Tully-Fisher Survey (2MTF: Masters et al. 2008, Hong et al. 2013; 2014, Masters et al. 2014, Springob et al. 2016).

Almost 40 years since the discovery of this relation, and the nature origin (Silk 1997, Avila-Reese et al. 1998), the curvature at high mass end (Aaronson et al. 1986, Neill et al. 2014), and the deviation of the dwarf galaxies from

---

[*] https://www.lsst.org/

the TF relation (Kraan-Korteweg et al. 1988, Zwaan et al. 1995, Pierini 1999, van den Bosch 2000, O'Neil et al. 2000, McGaugh et al. 2000, Verheijen 2001, Kannappan et al. 2002, McGaugh 2005, Courteau et al. 2007, Karachentsev et al. 2016) are still being debated.

On the other hand, a correlation between luminosity and rms dispersion velocity for elliptical galaxies (they do not rotate) was proposed by Faber & Jackson (1976). This relation did not look as a promising distance indicator due to its huge scatter (almost twice the TF scatter). However, Djorgovski & Davis (1987) and Dressler et al. (1987) independently showed that adding a third parameter to this correlation will reduce the scatter, hence improve the relation. This Fundamental Plane (FP) relation describes the correlation between the luminosity, velocity dispersion, and the half-light radius of an elliptical galaxy (for a review of this early results see Kormendy & Djorgovski 1989). The relation was explained by Faber et al. (1987) through the virial relation. However, Colless et al. (2001) found that the FP deviates from the virial equilibrium. After the advent of integral field spectroscopy, Cappellari et al. (2013) gave a precise determination of the FP relation and called the deviation from the viral relation the tilt of the FP. Although we have more TF spiral galaxies in the nearby universe, FP surveys for elliptical galaxies tend to probe deeper in redshift. Therefore, the FP relation was used in the peculiar velocity surveys with errors ($\sim 20-30\%$) such as, the 2dF Galaxy Redshift Survey (2dFGRS; Colless et al. 2001), and the 6dF Galaxy Survey (6dFGS; Magoulas et al. 2012, Campbell et al. 2014, Springob et al. 2014, Scrimgeour et al. 2016).

In the coming subsection, we will highlight the main results from the most recent TF and FP distances and peculiar velocities surveys.

1.1.3 Recent Studies

Given that we can not review each and every piece of work in the peculiar velocity field in just a few lines, instead we will give a quick review of only the most recent results in the field of peculiar velocity surveys.

One of the largest TF surveys available to date is the *I*-band (SFI++) survey (Springob et al. 2007), which uses both cluster and field galaxies. Because of its selection in the *I*-band, it is heavily affected by dust extinction and incomplete across the Galactic plane ($|b| < 15^\circ$). The Two Micron All-Sky Survey (2MASS; Skrutskie et al. 2006) Tully-Fisher Survey (2MTF; Masters et al. 2008, Hong et al. 2013, Masters et al. 2014, Hong et al. 2014) provides a complete Tully-Fisher analysis (*i.e.* distance and peculiar velocity) of all bright inclined spirals in the 2MASS Redshift Survey (2MRS; Huchra et al. 2012). Masters et al. (2008) started the survey by using 2MASX photometry (Jarrett et al. 2000) in the J, H, and K_s bands of 888 spiral galaxies to calibrate the TF relation. In two companion papers Hong et al. (2013) present new H I 21-cm observations of 303 southern galaxies using the Parkes telescope, and Masters et al. (2014) present H I 21-cm observations for 1194 northern galaxies using the Green Bank telescope. These new H I observations and the calibrated TF relation along with NIR data from 2MASX were used by Hong et al. (2014) to calculate distances and peculiar velocities of 2018 inclined spirals. Hong et al. (2014) also provided bulk flow measurements which are consistent with the Λ cold dark matter (ΛCDM) model. Springob et al. (2016) used the calculated distances and peculiar velocities to describe the cosmography of the nearby universe. They found that the *IRAS* Point Source Catalog Redshift Survey (PSCz; Branchini et al. 1999) gave a better fit to their observations than the 2MASS Redshift Survey (2MRS; Erdoğdu et al. 2006b).

Another recent survey is the 6dF Galaxy Survey (6dFGS). Magoulas et al. (2012) determined the FP for $\sim 10^4$ galaxies in the 6dFGS. Campbell et al. (2014) provide a catalogue to be used to estimate distances and peculiar velocities for $\sim$ 9000 elliptical galaxies. Distances and peculiar velocities were derived by Springob et al. (2014). They also described the cosmography and compared their observations with the PSCz and 2MRS predictions. They found that their observations indicate more positive peculiar velocities toward the direction of the Shapley and Vela superclusters, whereas more negative velocities toward the direction of the Pisces-Cetus Supercluster than the predicted by the models. Scrimgeour et al. (2016) used the same data to measure the bulk flow of the nearby Universe which was also consistent with ΛCDM model.

The third survey is the *COSMICFLOWS*, which is a gathering of distances and peculiar velocities measured by different methods. Tully et al. (2008) presents distances for a sample of 1791 galaxies, which is now know as the

COSMICFLOWS-1. This sample is limited to $cz \leq 3000$ km s^{-1} and derived from four methods as follows:

1. Tully-Fisher relation distances (Tully & Pierce 2000, Karachentsev et al. 2002)
2. The Hubble Space Telescope Cepheid Key Project distances (Freedman et al. 2001)
3. Tip of the Red Giant Branch distances (Rizzi et al. 2007)
4. The Surface Brightness Fluctuation distances (Tonry et al. 2001, Mei et al. 2007)

Tully et al. (2013) presents the *COSMICFLOWS-2* which contains 8315 galaxies up to 30000 km s^{-1}. They used the same methods as in the *COSMICFLOWS-1* plus Fundamental Plane and Type Ia supernovae distances. More recently, Tully et al. (2016) published the *COSMICFLOWS-3* which contains 17669 galaxies mostly from either 3.6μm *Spitzer* TF relation or from the 6dFGS survey.

1.1.4 Problems

The bulk flow is the average peculiar velocity over a sphere of a given radius R. The expected value of this measurement can be made by integrating over the power spectral as in Strauss & Willick (1995):

$$< v^2 >_R = \frac{f^2}{2\pi^2} \int P(k)\, \widetilde{W}^2(kR)\, dk, \tag{1.2}$$

where $P(k)$ is the power spectral, $W(R)$ is the window function which depends on the survey geometry, and $\widetilde{W}(kR)$ is its Fourier Transform. Using a Gaussian window of radius 50 Mpc h^{-1}, and assuming a ΛCDM model, the expected value for each X, Y, and Z Cartesian coordinates is $v \sim 100 - 110$ km s^{-1}. Therefore, one should expect a bulk flow amplitude of $\sqrt{3} \times (100 - 110)$ km s^{-1}, which is $173 - 190$ km s^{-1}.

Kashlinsky et al. (2008) used the kinetic Sunyaev-Zeldovich effect (Sunyaev & Zeldovich 1972) and measured a very high bulk flow amplitude of $600 - 1000$

km s^{-1} on a scale ≥ 300 Mpc h^{-1}, which contradicts the expectation from the ΛCDM model. At the same time, Watkins, Feldman & Hudson (2009) used a new method, the minimal variance, to compile all major surveys (at the time) by weighting the peculiar velocities. They also found a large bulk flow amplitude of 407 ± 81 km s^{-1} but one that arises from within a much smaller scale of 50 Mpc h^{-1}. Surprisingly, both studies agree on the direction of the bulk flow, which suggest that either the ΛCDM model is wrong and we need to search for alternatives, or we live in a special place in the ΛCDM Universe.

In contrast, the same team used the same minimal variance method for Type Ia supernovae and found a bulk flow amplitude of 249 ± 76 km s^{-1}, which is consistent with the expectation from the ΛCDM model (Turnbull et al. 2012). Watkins & Feldman (2015) used the *COSMICFLOWS-2* catalogue and found consistency with the expectation from the ΛCDM model on scales of ≤ 40 Mpc h^{-1}. They also showed that the amplitude of the bulk flow increases with the scale radius.

More recently, Hong et al. (2014) used the 2MTF survey and measured an amplitude of the bulk flow of 292 ± 28 for a volume of 40 Mpc h^{-1}. Scrimgeour et al. (2016) used a much larger sample from the 6dFGS to measure a bulk flow of 248 ± 58 for a scale of 50 Mpc h^{-1}, which is in excellent agreement with the ΛCDM model predictions.

One disadvantage of all the previous measurements, one that may well constitute part of the explanation of these contradictions, is the exclusion of parts of the sky, in particular the Zone of Avoidance (ZOA) (Kraan-Korteweg 2005, Erdoğdu et al. 2006a, Loeb & Narayan 2008). The ZOA is known to obscure major parts of dynamically important structures such as the Perseus-Pisces Supercluster (PPS; Einasto et al. 1980, Giovanelli & Haynes 1982, Focardi et al. 1984, Hauschildt 1987), the Great Attractor (GA; Lynden-Bell et al. 1988, Woudt et al. 1999), the Local Void (LV; Tully & Fisher 1987, Kraan-Korteweg et al. 2008) and the recently discovered Vela Supercluster (VSCL; Kraan-Korteweg et al. 2017). In this thesis, we aim to complement the previously mentioned surveys such as 2MTF and *COSMICFLOWS-3* and provide distances and peculiar velocities for sources in the ZOA. This has never been attempted before. In the coming section we will give a brief overview of the ZOA and some of the redshift and peculiar velocity surveys that have been performed in the ZOA.

1.2 Zone of Avoidance

1.2.1 A historical introduction to the ZOA

Interstellar dust grains in the Milky Way absorb the light from the background galaxies (Trumpler 1930). This process is called dust extinction and constitutes a major problem when mapping the Large-Scale Structure (LSS) of galaxies using optical wavelengths because it leaves at least 20% of the sky unmapped. This process is wavelength-dependent and decreases towards longer wavelengths. Furthermore, objects lying behind the Milky Way appear redder than their intrinsic colour because the extinction is more prominent at shorter wavelengths. The infrared wavelength is able to penetrate through more dust extinction and is thus a better tracer of extragalactic emission. Cardelli, Clayton & Mathis (1989) quantify the extinction in the J, H, and K_s-bands to be 21%, 13%, and 9% of the extinction in the optical B-band, respectively. Therefore, the situation can be improved by using infrared wavelengths instead of optical wavelengths. But not completely, because of the stellar confusion at low Galactic latitudes, this affects about 10% of the sky particularly around the Galactic Bulge (GB) even at infrared wavelengths (Kraan-Korteweg & Lahav 2000). In contrast, H I 21-cm observations are neither affected by dust extinction nor stellar density (Kraan-Korteweg & Lahav 2000).

1.2.2 Redshift surveys in the ZOA

Given that H I 21-cm observations are not affected by dust, it has been widely used as a tool for systematic surveys to measure the redshift for gas-rich galaxies in the ZOA(Fisher & Tully 1981). The innovative design of the multibeam receivers on the Parkes, Arecibo, and Effelsberg radio telescopes allows for the first time systematic surveys of large areas of the sky because of the increase in the survey speed. After the installation of the multibeam receiver (MB: Staveley-Smith et al. 1996) on the 64-m Parkes radio telescope, three blind systematic deep H I surveys have been conducted to an rms of ~ 6 mJy. These three surveys together cover the most obscured parts of the ZOA visible from

Parkes, i.e. the main southern H I Parkes Deep Zone of Avoidance Survey (HIZOA; Staveley-Smith et al. 2016), the Northern Extension (NE; Donley et al. 2005) and the Galactic Bulge (GB; Kraan-Korteweg et al. 2008). These surveys show many new structures and also reveal the missing connections of conspicuous features that cross the ZOA, such as the GA, the Puppis region and the LV for the first time. Based on these surveys, H I spectra for over a thousand galaxies in the southern ZOA became available.

In the northern ZOA, the Arecibo L-band Feed Array Zone of Avoidance (ALFAZOA) Survey is conducted on the Arecibo Radio Telescope (McIntyre et al. 2015, Henning et al. 2017). ALFAZOA is a systematic blind survey conducted in two phases, shallow phase with rms $\sim 5-7$ mJy and deep phase with rms ~ 1 mJy. The shallow phase has been completed and the deep phase is ongoing. First results from the deep survey phase found 61 galaxies with the expected resolution of rms ~ 1 mJy. Another redshift survey in the northern ZOA is a blind H I 21-cm survey for the Perseus-Pisces filament using the Westerbork Synthesis Radio Telescope (Ramatsoku et al. 2016). This survey resulted in 211 detected galaxies.

Surveys for other selected regions of the northern ZoA have been conducted also with Arecibo (Henning et al. 2008; 2010). Moreover, some pointed H I observations for samples selected from optical and infrared surveys have been made in both southern and northern skies and contributed to our knowledge of the structures hidden behind the Milky Way (Kraan-Korteweg et al. 1996; 2002, Schröder et al. 2009, van Driel et al. 2009, Ramatsoku 2012).

1.2.3 Peculiar velocity field in the ZOA

Redshift surveys can tell us about the large-scale structure of the Universe by creating a 3-dimension map of the distribution of galaxies. The main limitation of redshift surveys is that they can not distinguish between the smooth Hubble velocity due to the expansion of the Universe and the peculiar velocity component induced by the gravitational attraction. This means we can neither trace the fluctuations in the matter distribution nor test the gravitational instability paradigm using redshift surveys only.

Previous distances and peculiar velocities measurements in the ZOA were dedicated to the Norma cluster region using FP relation for elliptical galaxies

(Woudt et al. 2005, Mutabazi et al. 2014). These studies were very successful in measuring the distance to the Norma cluster itself and suggest that Norma is the core of the Great Attractor region.

Given the success of these studies and the existence of the previously mentioned H I redshift surveys, we decided to use the existing systematic HIZOA survey as a basis for a TF application to determine the cosmic flow field in the ZOA. To achieve this, we have conducted deep NIR follow-up observations of the HIZOA galaxies in the J, H, and K_s-bands. We selected the NIR wavelength because it is less affected by dust than optical. For these observations we used the InfraRed Survey Facility (IRSF) on the 1.4m telescope at Sutherland, South Africa. With 10 minutes of exposure time on each galaxy in the HIZOA catalog and the high resolution ($0\farcs45$/pixel) of the IRSF telescope, we obtained high quality images in the ZOA (Williams et al. 2014, Said et al. 2016). Furthermore, narrow-band H I 21-cm of selected sample of galaxies were obtained for this project (Said et al. 2016). With these high fidelity NIR and H I data, peculiar velocity analyses have become feasible in the ZoA. In this thesis we will use the TF relation and these high quality data to determine distances and peculiar velocities for galaxies in the southern ZOA, hence fill in the gap that was excluded from the 2MRS and the 2MTF.

1.3 Structure of this thesis

This thesis is organized as follows: Chapter 2 presents the calibration of the NIR Tully-Fisher relation as derived from isophotal magnitudes of 888 spiral galaxies in J, H, and K_s bands. We also derived a correction model for the inclination. Chapter 3 presents H I 21-cm narrow-band observations for 394 galaxies in the southern ZOA. In Chapter 4, we present deep near-infrared images for 1108 detection in the three HIZOA catalogues. Chapter 5 presents the derivation of distances and peculiar velocities for 287 spiral galaxies in the southern ZOA. We also discuss the method we used to correct for the Malmquist bias. In Chapter 5 we also derived the velocity field from our observations and compared the resulting flows with those derived from the 2MRS and PSCz reconstruction models. We finish with the summary and an outline of future work in Chapter 6.

Chapter 2

On how to extend the NIR Tully-Fisher relation to be truly all-sky

Dust extinction and stellar confusion by the Milky Way reduce the efficiency of detecting galaxies at low Galactic latitudes, creating the so-called Zone of Avoidance. This stands as a stumbling block in charting the distribution of galaxies and cosmic flow fields, and therewith our understanding of the local dynamics in the Universe (CMB dipole, convergence radius of bulk flows). For instance, ZoA galaxies are generally excluded from the whole-sky Tully-Fisher Surveys ($|b| \leq 5^\circ$) even if catalogued. We show here that by fine-tuning the near-infrared TF relation, there is no reason not to extend peculiar velocity surveys deeper into the ZoA. Accurate axial ratios (b/a) are crucial to both the TF sample selection and the resulting TF distances. We simulate the effect of dust extinction on the geometrical properties of galaxies. As expected, galaxies appear rounder with increasing obscuration level, even affecting existing TF samples. We derive correction models and demonstrate that we can reliably reproduce the intrinsic axial ratio from the observed value up to extinction level of about $A_J \simeq 3$ mag ($A_V \sim 11$ mag), we also recover a fair fraction of galaxies that otherwise would fall out of an uncorrected inclination limited galaxy sample. We present a re-calibration of the 2MTF relation in the NIR J, H, and K_s-bands for isophotal rather than total magnitudes, using their same calibration sample. Both TF relations exhibit similar scatter at high

Galactic latitudes. However, the isophotal TF relation results in a significant improvement in the scatter for galaxies in the ZoA, and low surface brightness galaxies in general, because isophotal apertures are more robust in the face of significant stellar confusion.

2.1 Introduction

In order to have a reliable TF survey, the first step is to construct a global-unbiased TF template relation. As a secondary distance indicator, the TF template relation should be obtained from a sample of galaxies with known distances. This TF relation can then be used as the calibrated relation between the absolute magnitude and rotational velocity. Raw data and corrections used in the measurement of TF distances and peculiar velocities should be consistent with that used in the derivation of the TF relation.

In the last few decades, many TF template relations have been derived using either different samples or methodology. Shortly after the inception of the TF relation, Aaronson et al. (1979) calibrated the TF relation in the NIR H ($1.6\mu m$) for spiral galaxies in clusters. The NIR suffers less from dust extinction and is more sensitive to stellar mass. They found that in the infrared the scatter is lower than that in the B-band and the slope is much steeper. Based on Cepheid distances to 21 galaxies, Sakai et al. (2000) derived the TF relation in the B, V, R, I, and H-bands. These relations were used to derive a value of H_0. At the same time, Tully & Pierce (2000), Rothberg et al. (2000) performed a calibration of the B, R, I, and K relations. To avoid the Malmquist bias, they used the inverse method to fit the TF relation (Kraan-Korteweg, Cameron & Tammann 1988).

Bouché & Schneider (2000) used 2MASS J, H, and K_s-bands to derive TF relations in the ZoA. They used five different types of magnitudes from 2MASX (Jarrett et al. 2000). They conclude that the scatter was lowest for the isophotal K_s-fiducial 20 mag/arcsec^2 TF relation. Macri (2001) derived R, I, H, and K_s-band TF relations based on Cepheid distances. He used both total and isophotal magnitudes with the 20% HI-line-width (the width measured at 20% of the peak flux). His results indicate that isophotal H, K_s magnitudes and total I magnitudes relations yield comparable distances.

These relations have a scatter of $\sim 0\overset{\mathrm{m}}{.}2$. These two previous studies prove that isophotal magnitude works equally well in and out of the ZoA.

Masters et al. (2006) followed the same procedure described by Giovanelli et al. (1997) but with a larger sample to derive a new I-band TF relation. Their sample consists of 807 galaxies in the vicinity of 31 clusters and groups. This template relation has been used by Springob et al. (2007) to derive peculiar velocities of galaxies in the SFI++ catalog, which contains 4861 field and cluster spiral galaxies. Later, Masters et al. (2008) used similar procedures with a slightly larger sample to derive the absolute calibration of the J, H, and K_s-bands relations. These relations are the first step towards the 2MTF.

Recently, two independent groups have extended the TF to mid-infrared wavelengths. Sorce et al. (2013) use Spitzer ($3.6\mu m$) photometry for 213 cluster galaxies to derive the TF relation. Lagattuta et al. (2013) use the mid-infrared ($3.4\mu m$) $W1$-band of the Wide-field Infrared Survey Explorer ($WISE$) satellite with a larger sample of 568 field and cluster galaxies drawn from the 2MTF catalog to derive the TF relation. While Sorce et al. (2013) adopted the inverse fitting scheme, Lagattuta et al. (2013) used a bivariate scheme, where errors in both x and y are taken into consideration. More recently, Neill et al. (2014) use a quadratic form, by adding a curvature term, to fit $WISE$ W1 and W2 TF relations.

In this chapter we present a variation on the NIR TF relation that is specifically designed to be deployed in the ZoA and is applicable to the rest of the sky. We discuss all biases affecting TF surveys in the ZoA in Section 2.2. In Section 2.3 we present a re-calibration of the TF relations in the NIR J, H, and K_s bands using isophotal magnitudes. In the concluding Section 2.4 we summarize our results and discuss their implications for TF surveys.

2.2 Biases in the NIR TF due to extinction

2.2.1 Total magnitude

Undoubtedly, total magnitudes give the best estimate of a galaxy's total luminosity, and hence, total stellar mass of the galaxy. However, it is difficult to determine reliable total magnitudes for (a) low surface brightness galaxies for which these values can be severely underestimated (Jarrett et al. 2003), or (b) galaxies close to or in the ZoA. Due to the foreground dust extinction and high stellar density in the ZoA, the fainter outer parts of a galaxy are usually not recovered in the extrapolation of the surface brightness profiles to yield total magnitudes (Riad, Kraan-Korteweg & Woudt 2010). This is particularly severe in the relatively shallow 2MASS as discussed in details by Andreon (2002) and Kirby et al. (2008). Therefore, the advantage of using isophotal magnitudes over total is twofold.

To quantitatively determine the loss in total magnitudes for ZoA galaxies in 2MASX, we compare the magnitudes of the shallow 2MASX survey with a deeper and more spatially resolved ZoA survey. This is based on a deep NIR imaging conducted with the Japanese InfraRed Survey Facility (IRSF) mounted on a 1.4 m telescope situated at the South African Astronomical Observatory (SAAO) site in Sutherland, South Africa. Our comparison sample consists of 66 galaxies, observed in both 2MASX (Jarrett et al. 2000) and the IRSF Catalog (Williams et al. 2011; Williams et al. 2014; Said et al. in prep.). The latter is approximately 2 magnitudes deeper in the K_s-band, because of its longer exposure time (10 min) compared to 2MASX (8 seconds) and the higher resolution of $0\overset{\prime\prime}{.}45$/pix compared to the 2MASX resolution of $2''$/pix. We use the "total" extrapolated magnitudes measured by extrapolation of the double Sersic function and fiducial "isophotal" magnitudes measured in an elliptical aperture defined at the $K_s = 20$ mag arcsec^{-2} to construct a comparison between 2MASX and IRSF. The metric used to calculate the offset between 2MASX and ZoA-IRSF magnitudes is

$$\Delta m = m(\text{2MASS}) - m(\text{IRSF}). \tag{2.1}$$

Figure 2.1 shows the offsets between the 2MASS and IRSF for both total (left panel) and isophotal (right panel) magnitudes in the J, H, and K_s-bands (top to bottom). Each dot presents galaxy colour coded by dust extinction. It clearly shows that the mean offsets (red line) between 2MASX and IRSF for the "isophotal" magnitudes are insignificant while, the offsets are significant for the total magnitude, where the 2MASS estimates are systematically too faint compared to the deeper IRSF. High offsets will produce systematic errors in the

Table 2.1: Comparison between 2MASX and IRSF magnitudes using the total extrapolated magnitudes and fiducial isophotal magnitudes measured in an elliptical aperture defined at the $K_s = 20$ mag arcsec^{-2}

Band	Total		Isophotal	
	Δm	σ	Δm	σ
J	0.228	0.363	−0.020	0.155
H	0.252	0.293	−0.039	0.139
K_s	0.263	0.308	−0.033	0.159

measurement of peculiar velocities. The mean offsets for each band is printed in the bottom left corner of each plot. The mean offsets in total magnitudes for J, H, and K_s bands are 0.23, 0.25, and 0.26 mag respectively. These offsets are large enough to create an artificial flow of about 200 - 600 km s^{-1} in the velocity range of 2000 - 6000 km s^{-1} if the galaxies are located in a similar patch on the sky. The scatter in the offsets of the "isophotal" magnitudes is far smaller than that in the "total" magnitudes; it is reduced by more than a factor of two. Table 2.1 summarizes the mean offsets and the scatter values for each band.

This positive offset in total magnitude is due to the improved sensitivity and higher resolution ($0\farcs45$/pix) of the IRSF/SIRIUS data, which allows measurement of the surface brightness profile further along the disk compared to 2MASS thus capture more of the host galaxy light. Although minimal, there is a small offset between the 2MASX isophotal magnitudes compared to the IRSF. They are about 0.02 - 0.03 mag brighter rather than fainter. This can be explained by the lower resolution of 2MASS ($2''$/pix), which does not always resolve stars superimposed on the galaxy resulting in a systematic brightening of the source.

Because of these two effects, the loss of low surface brightness flux in 2MASX total magnitudes and extinction which exacerbates this effect, it seems prudent to use isophotal magnitudes, despite the fact that total magnitudes are better tracers than isophotal magnitudes. To test for any systematic bias, we compare the difference in total and isophotal flux. Figure 2.2 presents the aperture correction, $J_{20} - J_{ext}$, of the same 66 galaxies used in Fig. 2.1. Figure 2.2 shows that 2MASS isophotal magnitude J_{20} underestimates the total flux

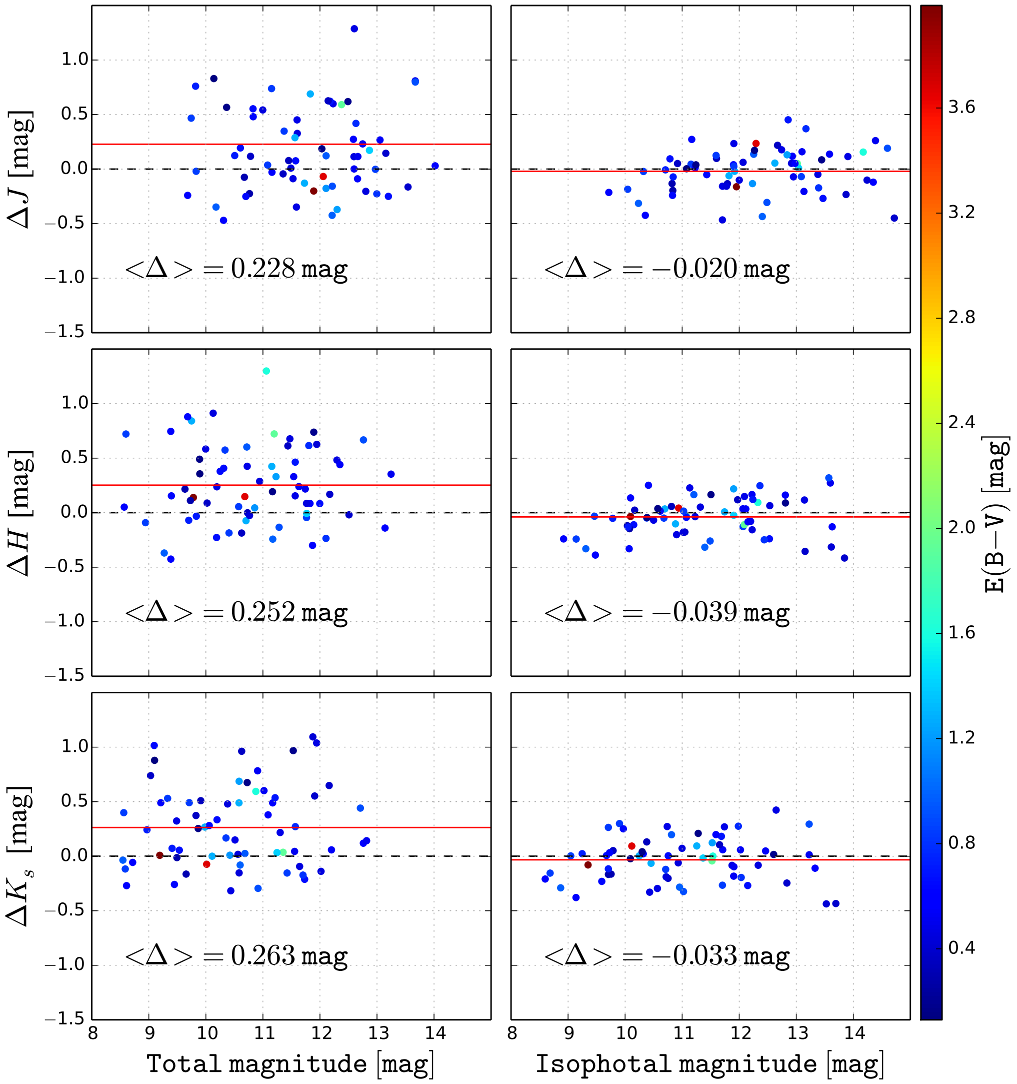

Figure 2.1: Comparison of 2MASX photometry with the ~2 mag deeper and more resolved IRSF photometry of ZoA galaxies. Each dot presents galaxy colour coded by dust extinction. The left panels display the total magnitudes and the right panels display the isophotal magnitudes with J, H, and K_s-band arranged from top to bottom. In all panels, solid red lines mark the mean offset, and the dashed black lines represent the zero-line. The mean offset is given in the bottom left corner of each plot.

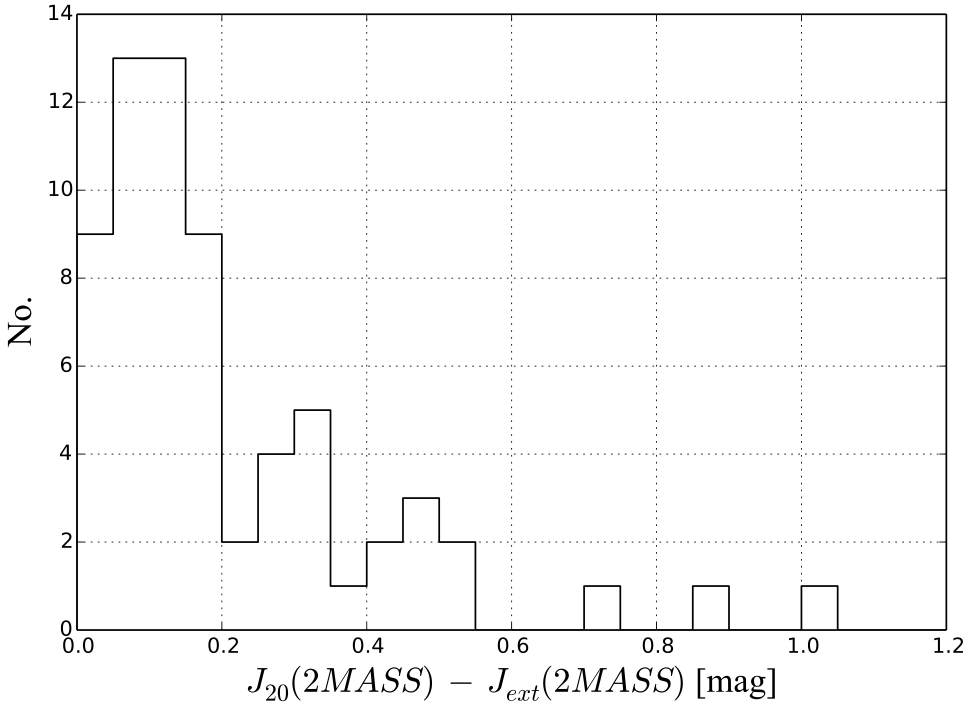

Figure 2.2: 2MASS aperture correction, $J_{20} - J_{ext}$, of 66 galaxies observed both in 2MASX and IRSF. The mean aperture correction is 0.21 mag.

by $< J_{20} - J_{ext} > = 0.21$ mag; in contrast, Fig. 2.1, left panel, shows that 2MASS total magnitude underestimates the total flux of 64% of the sample by $< J_{ext}(\mathrm{2MASS}) - J_{ext}(\mathrm{IRSF}) > = 0.47$ mag and overestimates 36% by 0.19 mag. Thus, any bias introduced by using isophotal magnitude is much smaller than the offsets introduced by using total magnitude in the ZoA.

To summarize, when working with 2MASS data for low surface brightness galaxies or galaxies affected by dust, "isophotal" magnitudes should preferentially be used over "total" magnitudes and most certainly for any TF derived distances. For this reason we derive in Section 3, a calibration of the NIR isophotal TF relation. The method and galaxy sample are exactly the same as these used by Masters et al. (2008) to derive their NIR TF for total magnitude.

2.2.2 Inclination

Spiral galaxies consist of a disk plus a bulge. The disk is almost flat and contains large amounts of dust and young stars, while the bulge is rounder and tends to be dust-poor with older generations. The effect of dust within the galaxy on the derived photometric parameters has been investigated by several authors (e.g., Han 1992, Giovanelli et al. 1994, Masters et al. 2003, Tuffs et al. 2004, Driver et al. 2007, Masters et al. 2010, Pastrav et al. 2013a;b). In this section we analyze another type of dust-induced change, namely, the change in the shape of the spiral galaxies due to the foreground dust in the Milky Way.

The effect of foreground dust extinction on the isophotal radius and magnitude of galaxies (elliptical as well as spirals) has been investigated for optical imaging by Cameron (1990) and more recently and extensively in the NIR J, H, and K_s bands by Riad et al. (2010). These studies were restricted to analyze the effect of dust on the magnitude and large diameter but not the minor axis, and therefore not the change in the apparent shape (axial ratio) of a galaxy which can vary considerably depending on bulge to disk ratio and intrinsic inclination.

Wherever dust obscuration occurs, such an effect should be accounted for. The first reason is the dependence of the TF parameters on inclination. The second reason is to avoid a systematic bias in the sample selections which generally are constrained by inclination uncorrected for absorption effects.

Inclination-dependent parameters in the TF relation

In the TF relation two parameters depend on the inclination of a spiral galaxy. The first one is the HI spectrum. To derive the maximum rotational velocity the observed line-width needs to be corrected to edge-on orientation. According to Springob et al. (2007) this is:

$$W = [\frac{w_{50} - \Delta_s}{1 + z} - \Delta_t]\frac{1}{\sin i} \tag{2.2}$$

where Δ_s and Δ_t are the instrumental and turbulence corrections, respectively. The inclination i is derived from the 2MASS J-band ellipticity $\epsilon_J = 1 - (b/a)_J$

via:

$$\cos^2 i = \frac{(1-\epsilon)^2 - q_0^2}{1 - q_0^2} \tag{2.3}$$

(e.g., Giovanelli et al. 1997) where q_0 is the intrinsic axial ratio of the galaxy ($q_0 = 0.13$ for Sbc and Sc, and $q_0 = 0.2$ for other types). The second set of dependency is with the NIR magnitudes, where we use the equation adopted by a number of authors (e.g., Giovanelli et al. 1994, Tully et al. 1998, Masters et al. 2003) to correct for the internal extinction. Inaccurate inclinations of spiral galaxies will create a systematic bias in both corrected line-width and absolute magnitude, and therefore in the derived peculiar velocities.

Systematic selection effect

To minimize the corrections in the line-width, most TF surveys apply a certain lower inclination limit on the axial ratio. The 2MTF project uses only galaxies with $b/a < 0.5$ (Masters et al. 2008, Hong et al. 2013, Masters et al. 2014), while in Said et al. (2014) we extend that limit to include galaxies with $b/a < 0.7$. Inaccurate inclinations will not only increase the uncertainty but can be systematic in that galaxies that appear rounder or more inclined will be excluded or included. This effect is dependent on the dust column density along the line-of-sight to the galaxies and as we show, is important for ZoA galaxies. It should therefore be explored how the foreground dust changes the apparent axial ratio. We quantify the effect of the foreground extinction on the number of galaxies in the TF sample through a statistical analysis based on simulated galaxies. The advantage of using artificial galaxies is twofold: firstly it measures the effect on the same galaxy with and without foreground dust; secondly we can test any correction model by applying it to the obscured galaxies and compare their axial ratio to their original intrinsic axial ratio.

The IRAF *artdata* tasks *gallist* and *mkobject* were used in this simulation. We created a sample of over 2000 artificial spiral galaxies with axial ratios $b/a \leq 0.5$ to be our primary TF sample. Four other samples have been generated with the same properties except for the magnitude zero point equivalent to adding a dust layer with increasing column density levels which we track accordingly.

Figure 2.3 shows the distribution of axes ratios of galaxies with different levels of dust extinction. Note the overall shift of the histograms to the right. The analysis confirms and quantifies our suspicion that galaxies appear rounder with increasing obscuration, which will affect the linewidth and internal extinction correction. Moreover, due to the axial ratio limit of the TF sample, the number of galaxies with $b/a \leq 0.5$ decreases significantly with increasing obscuration level. At dust extinction A_J of 1, 2, and 3 mag, the total number of galaxies in the TF sample decreases by 18%, 24%, and 31% respectively.

Figure 2.3 clearly demonstrates how significant this effect can decrease the number of galaxies used in the TF analysis, and therefore bias the survey sample. Future TF surveys based on HI surveys like WALLABY will exclude thousands of galaxies due to the axial ratio limit if this effect is ignored, and this will bias cosmic flow derivations as a function of foreground extinction.

To further study this effect, a sample of galaxies drawn from the 2MASS Large Galaxy Atlas (LGA) (Jarrett et al. 2003) is used to quantify this effect and test whether a correction model can be applied.

Quantitative analysis

In this section we use a sample of 54 spiral galaxies extracted from the 2MASS LGA. This sample of galaxies is selected to cover a wide range in galaxy size, brightness, morphological types and axial ratios. The sample contains both barred and unbarred galaxies. The galaxies have been artificially dimmed, similar to Cameron (1990) and Riad et al. (2010) but for the full 2-dimensional imaging data. We measured the surface brightness profile for both the major and minor axis by using the axial ratio as a free parameter.

We now demonstrate the method for the case of NGC1515 (Sbc). It has an intrinsic axial ratio of $b/a = 0.34$ in the J-band. In Fig. 2.4, the surface brightness is plotted against the major axis in the top panel and the minor axis in the bottom panel. The projection of the intercept between the solid line and the light profile on the x-axis gives the intrinsic major axis a° (top panel) and minor axis b° (bottom panel). We vary the simulation limits from

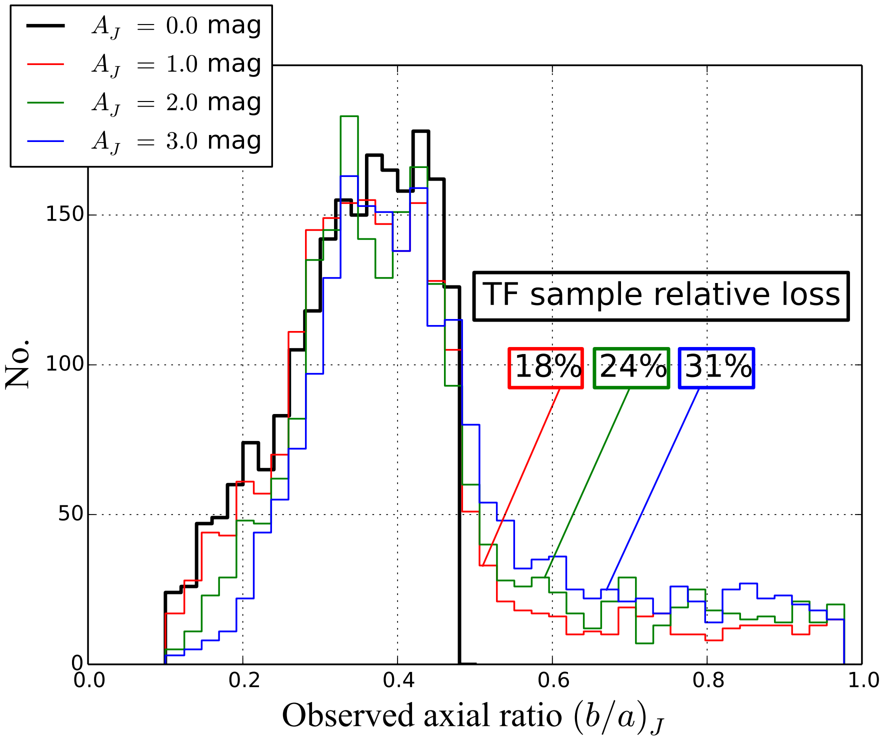

Figure 2.3: The axial ratio distribution of simulated galaxies at different levels of dust extinction. The histograms shift to the right, i.e. galaxies become less inclined, and the number of galaxies with $b/a \leq 0.5$ decreases with increasing obscuration level. At dust extinction A_J of 1, 2, and 3 mag, the TF sample relative loss is 18%, 24%, and 31% respectively.

$A_J = 0.0$ to $A_J = 3.0$ mag. The inward displacements represented by the dotted lines in Fig. 2.4 show the simulated extinction levels A_J in mag. For each level of extinction the major and minor axes have been measured from the intercept of the dotted line and the light profile. We then calculate the ratios of intrinsic versus absorbed axes ratio as a function of extinction.

$$f(a) = a^\circ/a, \tag{2.4a}$$

$$f(b) = b^\circ/b, \tag{2.4b}$$

where a°, a, b°, and b are the intrinsic and absorbed major and minor axes. The functions $f(a)$ and $f(b)$ are plotted for different values of simulated extinction A_J (top and middle panels) in Fig. 2.5. The bottom panel shows the ratio of $f(b)/f(a)$ against A_J, which clearly demonstrates that the axial ratio (b/a) increases with dust extinction (i.e. galaxies become increasingly rounder with increasing extinction). Using the formalism of Cameron (1990)

$$f(R) = 10^{c(A_\lambda)^d} \tag{2.5}$$

where c and d are derived from the data points in Fig. 2.5.

The galaxy NGC1515, with an intrinsic axial ratio of $b/a = 0.34$ in the J-band would appear to have $b/a = 0.48$ if seen through 1 mag of extinction, respectively $b/a = 0.62$ if seen through 2 mag of extinction. Deep in the ZoA where the extinction level would be very high, this edge-on galaxy would have been excluded from a typical TF survey analysis.

This procedure was followed for all 54 galaxies in our selected LGA sample and the change in parameters were used to construct an inclination correction model.

We will now investigate the correlations between the change in the axial ratio and the properties of the galaxies, such as, inclination or Hubble type and construct a correction model for inclination. The central surface brightness μ_c and the half-light effective mean surface brightness μ_e are used as indicator of morphological type (see Fig. 18 in Jarrett et al. 2003).

Following the recipe given by Riad et al. (2010) we include the central surface brightness μ_c in the J, H, and K_s-bands to optimize the correction

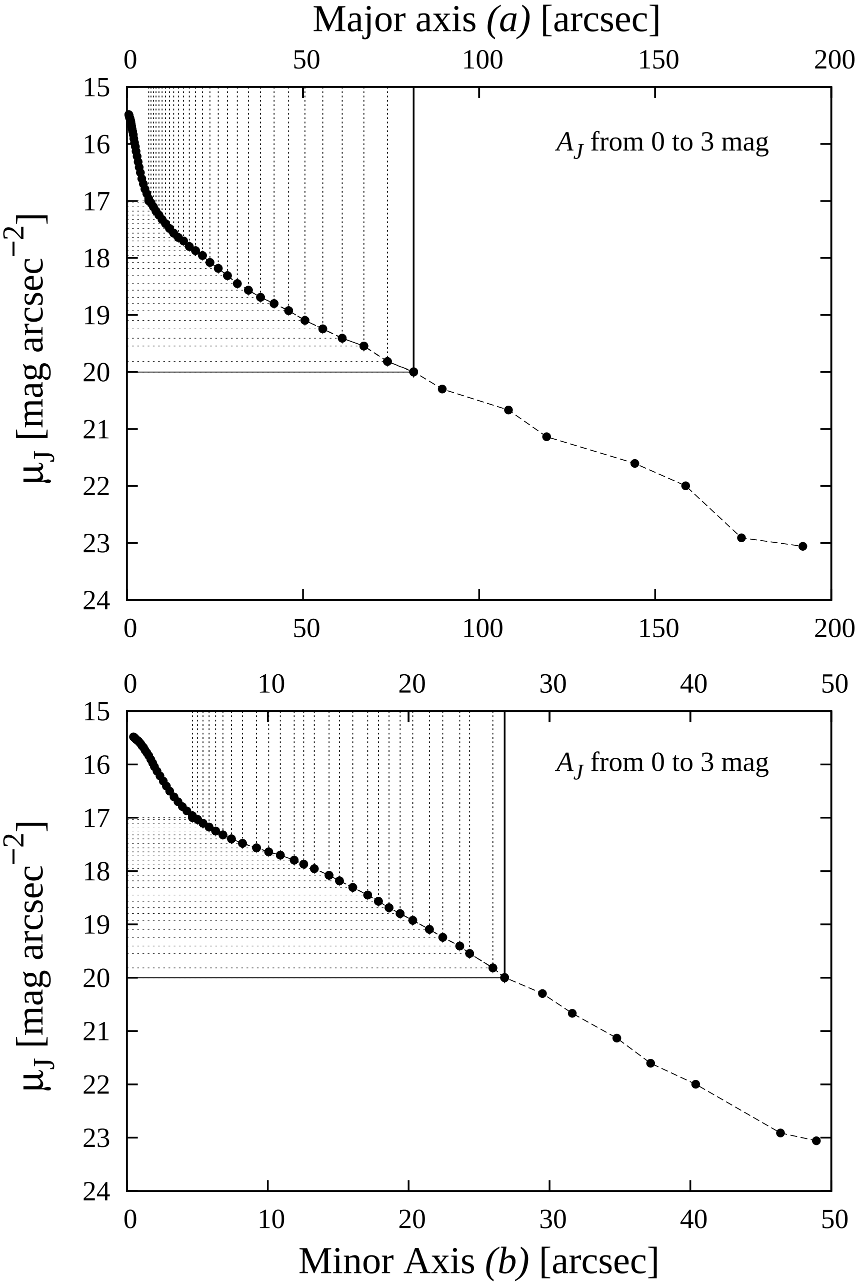

Figure 2.4: Surface brightness profile of NGC1515 (SAB(s)bc). The top panel shows the light profile against the major axis a. The bottom panel shows the light profile against the minor axis b. Note the different scales for major (top) and minor (bottom) axis. The dotted lines show different levels of dust extinction.

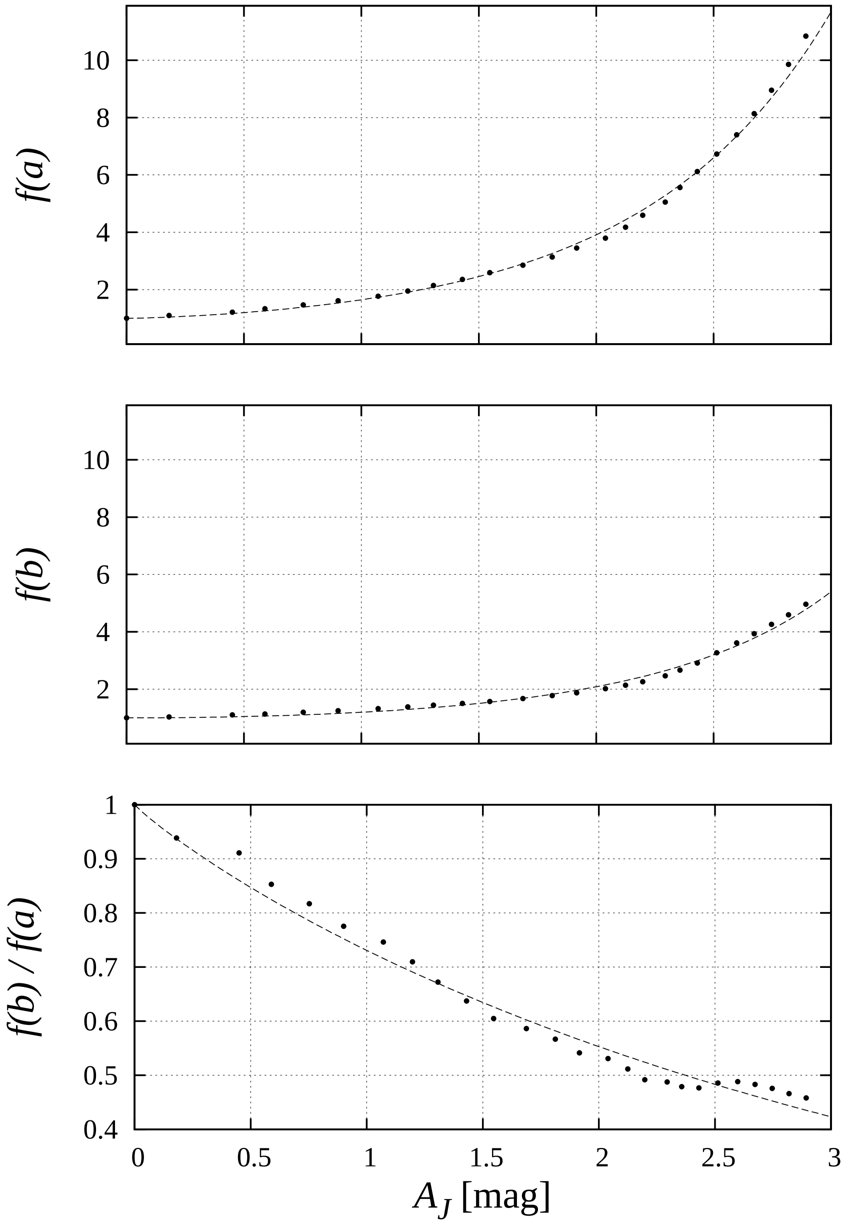

Figure 2.5: NGC1515 galaxy major axis correction due to the foreground extinction $f(a)$ in the top panel, the minor axis correction due to the foreground extinction $f(b)$ in the middle panel, and the axial ratio correction due to the foreground extinction $f(b)/f(a)$ in the bottom panel. The dashed lines in all panels show the fit to the data.

Table 2.2: The fitting parameters of the inclination correction based on the central surface brightness μ_c

	J		H		K_s	
Param.	$b/a \leq 0.4$	$b/a > 0.4$	$b/a \leq 0.4$	$b/a > 0.4$	$b/a \leq 0.4$	$b/a > 0.4$
c_0	−0.0165	−0.0049	−0.0221	−0.0109	−0.0328	−0.0254
c_1	0.1314	0.1624	0.1161	0.1239	0.1079	0.0762
d_0	3.4042	5.0117	13.0965	0.9383	1.1714	1.2599
d_1	−0.0510	−0.0742	−0.1387	0.0263	−0.0026	0.0125

Table 2.3: The fitting parameters of the inclination correction based on the effective surface brightness μ_e

	J		H		K_s	
Param.	$b/a \leq 0.4$	$b/a > 0.4$	$b/a \leq 0.4$	$b/a > 0.4$	$b/a \leq 0.4$	$b/a > 0.4$
c_0	−0.0044	−0.0004	−0.0061	−0.0056	−0.0100	−0.0537
c_1	0.1889	0.2756	0.1754	0.1433	0.1641	0.0220
d_0	9.4482	3.2485	101.65	0.1574	8.5084	1.9440
d_1	−0.1012	−0.0394	−0.2394	0.1241	−0.1186	−0.0144

model. The correction equations become

$$f(R, \mu_c) = 10^{c(\mu_c)(A_\lambda)^{d(\mu_c)}}, \tag{2.6}$$

where

$$c(\mu_c) = c_0 \exp(\mu_c \times c_1), \tag{2.7}$$

$$d(\mu_c) = d_0 \exp(\mu_c \times d_1). \tag{2.8}$$

The values of c_0, c_1, d_0, and d_1 in the J, H, and K_s-bands are the fitting parameters. The mean value for each parameter derived from all galaxies is given in Table 2.2.

The same method was applied using the half-light effective mean surface brightness μ_e. Table 2.3 give the mean value for each parameter.

Applying the correction model

To test whether our model reproduces the intrinsic axial ratio from the absorbed value, we compare the corrected values with the intrinsic values (see Fig. 2.6). We applied the correction based on μ_e (Eq. 2.6 and Table 2.3). Figure 2.6 presents the axial ratio distribution of simulated galaxies at different

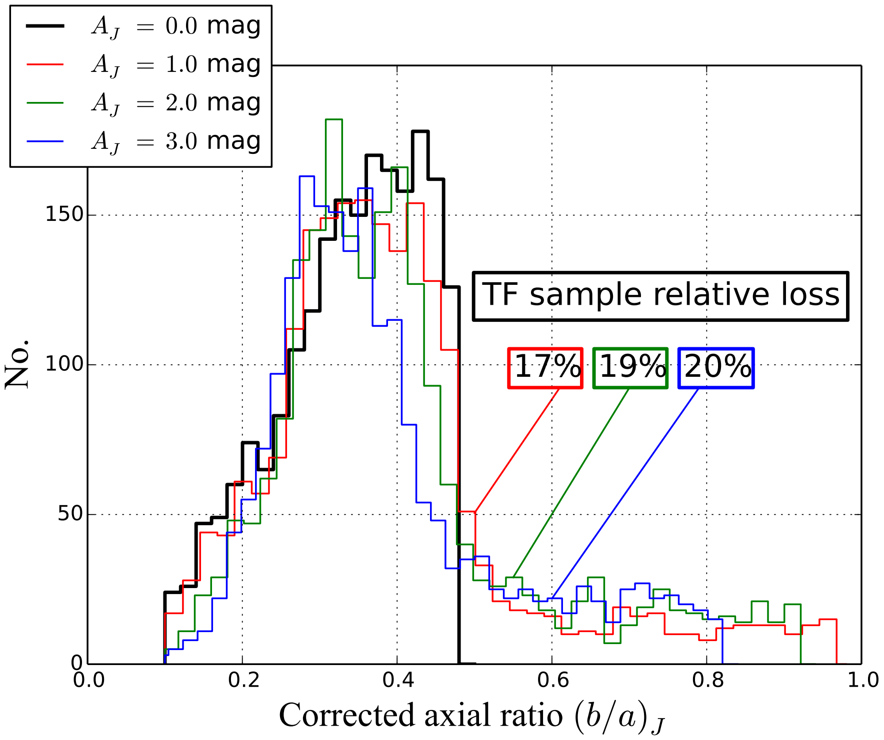

Figure 2.6: The axial ratio distribution of simulated galaxies at different levels of dust extinction after inclination correction. At dust extinction A_J of 1, 2,and 3 mag, the TF sample relative loss is 15%, 19%, and 20% respectively. It may be compared with the uncorrected results in Fig. 2.3

dust extinction level after applying the correction model. At dust extinction A_J of 1, 2, and 3 mag, the TF sample relative loss, after the correction, is 15%, 19%, and 20% respectively.

The effect of the correction model on the shape of the galaxy is hardly noteable in regions of low extinctions. At extinction level of $A_J \simeq 1$, we can recover only 4% of the TF sample relative loss (see, Figs. 2.3 & 2.6). In regions of higher extinction the improvement in parameters, particularly for the large galaxies seems to be significant. We can recover up to 18% and 59% at extinction level of $A_J \simeq 2$, and $A_J \simeq 3$ mag respectively. In conclusion, applying the correction model is not crucial at high latitudes, nevertheless, it is essential when working in the ZoA where the effect of dust extinction can be severe on the selection of the TF sample.

2.3 NIR isophotal TF relation

In this section we reiterate the advantages of NIR isophotal magnitude when applying the TF relations. The isophotal magnitude, specifically the 20 mag arcsec^{-2} fiducial measurement, is the primary brightness metric for 2MASX (Jarrett et al. 2003). It is uniformly measured across the sky for all galaxies. Total magnitudes are also measured, however they are known to be less reliable and prone to systematic underestimates, notably for low surface brightness galaxies and for confused environments (ZoA). Because of this, many authors prefer using 2MASX isophotal magnitudes instead of total magnitudes to avoid the large uncertainties in the required aperture correction (Bouché & Schneider 2000, Macri 2001, Karachentsev et al. 2002). For example, Macri (2001) used both total and isophotal magnitude to derive TF relations. The slope of his isophotal magnitude relations in H, and K_s is shallower than the total magnitude relation. He tested these isophotal relations against the I-band total magnitude and concludes that both isophotal H and K_s relations and I band total relation provide distance estimates with similar precision. Another TF study by Bouché & Schneider (2000) tests a variety of magnitudes provided by 2MASX and found that the scatter was lowest for the isophotal K_s magnitude. These studies agree with our findings in Section 2 that there are clear advantages of working with isophotal magnitudes over total magnitudes and that using isophotal TF relation in and out of the ZoA does not introduce any potential bias in the derived distance and peculiar velocity.

2.3.1 The TF sample

Two observational parameters describe the TF relation. The distance-independent rotation width is obtained from spectral data, and the imaging data provide all photometric quantities of interest. Different authors prefer different quantities, such as, the 20% line-width versus the 50% line-width, and isophotal versus total magnitudes. A variety of methods have been used over the years to derive w_{50} (Koribalski et al. 2004, Springob et al. 2005, Hong et al. 2013). These different algorithms can have a serious effect on the accuracy of the value of w_{50} if the S/N of the spectra are low. Consequently, TF samples only include galaxies with high S/N spectra, so that the noise will not affect the width measurement and the difference between different algorithms becomes negligible.

The calibration sample of galaxies is the same as that used in Masters et al. (2008)[*]. Their rotation-widths were obtained from either the Cornell HI digital archive (Springob et al. 2005) or optical rotation curves (Catinella et al. 2005). The photometric quantities of the calibration sample are a mix of J, H, and K_s-bands quantities from 2MASX and I-band quantities from Masters et al. (2006). We cross-matched the Masters et al. (2008) calibration sample with the 2MASX catalog and extracted the “isophotal” magnitudes for all of them.

Rotation widths

The rotation widths are drawn completely from the Masters et al. (2008) calibration sample which is available online[†], see Springob et al. 2005 for details.

Photometry

All photometric quantities are derived from the 2MASX catalog. Their properties are described online in Cutri et al. (2006)[‡]. The photometric quantities of the TF calibration are:

1. Isophotal magnitude: We use the J, H, and K_s-bands fiducial isophotal magnitudes measured at 20.0 mag arcsec^{-2} in K_s band, which is roughly equal to the 1 σ background noise level (Jarrett et al. 2003).
2. J-band axial ratio: The J-band axial ratio $(a/b)_J$ fit to the 3 σ isophote is used (the isophote corresponds to a surface brightness $\sim$ 3 times the background noise).
3. Central surface brightness μ_c: The central surface brightness μ_c in the J, H, and K_s-bands obtained from the 2MASS XSC. This parameter is necessary for the derivation of the Galactic extinction corrections.

---

[*] We thank Karen Masters for making that available to use

[†] http://www.icg.port.ac.uk/∼mastersk/TFdata.html

[‡] http://www.ipac.caltech.edu/2mass/releases/allsky/doc/

4. The colour reddening $E(B-V)$: Galactic extinction A_J, A_H, and A_{K_s} are approximated by the colour reddening $E(B-V)$ from the DIRBE dust map (Schlegel et al. 1998). Dust extinction of the calibration sample are very low and the difference between Schlegel et al. (1998) values and its updated values from Schlafly & Finkbeiner (2011) have no effect on our calibration. However for high extinction regions we use the Schlafly & Finkbeiner (2011) values of 0.87 times Schlegel et al. (1998) values which is in excellent agreement with the independent derived correction in the ZoA by Schröder et al. (2007) and more recently by Williams et al. (2014).

2.3.2 Photometric corrections

To construct a global TF relation, the photometric quantities from the 2MASX must be corrected for the cosmological redshift, internal extinction, and Galactic extinction. The corrected absolute magnitude, derived from the observed apparent magnitude is calculated as follows[§]:

$$M_{corr} - 5\log h = m_{obs} - A_X - I_X - k_X - 5\log v_{CMB} - 15, \qquad (2.9)$$

where A_X, I_X, and k_X are a correction for foreground extinction due to the dust in the Milky Way, a correction for extinction internal to the galaxy itself, and a cosmological k-correction respectively. Because these three corrections are wavelength-dependent, the index X refers to the wavelength band. For the k-correction we used the same procedure used by Masters et al. (2008). In the next two subsections we describe the methods used to correct for internal and Galactic extinction as we deviate slightly from the Masters et al. (2008) procedure.

Internal extinction

Dust extinction internal to galaxies themselves is a challenging quantity to estimate. Since the early work of Holmberg (1958) it has been widely assumed that spiral galaxies are mostly transparent. Later studies suggest that spiral

---

[§] The sign error in the application of the internal extinction and k-corrections to magnitudes used in Masters et al. (2008) and corrected in Masters et al. (2014) has been accounted for.

galaxies are optically thick (Valentijn 1990). Again, this study received some criticism (e.g. Burstein et al. 1991). The best study to date (Holwerda et al. 2009), uses occulting galaxy pairs to show that dust distributions vary, creating both optically thin and thick regions.

This problem has been investigated by several authors from different aspects. Most correction models for the internal extinction have been constructed as a function of inclination. In the TF relation, inclined galaxies are preferentially used, but the magnitudes of inclined galaxies are more affected by dust. In our analysis we adopt the empirical relation of internal extinction described in Giovanelli et al. (1994), Tully et al. (1998), Masters et al. (2003), which is dependent on axial ratio and waveband, as follows:

$$I_\lambda = \gamma \, \log(a/b). \tag{2.10}$$

The J-band axial ratio $(b/a)_J$ is the best tracer of the inclination, as it suffers less than the H, and K_s -bands from the effect of the bulge population. The axial ratio needs to be corrected for seeing, which is parameterized as

$$(a/b)_{corr} = (a/b)_{obs}(1 - 0.02x + 0.21x^2 - 0.01x^3), \tag{2.11}$$

where $x = \mathrm{FWHM}(\frac{a/b}{r_{20}})$, and FWHM $= 2\overset{''}{.}5$ (the full-width half-maximum of the seeing disc). Masters et al. (2003) provide different values of γ in J, H, and K_s-bands from different statistical tests based on total magnitudes. We deviate slightly in our approach because applying correction for total magnitudes will results in an over-correction in isophotal magnitudes. To investigate the internal extinction in J, and H bands, we use the calibration sample, 888 galaxies, to test the colour gradients (measured at 20.0 mag arcsec^{-2} in K_s band) with inclination. We assume that the internal extinction in the K_s-band isophotal magnitude is negligible (i.e., $\gamma_{K_s} = 0$); the effect of internal extinction is indeed very small in K_s band even in total magnitudes (Tully et al. 1998, Masters et al. 2003). Figure 2.7 shows how NIR colours, $J_{20} - K_{s20}$ and $H_{20} - K_{s20}$, change with inclination.

In this Fig. we used the calibration sample, 888 galaxies, binned in inclination groups. The slopes of Eq. 2.10 are:

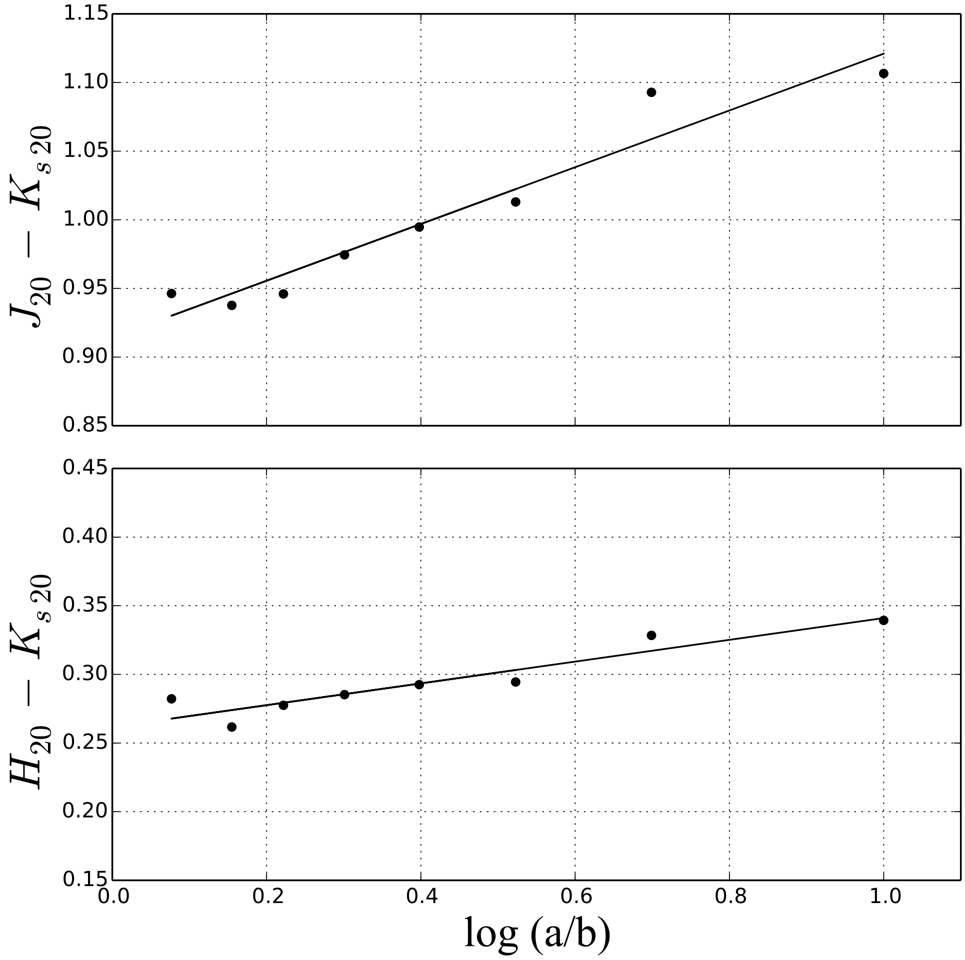

Figure 2.7: NIR colour, $J_{20} - K_{s20}$ and $H_{20} - K_{s20}$, dependence on inclination of the calibration sample (888 galaxies) binned in inclination groups. The slopes of Eq. 2.10 are 0.21 for $J_{20} - K_{s20}$ and 0.08 for $H_{20} - K_{s20}$. We assume that the K_s-band isophotal magnitude is internal extinction free (i.e., $\gamma_{K_s} = 0$)

$$\begin{aligned}
\gamma_{J_{20}-K_{s20}} &= \gamma_{J_{20}} - \gamma_{K_{s20}} \\
&= \gamma_{J_{20}} \\
&= 0.21 \pm 0.03, \qquad (2.12a) \\
\gamma_{H_{20}-K_{s20}} &= \gamma_{H_{20}} - \gamma_{K_{s20}} \\
&= \gamma_{H_{20}} \\
&= 0.08 \pm 0.02. \qquad (2.12b)
\end{aligned}$$

These values of γ mean that the effect of internal extinction is very small in the isophotal magnitudes compared to total magnitudes because most of the dust are in the disk.

Galactic foreground extinction

Galaxies appear smaller and fainter due to the dust extinction in the Milky Way. Therefore a correction to the isophotal magnitude is needed to account for the loss of light due to this dimming. Riad, Kraan-Korteweg & Woudt (2010) present two methods to apply the isophotal correction: (*i*) the average correction method which is a very direct application, and (*ii*) the more optimized correction method which is more accurate than the average correction but requires a fit to the light profile of the galaxy to determine either the disc central surface brightness, μ_0, or the combined disc plus bulge central surface brightness, μ_c. The optimized correction was used here, because the central surface brightness is available in the 2MASX. The central surface brightness is defined as the magnitude of the mean flux within a radius ≤ 5 arcsec.

2.3.3 Bias corrections

Many TF samples, including the one we use here, contain a broad range of spiral types. A single relation may not be appropriate for all spiral types as expressed already by Tully & Fisher themselves. Masters et al. (2008) found type dependences with their sample, and our analysis of this effect based on the “isophotal” magnitude yields similar trends. The earlier types have a shallower slope than later types. We correct to an Sc type (less bulge, more disk component) relation. In the J-band we use

$$\Delta M_{Sa} = 0.27 - 2.46(\log W - 2.5), \tag{2.13a}$$

$$\Delta M_{Sb} = 0.15 - 1.14(\log W - 2.5). \tag{2.13b}$$

In the H-band we use

$$\Delta M_{Sa} = 0.22 - 2.81(\log W - 2.5), \tag{2.14a}$$

$$\Delta M_{Sb} = 0.15 - 1.16(\log W - 2.5). \tag{2.14b}$$

In the K_s-band we use

$$\Delta M_{Sa} = 0.11 - 3.51(\log W - 2.5), \tag{2.15a}$$

$$\Delta M_{Sb} = 0.13 - 1.44(\log W - 2.5). \tag{2.15b}$$

These values are derived using the isophotal photometry for each sample before any bias corrections.

Due to the broad range in surface brightness and colour of the galaxy sample, further bias corrections including Incompleteness bias, Cluster size bias and Cluster peculiar velocity have to be applied. We used the values derived by Masters et al. (2008) to correct for these biases. Any difference in the correction would be incredibly small and much lower than any of the other corrections.

2.3.4 Calibration and scatter

Different fitting procedures have been used to derive the final parameters of the TF relation. The inverse TF was suggested by Kraan-Korteweg et al. (1986) to overcome the Malmquist bias. Giovanelli et al. (1997) used the minimization of χ^2 method to determine the direct, inverse, and bivariate forms of the linear TF relation. In Pizagno et al. (2007), the maximum likelihood method was used to estimate the slope a, intercept b, and intrinsic scatter ϵ_{int} of the TF relation. Here we are interested in the bivariate fit case, where errors in both

Table 2.4: Parameters of bivariate fit after all corrections derived from both isophotal (this work) and total magnitude (Masters et al. 2014).

Band	This work				Masters et al. (2014)			
	a_{iso}	b_{iso}	ϵ_a	ϵ_b	a_{tot}	b_{tot}	ϵ_a	ϵ_b
J-band	−20.951	−9.261	0.018	0.114	−21.370	−10.61	0.018	0.12
H-band	−21.682	−9.288	0.018	0.115	−21.951	−10.65	0.017	0.11
K_s-band	−21.861	−10.369	0.018	0.120	−22.188	−10.74	0.015	0.10

x and y are taken into consideration. We therefore use the linear form:

$$y(x) = a_{bi} + b_{bi}x, \tag{2.16}$$

via minimization of χ^2

$$\chi^2 = \sum_{i=1}^{N}[\frac{y_i - y(x_i; a_{bi}, b_{bi})}{\epsilon_i}]^2. \tag{2.17}$$

The error used in the computation is defined as $\epsilon_i = [(\epsilon_{x,i}b_{bi})^2 + \epsilon_{y,i}^2 + \epsilon_{int}^2 + \mathrm{cov}_{xy}]^{1/2}$, where cov_{xy} represents the covariance between the errors in x and y which is not significant in our case.

After applying all of the above detailed bias corrections, and applying the bivariate fitting mechanism to the Masters et al. (2008) 888 calibrator galaxies, our final isophotal TF relations have the form:

$$\begin{aligned} M_J - 5\log h &= -20.951 - 9.261(\log W - 2.5), & (2.18a)\\ M_H - 5\log h &= -21.682 - 9.288(\log W - 2.5), & (2.18b)\\ M_{K_s} - 5\log h &= -21.861 - 10.369(\log W - 2.5). & (2.18c) \end{aligned}$$

Table 2.4 presents the fitted parameters derived from both isophotal magnitude (this work) and total magnitude from Masters et al. (2014). Figure 2.8 shows the final isophotal TF relations for the J, H, and K_s-band from top to bottom.

The slope for the isophotal TF relations in J and H bands are shallower than the total TF but similar in the K_s band. This can be explained by Fig. 2.9, which shows the difference between isophotal and total TF relation as a function of line-width and inclination.

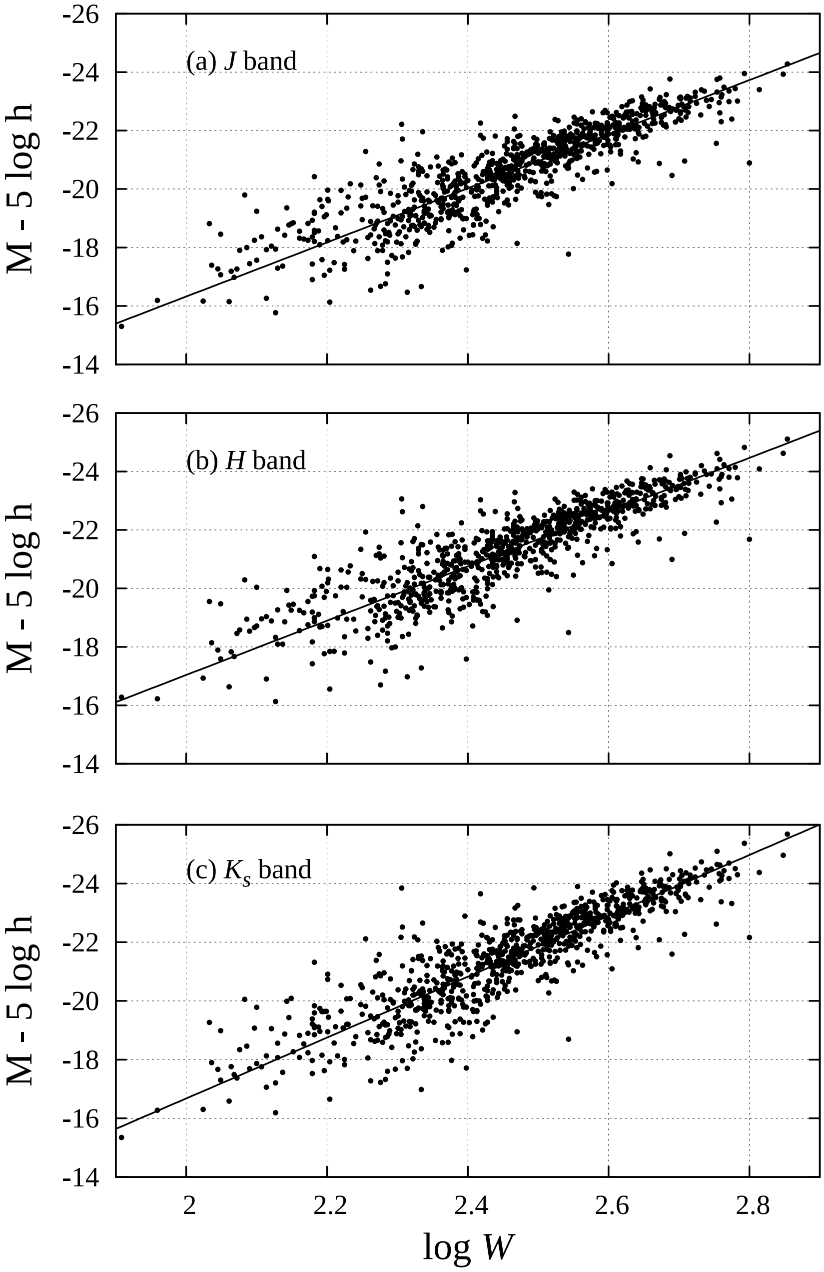

Figure 2.8: Isophotal TF relation for the (a) J-band, (b) H-band, and (c) K_s-band. The solid line shows the respective bivariate fit to the data.

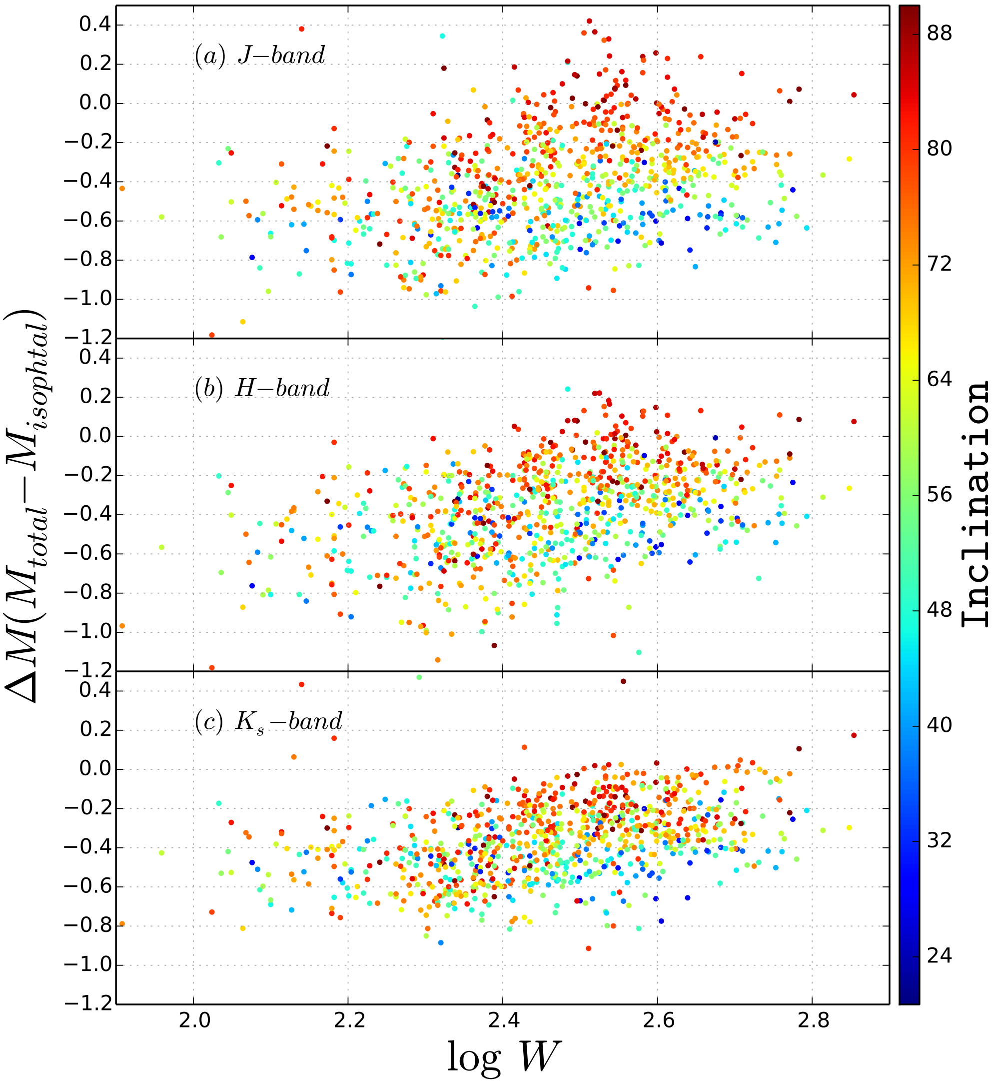

Figure 2.9: Total versus isophotal magnitude for the template galaxies as a function of line-width. Galaxies are colour coded by its inclination.

Each dot in Fig. 2.9 presents a galaxy from the TF calibration sample colour-coded by its inclination. The K_s band has the tightest scatter in Fig. 2.9. This is not a surprising result given that the aperture correction in the K_s band is lowest compared to the J and H bands (see also Fig. 7 in Jarrett et al. 2003). The deviation increases toward small and less inclined galaxies whose surface brightness profiles are not well determined. This further supports the preference of using isophotal magnitudes as the total magnitude for those galaxies become unreliable.

Figure 2.8 also reveals an increasing scatter in the TF relation with decreasing rotation width. Using the relation used in Giovanelli et al. (1997) to parameterize the scatter

$$\sigma = a + b(\log W - 2.5), \tag{2.19}$$

the total scatter is calculated, and displayed in Fig. 2.10 for the J, H, and K_s-bands as a function of the line-width.

The error on the isophotal magnitude (least source of error), as well as the error on the rotation width multiplied by the slope of the TF relation (expressed in magnitudes) are also displayed in Fig. 2.10. A linear fit to the intrinsic scatter gives

$$\begin{aligned}
\epsilon_{int,J} &= 0.46 - 0.90(\log W - 2.5), && (2.20a)\\
\epsilon_{int,H} &= 0.47 - 0.94(\log W - 2.5), && (2.20b)\\
\epsilon_{int,K_s} &= 0.46 - 0.83(\log W - 2.5). && (2.20c)
\end{aligned}$$

The intrinsic scatter, in magnitude units, is a crucial parameter to understand the errors on both distances and peculiar velocities derived from the TF relation. The intrinsic scatter in both the “isophotal” and “total” methods are nearly identical, because the calibration sample of galaxies is hardly affected by foreground dust of the Milky Way.

Comparing equations 2.20 with Masters et al. (2008) results shows that the intrinsic scatter is smaller in the total magnitude relation for the larger galaxies ($\log W > 2.5$), while for smaller galaxies ($\log W < 2.5$) the “isophotal” magnitude relation shows less scatter.

2.4 Summary

We study the effect of foreground dust and source confusion on galaxy photometry in the context of employing the TF method in the Zone of Avoidance. Two different methods using independent samples of galaxies were used to quantify this effect. Both methods confirm and quantify that galaxies appear rounder with increasing obscuration level leading to a substantial loss of galaxies in inclination-constrained TF samples deep in the ZoA. Correction models are proposed based on 54 spiral galaxies from the 2MASS LGA with different morphological types and intrinsic axial ratios. These correction models have been tested and show its applicability to reproduce the intrinsic axial ratio from the observed value for large galaxies up to extinction level of about $A_J \simeq 3$ mag, and recover a fair fraction of galaxies that otherwise would fall out of an uncorrected inclination limited galaxy sample.

We present the recalibration of the Tully-Fisher relation for isophotal magnitudes in the NIR J, H, and K_s-bands. This calibration sample of 888 galaxies is the same as the one used for the 2MTF project for total magnitudes. No significant change in the isophotal TF relation scatter was found in comparison to the scatter in the total TF relation because the calibration sample is minimally affected by the dust of the Milky Way. However, this does not hold for low surface brightness galaxies or galaxies obscured by dust where isophotal magnitudes are more robust.

The isophotal NIR TF relation has been applied in a pilot project by Said et al. (2014) to a preliminary sample of HI detected galaxies in the ZoA which had deep NIR photometry (Williams et al. 2014) and found to be quite promising. Considerable improvement of the scatter and the systematic offset of the derived peculiar velocities in the ZoA is achieved when the isophotal TF relation is applied in comparison to the traditional total magnitude method. The offsets of about 0.2 - 0.3 mag which may create an artificial flow of about 200 - 600 km s^{-1} in the velocity range of 2000 - 6000 km s^{-1}, have been reduced to about 0.02 - 0.03 mag in J, H, and K_s bands. Combining our data with that from 2MTF will provide more complete all-sky peculiar velocity survey. Using

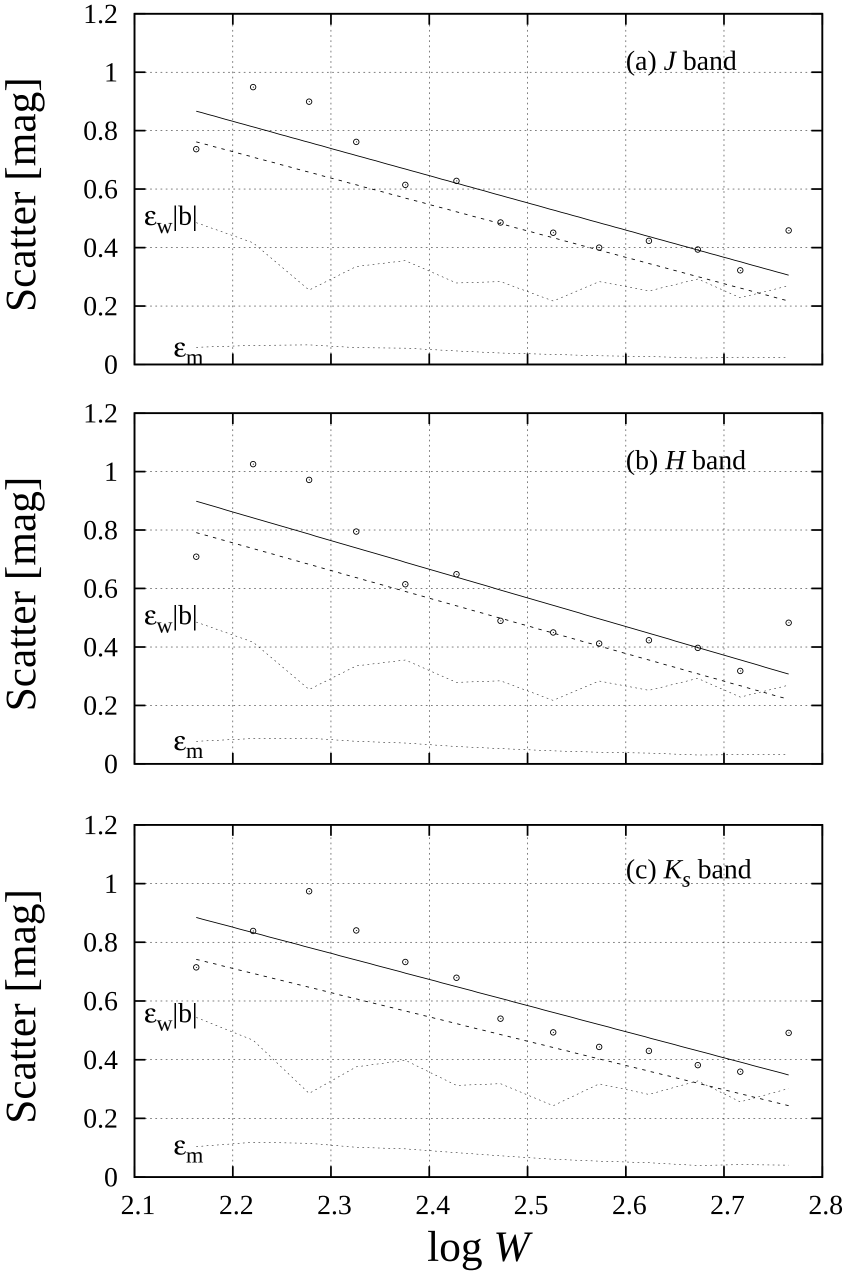

Figure 2.10: Scatter in the (a)J-band, (b)H-band, and (c)K_s-band. The circles present the total scatter averaged within bins in velocity width. The linear fit to the total scatter is shown as a solid line and the dashed line shows the linear fit to the intrinsic scatter. The dotted lines present the error on the isophotal magnitude and the error on the rotation width multiplied by the slope

the isophotal TF relation and accounting for the effect of extinction on inclination will lead to an improved TF analyses at lower latitudes. It will allow the extension of cosmic flow derivations deeper into the ZoA compared to current surveys and, moreover, improve on the results for galaxies with $|b| \leq 5^\circ$ that are already affected by dust, or any other regions of high extinction in the sky.

Chapter 3

21 cm H I-line spectra of southern ZOA galaxies

High-accuracy H I profiles and linewidths are presented for inclined ($(b/a)^o < 0.5$) spiral galaxies in the southern Zone of Avoidance (ZOA). These galaxies define a sample for use in the determinations of peculiar velocities using the near-infrared Tully-Fisher (TF) relation. The sample is based on the 394 H I-selected galaxies from the Parkes H I Zone of Avoidance survey (HIZOA). Follow-up narrow-band Parkes H I observations were obtained in 2010 and 2015 for 290 galaxies, while for the further 104 galaxies, sufficiently high signal-to-noise spectra were available from the original HIZOA data. All 394 spectra are reduced and parameterized in the same systematic way. Five different types of linewidth measurements were derived, and a Bayesian mixture model was used to derive conversion equations between these five widths. Of the selected and measure galaxies, 342 have adequate signal-to-noise (S/N $\geq$ 5) for use in TF distance estimation. The average value of the signal-to-noise ratio of the sample is 14.7. We present the H I parameters for these galaxies. The sample will allow a more accurate determination of the flow field in the southern ZOA which bisects dynamically important large-scale structures such as Puppis, the Great Attractor, and the Local Void.

3.1 Introduction

This chapter is the first in a series of papers presenting data obtained in a systematic way for future applications of the TF relation in the ZOA. It focuses on the first approach, where we start out with an H I-selected sample. It is based on the systematic HIZOA surveys pursued with the Parkes telescope, specifically designed to unveil the large-scale structures of galaxies in the nearby Universe across the most obscured part of the mostly southern ZOA (Staveley-Smith et al. 2016), i.e. in areas were most other surveys fail. The integration time of the HIZOA surveys are a factor of five longer compared to the H I Parkes All-Sky Survey (HIPASS) (Meyer et al. 2004). These H I-selected galaxies are not biased with respect to the Galactic foreground dust layer, as shown in Staveley-Smith et al. (2016).

Three blind systematic deep H I ZOA surveys were conducted with the Multibeam Receiver on the 64-m Parkes Radio Telescope, i.e. the main southern H I Parkes Deep Zone of Avoidance Survey (HIZOA-S; Staveley-Smith et al., 2016), the Northern Extension (HIZOA-N) (Donley et al. 2005) and the Galactic Bulge (GB) (Kraan-Korteweg et al. 2008). These three surveys show many new structures and also reveal the missing connections in the conspicuous features that cross the ZOA, such as the GA, the Puppis region and the LV for the first time. This highlights the importance of the ZOA in the understanding of the cosmic web. Based on these surveys, H I spectra for over a thousand galaxies in the southern ZOA are now available.

Accordingly, follow-up pointing deep NIR observations for all galaxies in the three HIZOA surveys were conducted between 2006 and 2013 with the Japanese InfraRed Survey Facility (IRSF), a 1.4 m telescope situated at the South African Astronomical Observatory site in Sutherland. Data from 2006 to 2010 were published in Williams et al. (2014). In the next chapter, we will present high-quality NIR J, H, and K_s-band observations for the completed HIZOA surveys, and discuss completeness and reliability of the NIR catalog for application in a TF-survey. The NIR data has already been used extensively for the sample selection for the present TF analysis with regard to unambiguous counterpart identification, availability of high accuracy photometry, and the required inclination limits.

The determination of the H I parameters also required further attention. We need highly resolved H I-line profiles, with high signal-to-noise and homogeneous analysis. 104 spectra in the ZOA TF sample already meet our requirements (S/N $>$ 5, very well resolved H I profile). Based on the newly-derived NIR imaging, an additional 290 needed to be re-observed to obtain higher resolution HI profiles. This was achieved by conducting 21-cm narrow-band follow-up observations with the Multibeam Receiver on the 64-m Parkes Radio Telescope.

In this chapter we present the newly obtained 21 cm H I line spectra. We discuss the observations and data reduction procedures in Section 3.2. In Section 3.3 we describe the algorithm with which we derive the H I parameters and associated errors, both for the new observations and the re-measurements of the HIZOA linewidths, the final compilation, the characteristics of the data set and comparison with the published H I data. We summarize our results in Section 3.4.

3.2 Observations and Data Reduction

3.2.1 Sample Selection

HIZOA is a blind H I survey of the southern ZOA ($|b| < 5°$; Dec $< +15°$), conducted with the 64-m Parkes Radio Telescope* in three parts: (1) the main part (HIZOA-S) covers $|b| < 5°; 212° \leq l \leq 36°$ (Staveley-Smith et al., 2015), (2) the Northern Extension (HIZOA-N) covers the northern regions visible from Parkes ($|b| < 5°; 36° < l < 52°$ and $196° < l < 212°$; Donley et al. 2005), and (3) the Galactic Bulge (GB) extension, which goes to higher latitudes around the GB region ($5° < |b| < 10°; 332° < l < 36°$ and $10° < b < 15°; 348° < l < 20°$; Kraan-Korteweg et al. 2008). These surveys cover the most obscured southern ZOA visible from Parkes out to 12000 km/s, and result in more than a thousand detected galaxies with an rms $\sim$ 6 mJy/beam.

Our H I sample selection is based on a cross-identification of the HIZOA galaxies with the high-quality NIR IRSF images. We select only galaxies with secure counterparts and good photometry (error in isophotal magnitude less

---

*The Parkes telescope is part of the Australia Telescope National Facility which is funded by the Commonwealth of Australia for operation as a National Facility managed by CSIRO.

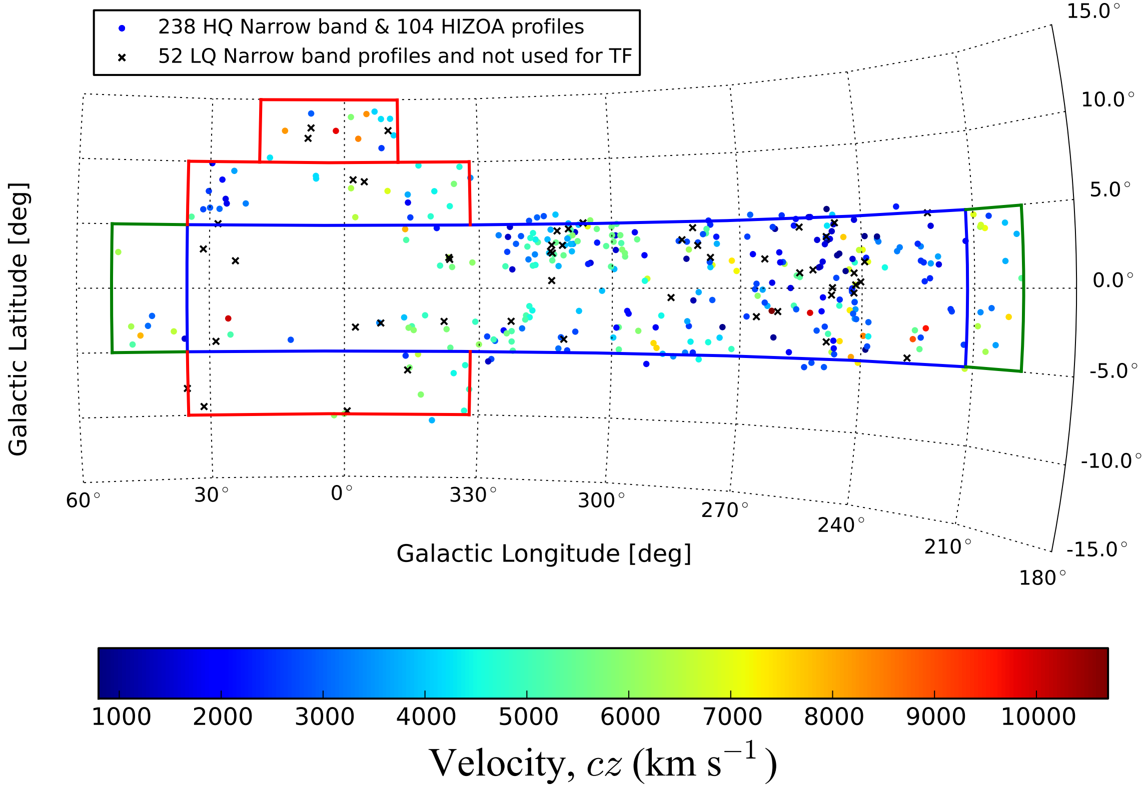

Figure 3.1: The distribution of the 394 inclined spiral galaxies in the TF sample with accurate NIR photometry shown in a zoomed-in Aitoff projection: High Quality (HQ) narrow-band observations of 238 galaxies and 104 additional HIZOA galaxies with HQ H I profiles are shown as circles colour coded by their velocity cz; Low Quality (LQ) narrow-band observations of the 52 galaxies discarded from the TF are shown as black crosses. The boundaries of the three HIZOA survey areas are plotted in blue (HIZOA-S), green (HIZOA-N) and red (GB). Note the wall-like structure of the Norma super-cluster at $290^\circ < l < 340^\circ$ and $cz \sim 4800$ km s^{-1}.

than 0.1 mag at the highest extinction level). After applying additional restrictions on inclination, we use galaxies with $b/a < 0.7$ (see also, Fig. 6 in Said et al. 2015). All the selected HIZOA profiles were visually inspected. Galaxies with good profiles were excluded from the re-observation list. Only galaxies with profiles of insufficient S/N ratio for TF work were included in the narrow-band observing list. The final list for re-observations contains 290 galaxies. An additional 104 H I profiles from the three HIZOA surveys were deemed sufficiently reliable for TF analysis and measured directly from data in the HIZOA archive.

3.2.2 Data Acquisition and Reduction

Data were collected in 2010 and 2015 using the 21 cm Multibeam receiver (MB; Staveley-Smith et al. 1996) on the 64-m Parkes Radio Telescope in narrow-band mode, using only the high-efficiency 7 inner beams. Beam-switching mode allows one beam ON the source and the other six OFF source, which reduces the noise by a factor of 2. Each target was observed for at least 35 minutes of ON-source integration time, with the 8 MHz bandwidth split into 1024 channels. This results in a velocity resolution of 1.6 km s^{-1}.

Preliminary processing of the data was done in the real time. Each galaxy was observed for at least 35 minutes to get improved sensitivity over the original HIZOA data. To avoid L3 beacon of the Global Positioning System (GPS), the integration time for sources near cz= 8300 km s^{-1} was reduced to 2×17.5 minutes. Based on an assessment of the preliminary 35 minutes integration results, some galaxies were observed for another 17.5 or 35 minutes. We used the package **LIVEDATA**[†] (Barnes et al. 2001) to correct for the bandpass and Doppler effects. Estimation of the bandpass is done by using the MEAN estimator. All spectra were converted to the Solar System barycentre. The corrected-spectra were gridded with **GRIDZILLA**[‡] (Barnes et al. 2001).

[†] This software is available in the ATNF package of AIPS++

[‡] This software is available in the ATNF package of AIPS++

3.3 H I Results

As mentioned above, the aim of this chapter is to provide H I parameters measured in a uniform way from high signal-to-noise (S/N) ratio and High Quality (HQ) profiles to be used in the forthcoming NIR TF analysis of galaxies in the ZOA. The required S/N threshold of depends on the shape of the H I profile, but S/N $\simeq 5$ appears to be minimum requirement for our algorithm (Donley et al. 2015). In this section we describe how we obtain the H I parameters required for the 394 galaxies selected for the TF ZOA relation.

Figure 3.1 shows the distribution of all 394 galaxies in the sample. The newly-observed HQ narrow-band observations of 238 galaxies and additional 104 HQ HIZOA profiles derived directly from the HIZOA surveys are shown as circles colour-coded by their velocity cz. For 52 of the re-observed galaxies, the resulting profile or signal to noise ratios was not deemed of sufficient quality for the ZOA TF analysis. These 52 (LQ) narrow-band observations are shown as black crosses. In this figure, the wall-like structure of the Norma super-cluster seems to dominate the distribution at $290^\circ < l < 340^\circ$ and $cz \sim 4800$ km s^{-1} (Kraan-Korteweg et al. 1996, Woudt et al. 1999; 2008, Mutabazi et al. 2014). See also the wedge plot (Fig. 18) in Staveley-Smith et al. (2015).

Figure 3.2 presents a quantitative comparison between the three HIZOA surveys and the TF sample presented here. The distribution of both the HIZOA sources and TF sample are shown as a function of Galactic longitude in Fig. 3.2. It shows that the TF sample is representative of the distribution of the parent HIZOA sample. The two histogram peaks around $240^\circ < l < 270^\circ$ and $300^\circ < l < 330^\circ$ in the HIZOA distribution are due to the Puppis and GA regions respectively. Both are well represented in the TF sample. The drop in both histograms towards the center of the Milky Way is due to existence of the LV. This drop is more prominent in the TF sample than the HIZOA survey because of the dependence of the TF sample on HQ NIR observations (Said et al. in prep.). In the Galactic Bulge region, not only is the stellar density high but the region is also dominated by the LV, and the sample contains a relatively larger proportion of smallish blueish dwarfs (Kraan-Korteweg et al. 2008).

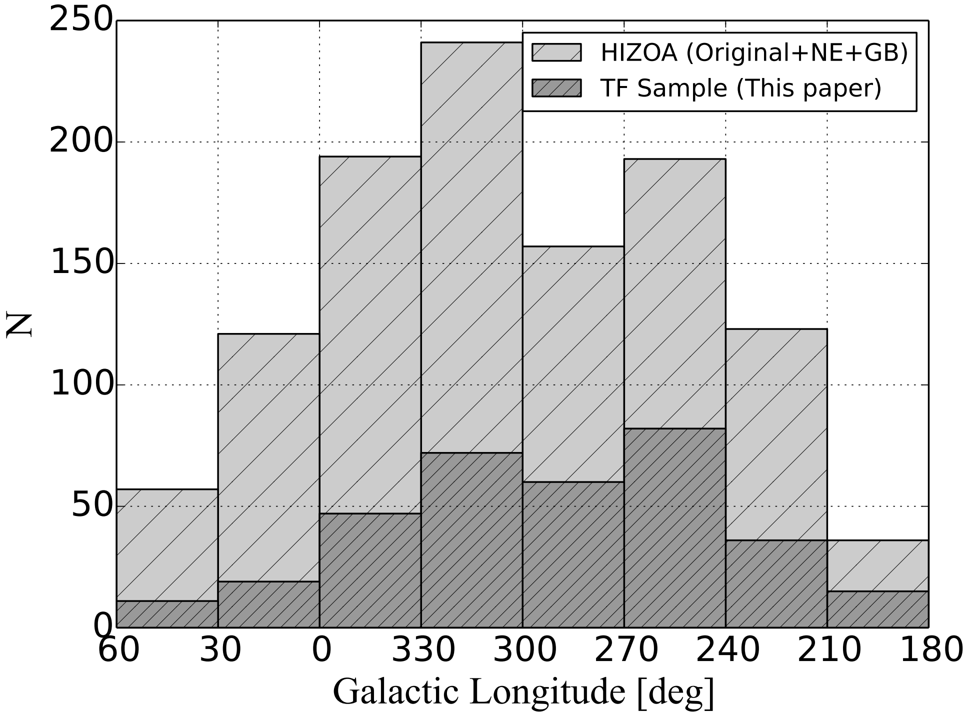

Figure 3.2: The distribution of both HIZOA (N+S+GB) and the NIR TF ZOA sample as a function of Galactic longitude. The final TF sample is representative of the three input HIZOA surveys. The two peaks around 240° $< l <$ 270° and 300° $< l <$ 330° are due to Puppis and GA respectively. The drop in both histograms around the center of the Milky Way is due to existence of the LV. This drop is more prominent in the TF sample because of the dependence on accurate NIR photometry.

3.3.1 H I Parametrization

The total flux and errors

We follow Staveley-Smith L. et al. (2015) in measuring the total flux of the H I using the function **MBSPECT** within the **MIRIAD** package (Sault et al. 1995). After applying three-channel Hanning smoothing, which results in a velocity resolution of 3.3 km s^{-1} for our spectra, a low-order polynomial was fitted and subtracted from this spectrum. The integrated line flux was then measured from this smoothed and baseline-subtracted profile by integrating across the channels containing the emission line. The error was calculated using the formula given in Koribalski et al. (2004):

$$\sigma(F_{HI}) = 4(SN)^{-1}(S_{peak}F_{HI}\delta_v)^{1/2} \tag{3.1}$$

where (SN) is the ratio of the peak flux density, S_{peak}, and its uncertainty, and $\delta_v = 3.3$ and 27 km s^{-1} are the velocity resolution of narrow-band and HIZOA observations respectively, after applying three-channel Hanning smoothing.

Systemic velocities and velocity widths

For the determination of the TF distances and peculiar velocities, the most important parameters from the H I profile are the systemic velocity and linewidth. The measurement of the H I linewidth and its associated uncertainty has received a lot of attention in the last few decades. Giovanelli et al. (1997) found the error in the H I linewidth to be the dominant source for the scatter in the TF relation. However, Tully & Pierce (2000) state that this does not hold if the error is less than 20 km s^{-1}. Subsequently, different algorithms have been introduced to measure the linewidth with high precision. Some authors adopt W_{F50}, the linewidth at 50% of the peak flux-rms (f_p−rms) measured with a polynomial fit to both sides of the profile, to be their first preference (Haynes et al. 1999, Springob et al. 2005). Courtois et al. (2009), on the other hand, compared the W_{20}, the linewidth at 20% of the peak flux of a single peak, as used in the early work (Tully & Fisher 1977, Pierce & Tully 1988) with the different linewidths from Springob et al. (2005) for an optimized choice of linewidth. They found a better correlation of W_{20} with W_{M50}, the linewidth at 50% of the mean flux, than with W_{F50}. They therefore developed an algorithm to measure the W_{m50} based on the mean flux instead of the peak level. This linewidth measurement, W_{m50}, has been used to update the Pre-Digital H I catalog of the Extragalactic Distance Database (Courtois et al. 2011, Courtois & Tully 2015).

In this chapter, we measure the systemic velocities and velocity widths using a modified version of the **GBTIDL**[§] function to find the Area, Width, and Velocity of a galaxy profile (**AWV**)[¶] (see also, Hong et al. 2013, Masters et al. 2014). This allows us to measure the linewidth values using five different methods:

1. W_{P20}: the linewidth at 20% of the peak flux−rms,

2. W_{M50}: the linewidth at 50% of the mean flux,

3. W_{P50}: the linewidth at 50% of the peak flux−rms,

4. W_{F50}: the linewidth at 50% of the peak flux−rms, measured with a polynomial fit to both sides of the profile,

5. W_{2P50}, the linewidth at 50% of the peak flux−rms measured at each of the two peaks.

The errors for the systemic velocities and velocity widths were calculated by conducting a set of simulations for each profile (see also, Donley et al. 2005, Hong et al. 2013). This was achieved in three steps:

Step 1: The Savitzky-Golay smoothing filter (Press et al. 1992) was used to smooth each galaxy profile. A smoothing width of seventeen velocity channels was used for the new narrow-band observations, while eight velocity channels were used for HIZOA profiles (e.g., Donley et al. 2005, Hong et al. 2013).

[§] GBTIDL is an interactive package for reduction and analysis of spectral line data taken with the Robert C. Byrd Green Bank Telescope (GBT) using IDL

[¶] This code adapted from code in use at Arecibo. This version was originally from Karen O'Neil and modified by adding W_{F50} option by Karen L. Masters

Step 2: Fifty simulated galaxy profiles were created for each galaxy by applying Poisson noise to the smoothed profile. The rms of the Poisson noise was adjusted to the rms of the original galaxy profile.

Step 3: A modified version of the **GBTIDL** function **AWV** was used again to measure all the parameters using the simulated spectra. The median offset between the 50 simulated spectra and the original spectrum was adopted as the error.

For 17 galaxies, the **GBTIDL** function **AWV** failed to determine the W_{F50} from the simulated spectra. For these galaxies, we used the formula proposed by Masters et al. (2014):

$$\epsilon_{WF50} = \sqrt{(rms/a_l)^2 + (rms/a_r)^2} \tag{3.2}$$

where a_l and a_r are the slopes of the fit on the left and right edge of the profile. This error was converted to the Monte Carlo simulation error using

$$\epsilon_{MC} = 0.815 + 0.405\epsilon_{WF50} \tag{3.3}$$

also proposed by Masters et al. (2014).

Figure 3.3 shows two examples of H I profiles in our sample measured with five different linewidth fitting algorithms. The profile on the left presents one of the newly observed galaxies with the narrow-band. The right profile is based on the HIZOA data but re-processed with the same method for the narrow-band observations. Figure 3.3 reveals good agreement within the uncertainty of W_{P20}, and W_{M50} and also between W_{F50} and W_{2P50}.

To expand on this statement, we plot in Fig. 3.4 the five linewidth measurements against each other and determine their respective correlations. The strongest correlation was found between W_{P20} and W_{M50} which confirms the results of Courtois et al. (2009). We also found good agreement between W_{F50} and W_{2P50}. In contrast, a significant offset was found between W_{M50} and W_{F50} which also agrees with what was found by Courtois et al. (2009).

To quantify the correlations between the five linewidth measurements, we

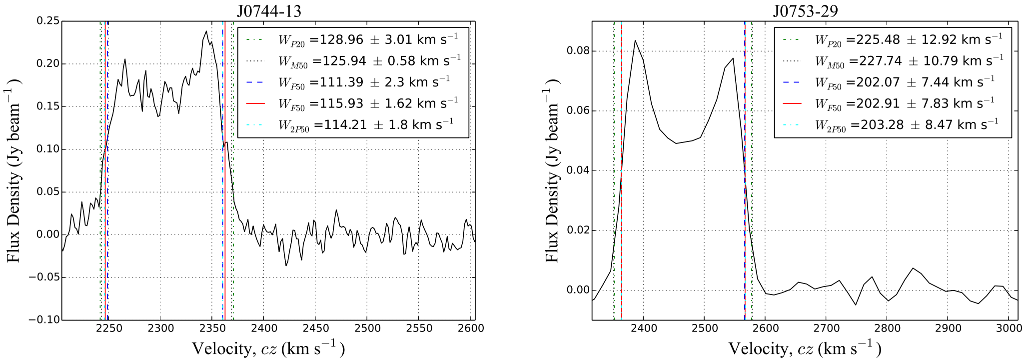

(a) (b)

Figure 3.3: Two examples of H I profiles in our sample measured with five different linewidth algorithms: (a) new narrow-band observations with velocity resolution of 3.3 km s^{-1}; (b) existing HIZOA data of a good H I profile, with a velocity resolution of 27 km s^{-1}. The solid red lines represents our preferred linewidth measurement W_{F50}. Figures for the entire sample are available online.

used the Pearson's sample correlation coefficient

$$r = \frac{\sum_{i=1}^{n}(x_i - \bar{x})(y_i - \bar{y})}{\sqrt{\sum_{i=1}^{n}(x_i - \bar{x})^2}\sqrt{\sum_{i=1}^{n}(y_i - \bar{y})^2} \tag{3.4}$$

with $-1 \leq r \leq 1$, where $r \sim -1$ indicates a perfect anti-correlation and for uncorrelated parameters $r \sim 0$, while $r \sim 1$ means a strong positive correlation. Table 3.1 shows the resulting Pearson's sample correlation coefficient correlation matrix. The best two correlations in Table 3.1 are between W_{P20} and W_{M50} and between W_{F50} and W_{2P50} where $r = 0.993$ for both of them. The least correlated linewidths are W_{M50} and W_{P50} where $r = 0.932$. Based on the values of r, W_{F50} comes out to be the most stable parameter with average correlation of $\bar{r}_{WF50} = 0.975$ with the four other linewidths. This is ideal because it is also the linewidth used in our calibration of an isophotal NIR TF relation which is optimal for use in the ZOA (Said et al. 2015)

In addition to the preferred linewidth W_{F50}, we provide the derived conversion equations between all the five linewidths. These conversion equations are derived using a Bayesian mixture model with more parameters than the data points (see also, Hogg et al. 2010, Ivezić et al. 2014). The advantage

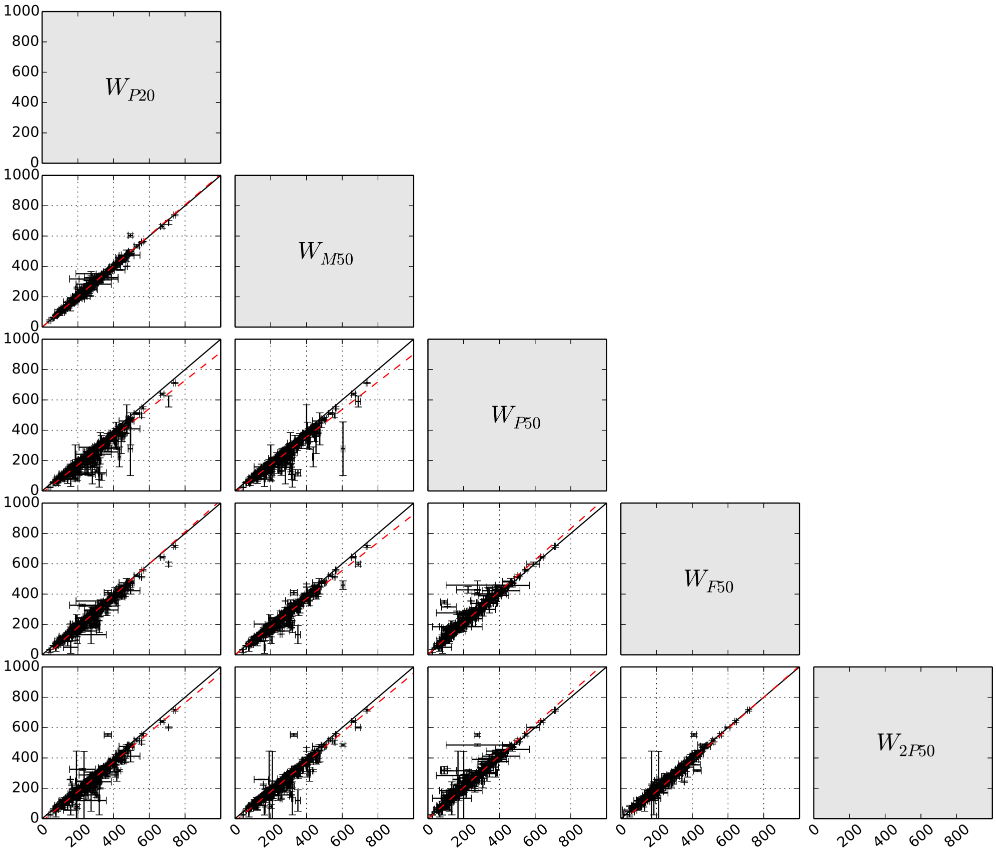

Figure 3.4: A matrix of pairwise plots of the five linewidth measurements. The solid line shows the one-to-one relation, while the dashed red line is the best fit model to the data. Almost perfect correlation was found between W_{P20} and W_{M50} also between W_{F50} and W_{2P50} (within the uncertainty). A large offset was found between the two most used linewidths in the TF analysis W_{M50} and W_{F50}.

Table 3.1: The Pearson's sample correlation coefficient r. The correlation coefficient clearly identifies W_{F50} as the most stable linewidth with average correlation of $\bar{r}_{WF50} = 0.975$ with the four other linewidths and therefore the optimal choice for TF analysis.

linewidth type	W_{P20}	W_{M50}	W_{P50}	W_{F50}	W_{2P50}
W_{P20}	1.000				
W_{M50}	0.993	1.000			
W_{P50}	0.947	0.932	1.000		
W_{F50}	0.978	0.974	0.953	1.000	
W_{2P50}	0.973	0.970	0.956	0.993	1.000

of using a Bayesian mixture model is two-fold; it is less sensitive to outliers compared to the simple maximum likelihood approach, and it does not exclude them completely as happens with the sigma-clipping procedure. This model was computed with the Python MCMC Hammer **emcee**[‖] (Foreman-Mackey et al. 2013). The 10 conversion formulae are given in Eqs. 3.5:

$$
\begin{aligned}
W_{M50} &= -0.287(\pm 0.086) + 1.0089(\pm 0.0003)W_{P20}, && \text{(3.5a)}\\
W_{P50} &= -14.177(\pm 0.066) + 0.9287(\pm 0.0003)W_{P20}, && \text{(3.5b)}\\
W_{P50} &= -9.053(\pm 0.065) + 0.9106(\pm 0.0003)W_{M50}, && \text{(3.5c)}\\
W_{F50} &= -27.999(\pm 0.181) + 1.0474(\pm 0.0008)W_{P20}, && \text{(3.5d)}\\
W_{F50} &= -0.130(\pm 0.173) + 0.9261(\pm 0.0007)W_{M50}, && \text{(3.5e)}\\
W_{F50} &= 2.554(\pm 0.155) + 1.0382(\pm 0.0007)W_{P50}, && \text{(3.5f)}\\
W_{2P50} &= -17.293(\pm 0.172) + 0.9765(\pm 0.0009)W_{P20}, && \text{(3.5g)}\\
W_{2P50} &= -17.293(\pm 0.181) + 0.9767(\pm 0.0009)W_{M50}, && \text{(3.5h)}\\
W_{2P50} &= -1.400(\pm 0.160) + 1.0380(\pm 0.0009)W_{P50}, && \text{(3.5i)}\\
W_{2P50} &= -27.280(\pm 0.152) + 1.0341(\pm 0.0008)W_{F50}. && \text{(3.5j)}
\end{aligned}
$$

Before using any of these linewidths in a TF application, four corrections need to be applied to obtain the more physical rotational velocity, namely: the instrumental resolution correction, the cosmological redshift correction, and the correction for the effect of turbulent motion and inclination. We will apply these four corrections in the forthcoming TF analysis.

3.3.2 H I Catalog

The H I catalog and plots of the H I spectra are available electronically. Figure 3.3 and Tables 3.2 & 3.3 present examples of the H I profiles and catalog. The H I parameters listed in the two catalogs are:

Column (1) - HIZOA ID as reported in the HIZOA survey publications (Donley et al. 2005; Staveley-Smith et al., 2015; Kraan-Korteweg et al., in

---

[‖] http://dan.iel.fm/emcee/current/

prep.).

Columns (2 and 3) - Right Ascension (RA) and Declination (Dec.) in the J2000.0 epoch of the fitted position in HIZOA.

Columns (4 and 5) - Galactic coordinates.

Column (6) - I, Integrated H I flux and associated error.

Column (7) - Heliocentric velocity V_{hel} (cz) measured as the mid-point of the 50% of the profile using the W_{F50} algorithm and associated error.

Column (8) - W_{P20}, the linewidth at 20% of the peak flux-rms and associated error.

Column (9) - W_{M50}, the linewidth at 50% of the mean flux and associated error.

Column (10) - W_{P50}, the linewidth at 50% of the peak flux-rms and associated error.

Column (11) - W_{F50}, the linewidth at 50% of the peak flux-rms measured with a polynomial fit to both sides of the profile and associated error.

Column (12) - W_{2P50}, the linewidth at 50% of the peak flux-rms measured at each of the two peaks and associated error.

Column (13) - rms noise.

Column (14) - Signal-to-noise ratio (S/N).

3.3.3 Characteristics of the Current Data

An overview of the H I parameters (divided into two sub-samples) is given in Fig. 3.5, which shows histograms of the linewidth at 50% of the peak flux−rms measured after fitting polynomials to both sides of the profile W_{F50}, the error on the linewidth ϵ_{WF50}, the heliocentric velocity V_{hel}, the rms noise, the logarithmic integrated line flux and the logarithmic signal-to-noise ratio.

The distribution of galaxies with linewidths $W_{F50} > 150$ km s^{-1} is similar to the distribution of the overall HIZOA catalogue (see also Fig. 2 in Staveley-Smith et al., 2015). The fraction of low-linewidth galaxies in the TF sample is significantly lower. That is to be expected because these profiles generally originate from dwarf galaxies which often have no clear disks, hence uncertain inclinations, and low S/N. They are also less likely to have a NIR counterpart.

Table 3.2: H I derived parameters for the good HIZOA profiles (velocity resolution of 27 km s^{-1}). The full table is available online.

H I Name	RA	DEC	l	b	I	v_{hel}	W_{P20}	W_{M50}	W_{P50}	W_{F50}	W_{2P50}	rms	SNR
	(J2000)		[deg]		Jy km s^{-1}			km s^{-1}				[mJy]	
(1)	(2)	(3)	(4)	(5)	(6)	(7)	(8)	(9)	(10)	(11)	(12)	(13)	(14)
J0653-03A	06 53 21.1	-03 53 32	216.6146	-1.3488	8.2 ± 1.0	2566.43 ± 2.90	290.356 ± 9.42	282.72 ± 8.13	181.06 ± 4.51	190.67 ± 3.19	181.06 ± 7.24	3.7	13.9
J0700-11	07 00 58.1	-11 47 17	224.5099	-3.2637	18.5 ± 0.7	2744.06 ± 1.62	449.90 ± 13.19	452.45 ± 9.69	424.85 ± 10.00	426.76 ± 9.25	426.80 ± 10.07	2.3	33.4
J0705-12	07 05 39.9	-12 59 55	226.1123	-2.7952	5.8 ± 0.7	5455.80 ± 2.20	222.06 ± 18.49	222.99 ± 15.81	206.61 ± 10.79	209.77 ± 4.30	208.88 ± 10.54	3.0	13.9
J0709-05	07 09 34.2	-05 24 14	219.8091	1.5520	14.4 ± 1.2	1720.60 ± 4.36	311.59 ± 1.74	305.04 ± 4.79	273.74 ± 2.70	279.29 ± 2.90	273.74 ± 2.79	3.8	16.5
J0717-08	07 17 40.6	-08 55 25	223.8612	1.7025	7.0 ± 0.8	2460.64 ± 4.45	201.84 ± 4.59	205.05 ± 3.62	178.40 ± 4.25	187.15 ± 17.97	178.40 ± 4.25	3.4	15.0
J0722-09	07 22 47.2	-09 01 54	224.5481	2.7670	9.0 ± 1.2	3338.34 ± 4.83	219.51 ± 22.20	231.46 ± 21.04	187.63 ± 10.82	181.50 ± 20.73	187.63 ± 10.82	4.5	13.1
J0724-09	07 24 57.5	-09 39 18	225.3511	2.9460	56.7 ± 0.7	2438.02 ± 2.32	203.50 ± 13.66	211.72 ± 11.86	178.45 ± 6.33	220.53 ± 17.65	178.45 ± 6.33	2.7	130.5
J0725-24A	07 25 16.4	-24 28 19	238.4486	-3.9987	57.5 ± 0.8	796.53 ± 0.36	195.95 ± 0.43	257.60 ± 5.64	131.04 ± 3.98	135.94 ± 0.16	131.04 ± 3.98	3.0	125.2
J0725-24B	07 25 16.5	-24 57 20	238.8765	-4.2258	10.8 ± 0.8	2761.76 ± 2.12	266.37 ± 16.29	267.44 ± 14.38	244.33 ± 5.19	245.66 ± 7.51	246.71 ± 6.29	2.9	19.6
J0727-23	07 27 31.3	-23 57 48	238.2420	-3.3068	18.7 ± 0.9	4391.43 ± 1.00	442.93 ± 9.04	445.06 ± 6.70	417.02 ± 6.70	420.80 ± 8.78	420.06 ± 9.18	2.9	26.2

Table 3.3: H I derived parameters for the narrow-band profiles (velocity resolution of 3.3 km s^{-1}). The full table is available online.

H I Name	RA	DEC	l	b	I	v_{hel}	W_{P20}	W_{M50}	W_{P50}	W_{F50}	W_{2P50}	rms	SNR
	(J2000)		[deg]		Jy km s^{-1}			km s^{-1}				[mJy]	
(1)	(2)	(3)	(4)	(5)	(6)	(7)	(8)	(9)	(10)	(11)	(12)	(13)	(14)
J0744-13	07 44 29.5	-13 03 58	230.6608	5.4984	21.9 ± 0.7	2304.82 ± 0.44	128.96 ± 3.01	125.94 ± 0.58	111.39 ± 2.30	115.93 ± 1.62	114.21 ± 1.80	10.3	23.14
J0744-25	07 44 26.4	-25 59 20	241.8791	-0.9424	2.1 ± 0.3	4048.62 ± 12.66	182.10 ± 2.28	174.57 ± 6.76	131.00 ± 45.66	170.17 ± 12.55	150.57 ± 2.78	4.4	6.44
J0744-26	07 44 23.4	-26 01 48	241.9092	-0.9725	8.8 ± 0.5	2728.33 ± 0.74	318.23 ± 1.37	309.14 ± 1.92	288.18 ± 9.41	285.73 ± 12.41	268.52 ± 34.02	5.4	9.02
J0744-27	07 44 55.4	-27 21 10	243.1148	-1.5301	3.5 ± 0.4	7272.13 ± 7.54	313.30 ± 2.10	314.20 ± 3.41	252.10 ± 51.65	267.42 ± 40.15	273.47 ± 12.98	5.6	6.17
J0747-21	07 47 19.7	-21 37 9	238.4298	1.8211	2.9 ± 0.4	6969.20 ± 3.39	123.33 ± 9.66	120.45 ± 0.32	106.60 ± 9.57	108.67 ± 16.82	107.35 ± 31.65	6.0	7.32
J0748-25B	07 48 33.6	-25 14 35	241.7011	0.2355	5.2 ± 0.6	6813.39 ± 6.13	387.72 ± 11.11	387.31 ± 8.30	359.04 ± 26.94	381.84 ± 24.89	375.88 ± 14.65	6.5	4.55
J0749-21	07 49 21.4	-21 53 6	238.8975	2.0935	2.9 ± 0.4	2338.38 ± 0.33	192.44 ± 0.08	182.80 ± 2.00	165.54 ± 15.94	179.23 ± 6.77	174.32 ± 11.21	5.7	5.59
J0749-26B	07 49 21.0	-26 12 17	242.6205	-0.0983	13.0 ± 0.5	2490.82 ± 1.42	328.04 ± 10.59	313.38 ± 0.07	279.72 ± 8.94	296.52 ± 4.76	288.81 ± 2.63	4.4	13.74
J0750-32	07 50 39.7	-32 49 19	248.4695	-3.2120	5.0 ± 0.4	5130.45 ± 0.36	329.91 ± 6.04	320.56 ± 0.33	290.53 ± 7.32	307.97 ± 13.66	303.12 ± 6.95	4.3	7.68
J0751-37	07 51 28.0	-37 13 4	252.3550	-5.2946	12.4 ± 0.5	2805.47 ± 0.28	101.69 ± 2.71	99.19 ± 2.60	79.94 ± 3.18	85.73 ± 0.30	85.97 ± 1.49	8.4	18.78

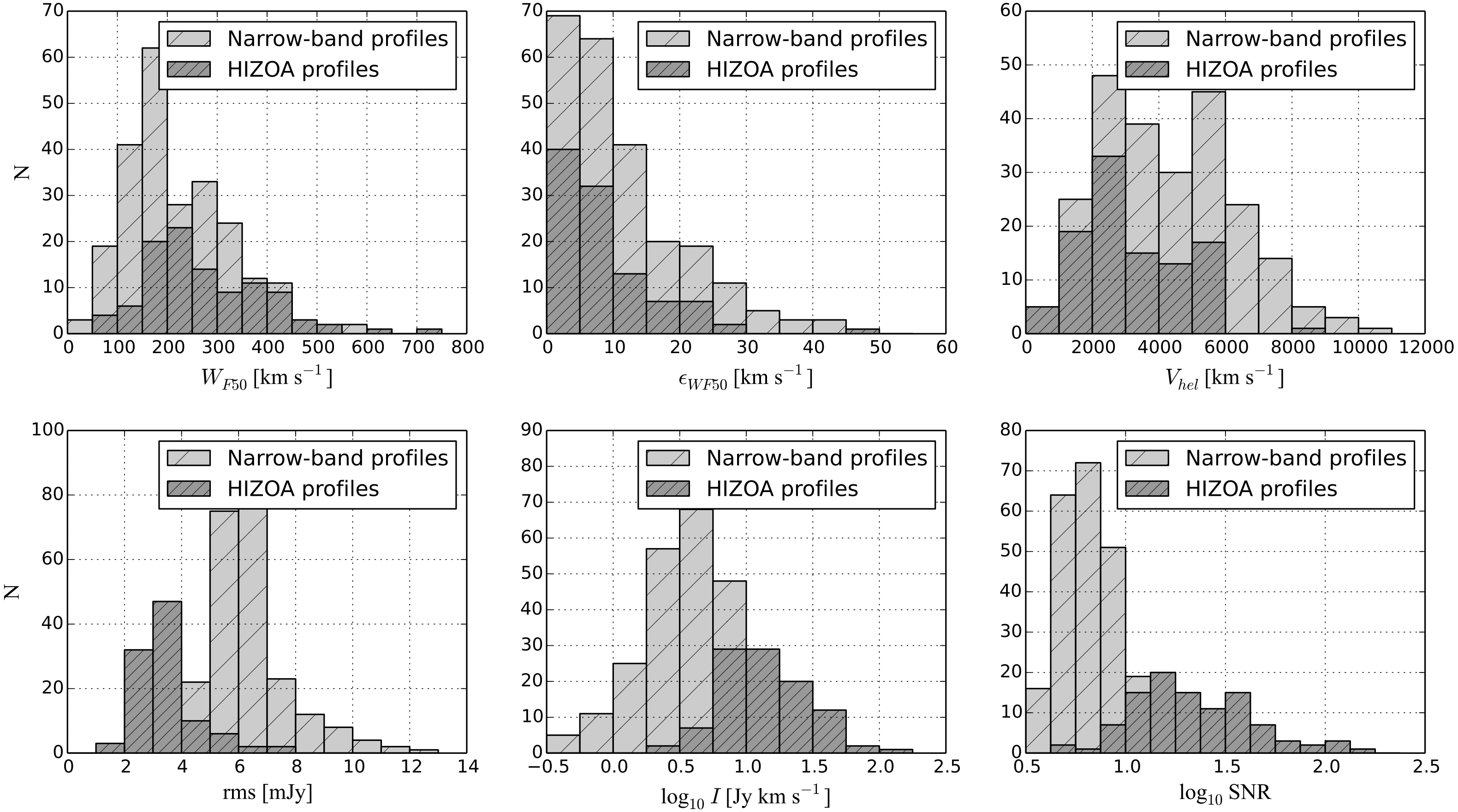

Figure 3.5: Histograms of the H I parameters for the whole TF sample divided into two sub-samples (238 narrow band profiles and 104 HIZOA profiles); the linewidth at 50% of the peak flux−rms measured after fitting polynomials to both sides of the profile W_{F50}, the error on the linewidth ϵ_{WF50}, the heliocentric velocity V_{hel}, the rms noise, logarithmic integrated line flux and logarithmic signal-to-noise ratio.

The scatter in the TF relation for these low-linewidth galaxies is much higher and they are preferentially excluded from TF applications.

The distribution of the associated linewidth error ϵ_{WF50} in Fig. 3.5 shows that 95% and 84% of our sample have errors less than 30 km s^{-1} and 20 km s^{-1}, respectively.

The distribution of the heliocentric velocity V_{hel} shows the peaks that are indicative of the Puppis and GA overdensities, but they are not quite as pronounced as in the HIZOA data. There is a clear drop in the number of detected galaxies for reliable TF analysis beyond 7000 km s^{-1}, compared to the full HIZOA data set. Only 24 galaxies (7%) of the sample have $V_{hel} > 7000$ km s^{-1}. Galaxies beyond 7000 km s^{-1} on average have lower S/N ratios given their large distances.

The average rms noise for our sample is 5.5 mJy and the majority (92%) have rms < 8.0 mJy. A histogram of the logarithmic value of the integrated line flux is also shown in Fig. 3.5. The final histogram in Fig. 3.5 shows the distribution of the logarithmic value of the signal-to-noise ratio. The average value of the signal-to-noise ratio of our sample is 14.7 with a median value of 7.9, which is adequate for the TF analysis.

In Fig. 3.5, the 104 HIZOA profiles have higher S/N ratio than the new narrow band observations. This is expected because the narrow-band observing list contains only galaxies with weaker HIZOA profiles of insufficient S/N ratio for the TF work.

3.3.4 Comparison with published H I data

In this section we provide an extensive comparison of the newly measured linewidths and the published linewidths. We used the two published parts of the HIZOA survey (HIZOA-S; Staveley-Smith et al., 2015 and HIZOA-N; Donley et al. 2005). After excluding galaxies from the GB extension, the number of galaxies used in this comparison becomes 307 galaxies.

Figure 3.6 shows a comparison between linewidths at 50% of the peak flux measured in this work against its counterpart measurements in HIZOA surveys. In Fig. 3.6, we divided the whole sample into three sub-sample: (1) the new narrow band observations, (2) HIZOA profiles (same spectra) and (3) The northern extinction profiles (HIZOA-N). Good agreement for most of the

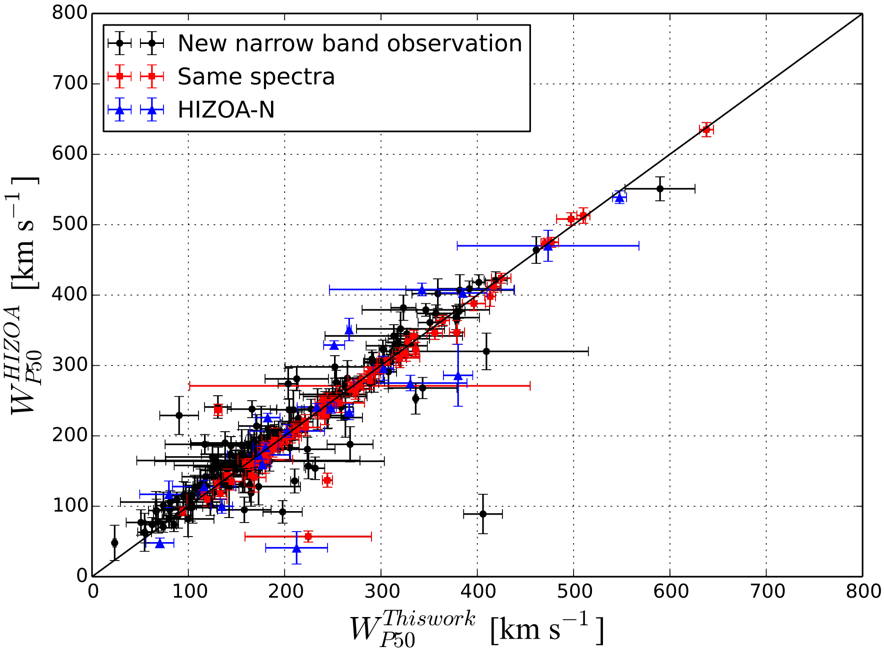

Figure 3.6: A comparison between W_{P50} measured in this work using a modified version of the GBTIDL function AWV and W_{P50} measured in HIZOA surveys using MIRIAD task MBSPECT. The solid line shows the one-to-one relation.

Table 3.4: List of galaxies with offset larger than 50 km s^{-1}

H I Name	$W_{P50}^{Thiswork}$	W_{P50}^{HIZOA}	offset
J0623+14	380 ± 15	286 ± 44	94
J0635+02	212 ± 32	41 ± 23	171
J0635+11	342 ± 96	408 ± 9	-65
J0635+14A	330 ± 58	275 ± 11	55
J0653+07	251 ± 10	329 ± 6	-77
J0704-13	197 ± 20	92 ± 18	105
J0722-05	130 ± 13	241 ± 16	-110
J0730-25	336 ± 1	253 ± 23	83
J0752-29	166 ± 25	238 ± 14	-71
J0753-22	231 ± 9	154 ± 18	77
J0808-35	409 ± 50	320 ± 26	89
J0821-39	267 ± 23	188 ± 25	79
J0858-45A	343 ± 35	268 ± 15	75
J0859-52	210 ± 4	136 ± 18	74
J1012-62	90 ± 20	229 ± 27	-138
J1045-64	323 ± 13	382 ± 18	-58
J1052-64	158 ± 27	95 ± 18	63
J1125-60	224 ± 4	157 ± 19	67
J1149-64	117 ± 41	188 ± 14	-70
J1339-57	212 ± 32	281 ± 17	-68
J1419-57	138 ± 35	190 ± 16	-51
J1624-45A	203 ± 10	274 ± 22	-70
J1625-55	405 ± 20	89 ± 28	316
J1929+11	266 ± 2	351 ± 16	-84
J0858-39	224 ± 65	57 ± 8	167

galaxies are shown clearly in this figure. Measurements from the same spectra, shown as red squares, are almost identical. Our new measurements are slightly different from the HIZOA-N (blue triangles). In Table 3.4 we list all galaxies with offsets larger than 50 km s^{-1}. Table 3.4 also shows the newly measured, the published linewidth with the associated error for each measurement and the offset for each galaxy.

The main reason for these offsets is the difference in the velocity resolution between the narrow band (3.3 km s^{-1}) and the HIZOA (27 km s^{-1}) data. This is shown clearly in the most notable offset (316 km s^{-1}, for J1625$-$55). This galaxy is measured in the narrow band observations to have $W_{P50} = 405$ km

s^{-1}, which agrees within the uncertainty in the measurement of the same galaxy in the HICAT catalog (Meyer et al. 2004) which was $W_{P50} = 453$ km s^{-1}. In contrast, the same galaxy was measured in the HIZOA-S catalog to have W_{P50} of 89 km s^{-1} because one of the two peaks dominate their signal. This can be further explained by looking at the W_{P20} in the three surveys (narrow-band, HICAT and HIZOA-S) which all agree within the uncertainty. All other notable offsets listed in Table 3.4 can be explained in a similar manner.

Another comparison with the HIPASS catalog (Koribalski et al. 2004) is shown in Fig. 3.7.

The left panel of this plot shows a comparison between W_{P50} measured in this work on the x-axis and W_{P50} measured in HIPASS survey on the y-axis for the 28 galaxies in common. As expected, a perfect agreement between both measurements are shown because these galaxies are among the brightest galaxies in the HIPASS survey. Two galaxies, J1059-66 & J1149-64, both show a notable offset. They are identified by name on the left panel of the figure itself. The profiles of these two galaxies are displayed in the right panel of the plot. They demonstrate quite well why there is such a large difference: in both cases one of the two peaks is more prominent than the other peak in these lob-sided profiles.

3.4 Summary

In this chapter, we present H I observations for 394 inclined spiral galaxies in the southern ZOA. Parameters were determined in a systematic way for applications of the TF relation in the ZOA. New observations for 290 galaxies in the sample were conducted in 2010 and 2015 with the 7 inner beams of the multibeam receiver on the Parkes 64 m Radio Telescope. Three-channel Hanning smoothing was applied to the spectra, resulting in a velocity resolution of 3.3 km s^{-1} for our newly observed sample. The additional 104 galaxies were measured directly from the existing HIZOA data. The final sample contains 342 galaxies with adequate signal-to-noise ($S/N > 5$) and an H I profiles suitable for TF analysis. The average value of the signal-to-noise ratio of the final sample is 14.7 with a median value of 7.9. A modified version of the **GBTIDL** function **AWV** was used to measure the systemic velocities and ve-

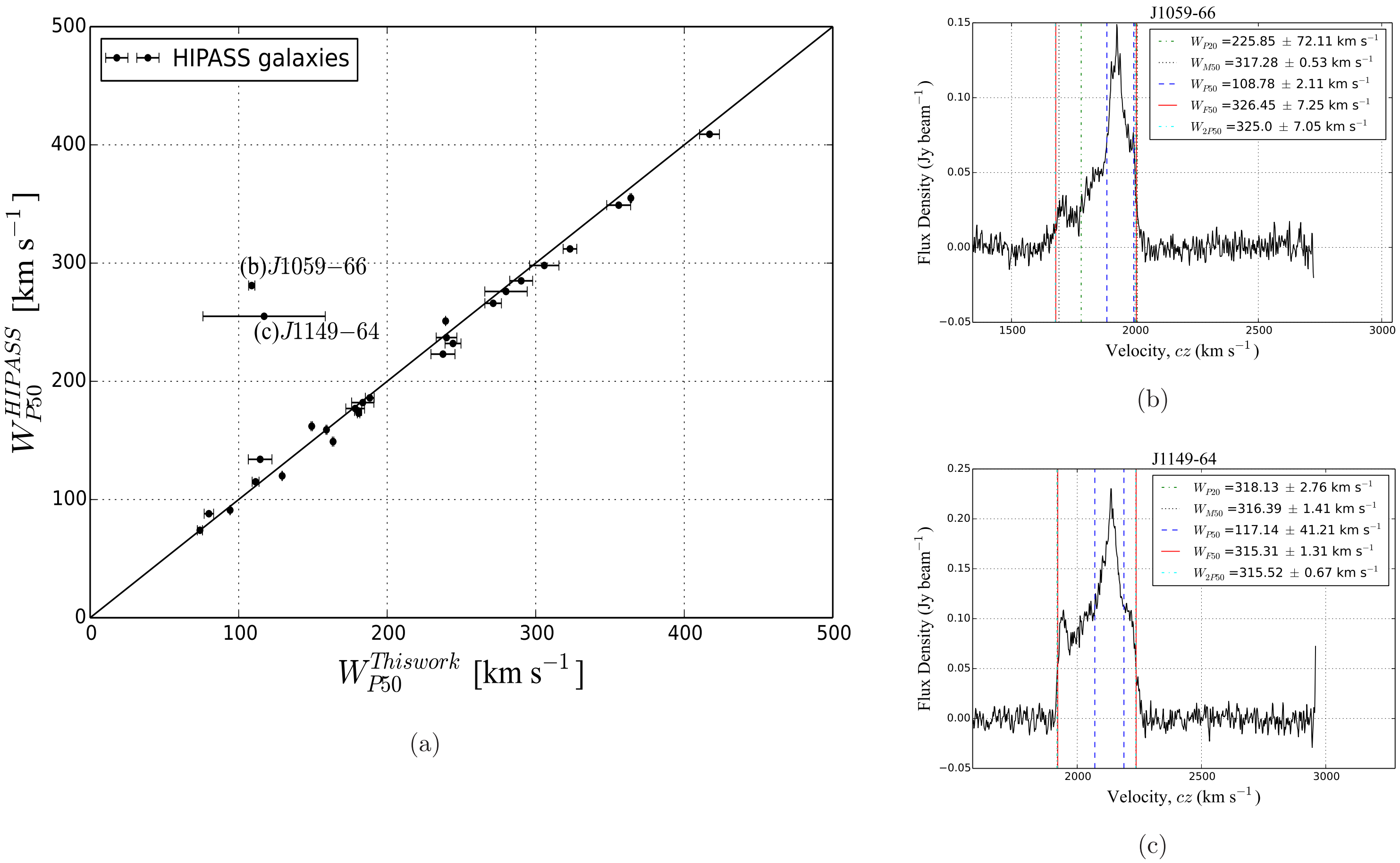

(a)

(b)

(c)

Figure 3.7: A comparison between W_{P50} measured in this work using a modified version of the GBTIDL function AWV and W_{P50} measured in HIPASS survey using MIRIAD task MBSPECT. The solid line shows the one-to-one relation.

locity linewidths based on five different methods. Good agreement was found, within the uncertainty, between W_{P20}, the linewidth at 20% of the peak flux-rms and W_{M50}, the linewidth at 50% of the mean flux. A larger offset was found between both of these linewidth values and W_{F50}, the linewidth at 50% of the peak flux-rms measured with a polynomial fit to both sides of the profile. Also, W_{F50}, the linewidth at 50% of the peak flux-rms and W_{2P50}, the linewidth at 50% of the peak flux-rms measured at each of the two peaks seem to agree within the uncertainty. The Pearson's sample correlation coefficient was used to quantify the correlation between all derived linewidths. Conversion equations between these five linewidths were derived using a Bayesian mixture model to avoid any bias toward the outliers.

In a forthcoming chapter, we will present the accompanying final high-quality NIR J, H, and K_s-band photometry that has been obtained for all galaxies in the HIZOA surveys. In that chapter we will also discuss the completeness of the NIR catalog in the ZOA and the reliability of the photometry with regard to the determinations of peculiar velocities from the NIR TF application.

The H I data presented in this chapter, the NIR data (next chapter) and the newly calibrated TF relation (Said et al. 2015) will be used to measure the flow fields in the ZOA. This will be the first measurement of the flow fields in the ZOA and should improve the assessment of the actual overdensity of the so far hidden large-scale structures, in particular for the GA region. This work should also be regarded as a precursor to the forthcoming Widefield ASKAP L-band Legacy All-sky Blind surveY (WALLABY)[**] and its sister in the northern hemisphere, the Westerbork Northern Sky HI Survey (WNSHS)[††] which will provide an HI survey of the whole sky (Duffy et al. 2012). This work can be regarded as a pilot project as well to the determination of flow fields as close as possible to the Galactic Plane, given the forthcoming deep NIR photometry from surveys such as UKIDSS and VISTA (Emerson et al. 2004, Hewett et al. 2006, Lucas et al. 2008).

[**] http://www.atnf.csiro.au/research/WALLABY/proposal.html

[††] http://www.astron.nl/ jozsa/wnshs/

Chapter 4

Deep NIR catalogue of the HIZOA galaxies

We present a deep near-infrared (NIR; J, H, and K_s bands) photometric catalogue of sources from the Parkes H I Zone of Avoidance (HIZOA) survey, which forms the basis for an investigation of the matter distribution in the Zone of Avoidance. Observations were conducted between 2006 and 2013 using the Infrared Survey Facility (IRSF), a 1.4-m telescope situated at the South African Astronomical Observatory site in Sutherland. The images cover all 1108 HIZOA detections and yield 915 galaxies. An additional 105 bright 2MASS galaxies in the southern ZOA were imaged with the IRSF, resulting in 129 galaxies. The average K_s-band seeing and sky background for the survey are 1.38 arcsec and 20.1 mag, respectively. The detection rate as a function of stellar density and dust extinction is found to depend mainly on the H I mass of the H I detected galaxies, which in principle correlates with the NIR brightness of the spiral galaxies. The measured isophotal magnitudes are of sufficient accuracy (errors ~ 0.02 mag) to be used in a Tully-Fisher analysis. In the final NIR catalogue, 285 galaxies have both IRSF and 2MASS photometry (180 HIZOA plus 105 bright 2MASX galaxies). The K_s-band isophotal magnitudes presented in this chapter agree, within the uncertainties, with those reported in the 2MASX catalogue. Another 30 galaxies, from the HIZOA northern extension, are also covered by UKIDSS Galactic Plane Survey (GPS) images, which are one magnitude deeper than our IRSF images. A modified version of our photometry pipeline was used to derive the photometric parameters of these UKIDSS galaxies. Good agreement was found between the respective K_s-band isophotal magnitudes. These comparisons confirm the robustness of the isophotal parameters and demonstrate that the IRSF images do not suffer from foreground contamination, after star removal, nor under-estimate the isophotal fluxes of ZoA galaxies.

4.1 Introduction

At low Galactic latitude NIR wavelengths are preferred over optical wavelengths because of the ability of NIR radiation to penetrate through dust. The NIR also provides a more stable indicator of total stellar mass (Kraan-Korteweg & Lahav 2000, Kraan-Korteweg 2005). In the last few decades many surveys have used the NIR to unveil the LSS hidden behind the Milky Way. The 2MASS extended source catalogue (2MASX) contains galaxies that have never been seen before in the ZOA (Jarrett et al. 2000). Jarrett et al. (2000) present new extended sources in the ZOA at Galactic longitude between 40° and 70°. Deeper NIR observations have been used specifically for dedicated surveys in the ZOA. Nagayama et al. (2004) used the same instrument that we have used in this work to conduct a NIR survey around the radio galaxy PKS1343-601. They detected 19 galaxies and another 38 galaxy candidates of which only three were known previously. Woudt et al. (2005) also used the IRSF to obtain deep photometry for 76 galaxies which was used in the determination of the distance to the Norma cluster. Nagayama et al. (2006) used a deep NIR survey of a luminous cluster in the GA region and identified 111 galaxy candidates. Longer wavelengths are also used in the ZOA; Jarrett et al. (2007) used mid-infrared wavelengths to unveil two galaxies in the GA region. A large deep NIR survey of the Norma Wall (NWS: Riad et al. 2010, Riad 2010, Kraan-Korteweg et al. 2011; Riad et al,. in prep) was also conducted with the IRSF. This survey resulted in a catalogue of 4360 galaxies with completeness limits of 15.6, 15.3 and 14.8 mag in the J, H, and K_s bands, respectively. Given the success of these surveys, we started a follow-up NIR survey of the HIZOA galaxies in the southern ZOA using the same telescope and instrument (IRSF).

This chapter is organized as follows. Section 4.2 discusses the observations, calibration and observatory site conditions. The final extended source catalogue and parameter characterization are presented in Section 4.3. Completeness as a function of dust extinction and stellar density is discussed in detail in Section 4.4. Comparison of the resulting photometry with the 2MASS and UKIDSS surveys is presented in Section 4.5. We summarise our results in Section 4.6. All magnitudes are quoted in the Vega System.

4.2 Observations

Deep NIR follow-up observations of all HIZOA galaxies were conducted with the Infrared Survey Facility (IRSF), a 1.4-m telescope situated at the South African Astronomical Observatory (SAAO) site in Sutherland, South Africa. The Simultaneous 3-colour (J, H, and K_s) Infrared Imager for Unbiased Survey (SIRIUS; Nagayama et al. 2003) camera on the IRSF has a field of view of 7.7×7.7 arcmin^2 (ideally suited for HIZOA follow-up given the 4 arcmin positional accuracy of the H I detections) with a pixel scale of 0.45 arcsec pixel^{-1} compared to 2.0 arcsec pixel^{-1} for 2MASS (Skrutskie et al. 2006). A pilot project and the first results of the catalogue were published by Williams et al. (2014) who presented photometry for 557 galaxies in the HIZOA catalogue with $cz \leq 6000$ km s^{-1}. For completion we have included their 578 fields in the current study.

An additional 105 2MASX fields in the southern ZOA but not in the HIZOA survey were also observed. The H I spectral line data for these 105 2MASX fields are from Parkes observations and available either from the 2MASS TF Survey (Hong et al. 2013) or from Said et al. (in prep.). These additional galaxies are all the bright ($K_s^\circ = 11.25$ mag), edge-on ($b/a = 0.5$) 2MASX galaxies in the southern ZOA ($5^\circ \leq |b| \leq 10^\circ$).

4.2.1 Data acquisition

Data acquisition started in 2006 and was completed by 2013, resulting in deep NIR imaging of all the HIZOA targets. The images have exposure times of 10 min, and are 2 mag deeper than 2MASS in the K_s-band (Riad 2010). We used the dithering technique to overcome the problem of faulty pixels in the NIR

Table 4.1: IRSF observations and the Observer In Charge (OIC). OIC: Wendy Williams (WW), Tom Mutabazi (TM) and Khaled Said (KS).

Year	Month(s)	Allocated weeks	No. of fields	OIC
2006-2008			101	
2009	March/April	2	249	WW
2009	March/April	2	67	WW
2010	June/July	3	138	WW
2012	May	2	231	TM
2013	April	3	430	KS

detector. We repeated a 24 s exposure 25 times with a dithering step of 15 arcsec. This dithering resulted in increasing the final image size to 8.6 × 8.6 arcmin^2. A total of 12 weeks were allocated to this project starting in 2009. 101 fields were observed between 2006 and 2008 as part of other projects to test the feasibility of this project. Table 4.1 shows the observations, number of allocated weeks, number of fields observed and the Observer In Charge (OIC). Substantial time was lost during the 2009 and 2010 runs due to bad weather and cooling system problems.

4.2.2 Data reduction and calibration

The primary data reduction, including dark frame subtraction, flat field correction, sky-subtraction, dither combination and astrometric and photometric calibration, was carried out using the pipeline software for SIRIUS[*].

4.2.3 Observatory site conditions and quality control

Figs 4.1 and 4.2 show the distributions of the K_s-band seeing and the deviation of magnitude zero point from the mean, respectively, for the 1229 observed fields as a function of observation date. An average K_s-band seeing of 1.38 arcsec and an average K_s-band magnitude zero point of 20.1 mag were found for the entire survey. These values agree with those found for the Norma wall survey (Riad 2010, Kraan-Korteweg et al. 2011). Fig. 4.1 shows that 95 per cent of the survey has seeing values below 2.0 arcsec. Fig. 4.2 shows that

---

[*] http://irsf-software.appspot.com/yas/nakajima/sirius.html

85 per cent of the survey lies within ± 0.2 mag of the mean magnitude zero point. While the deviations of magnitude zero point from the mean are not significant, Fig. 4.2 shows a clear trend that the sky is getting brighter with time. All fields with either seeing or zero point magnitude outside of these two ranges were inspected visually to check their image quality. Poor quality fields were re-observed under photometric conditions[†].

Fig. 4.3 shows one field that was re-observed, where the left panel shows the field observed under non-photometric conditions and the right panel shows that same field re-observed under photometric conditions. The image on the left hand side was taken under a partially cloudy sky which affects both the seeing and magnitude zero point. The K_s-band seeing for the left hand side image is 2.6 arcsec. The K_s-band zero point magnitude for the image on the left hand side was found to be 18.1 mag. In contrast, the right hand side image shows the field observed under photometric conditions. The K_s-band seeing and zero point magnitude for the right hand side image are 0.9 arcsec and 20.1 mag, respectively. The counterpart of the HIZOA galaxy, J1624-45A, in this field is an edge-on galaxy and is marked with the white ellipse in the bottom-left corner of each image. This example demonstrates how important photometric conditions are for this kind of survey. The extent of the galaxy on the left hand side is underestimated while the real size of the galaxy is apparent in the right hand image.

4.3 Final extended source catalogue

The procedures for source identification, star subtraction and photometry are described in detail by Williams et al. (2014). In this section we will therefore only present the final extended source catalogue. This catalogue contains photometry in the J, H, and K_s bands for 1044 galaxies. We divide the final catalogue into two separate catalogues, one for the HIZOA galaxies and the second for the bright 2MASX galaxies, full catalogues are available electronically. FITS files for the three bands are also available upon request. An example of the catalogue is given here for the brightest 100 galaxies in the

---

[†] These poor fields were removed and replaced with the photometric-quality ones for the final catalogue but we have made both FITS files available for comparison purposes

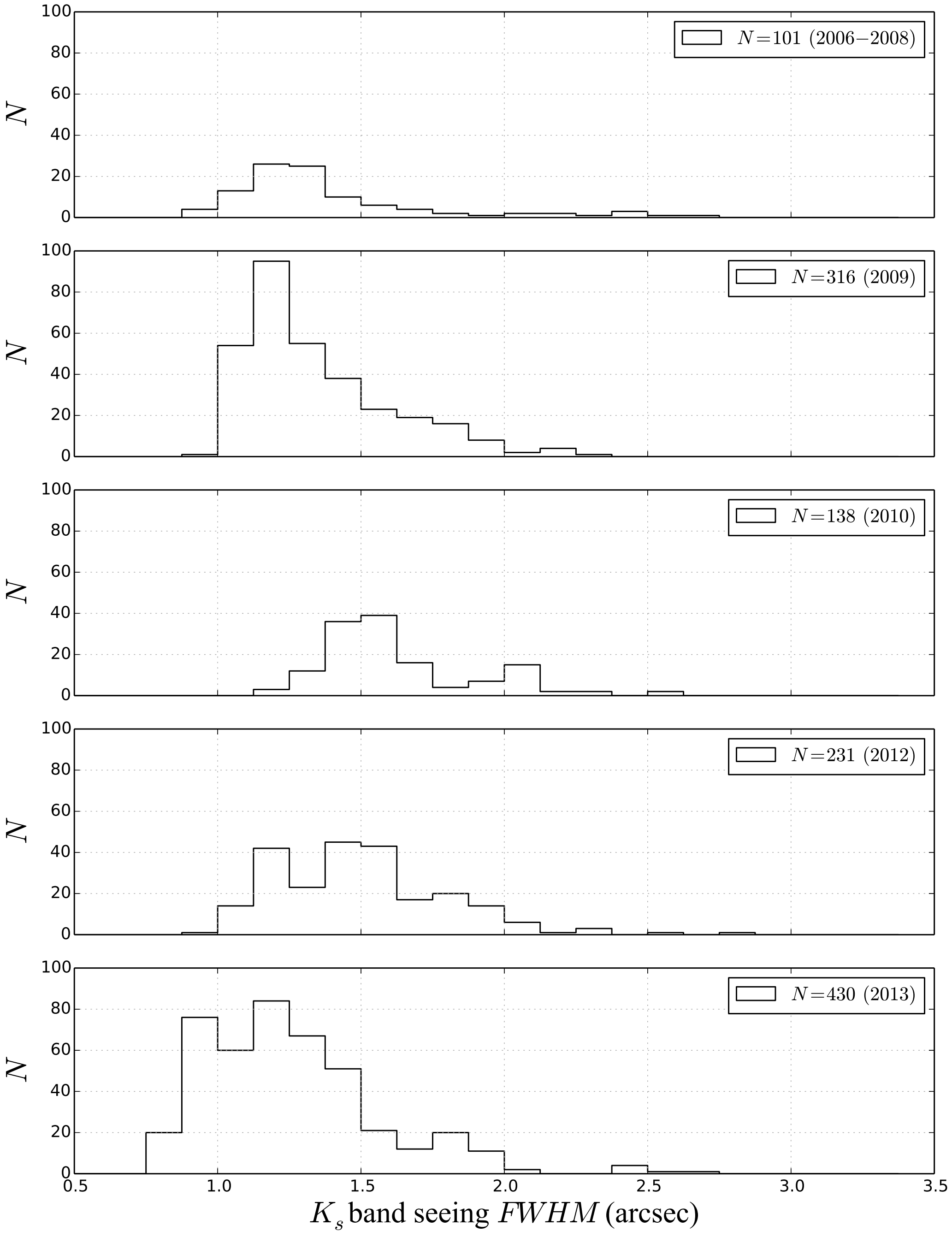

Figure 4.1: Distributions of the measured K_s-band seeing $FWHM$ from 2006 to 2013.

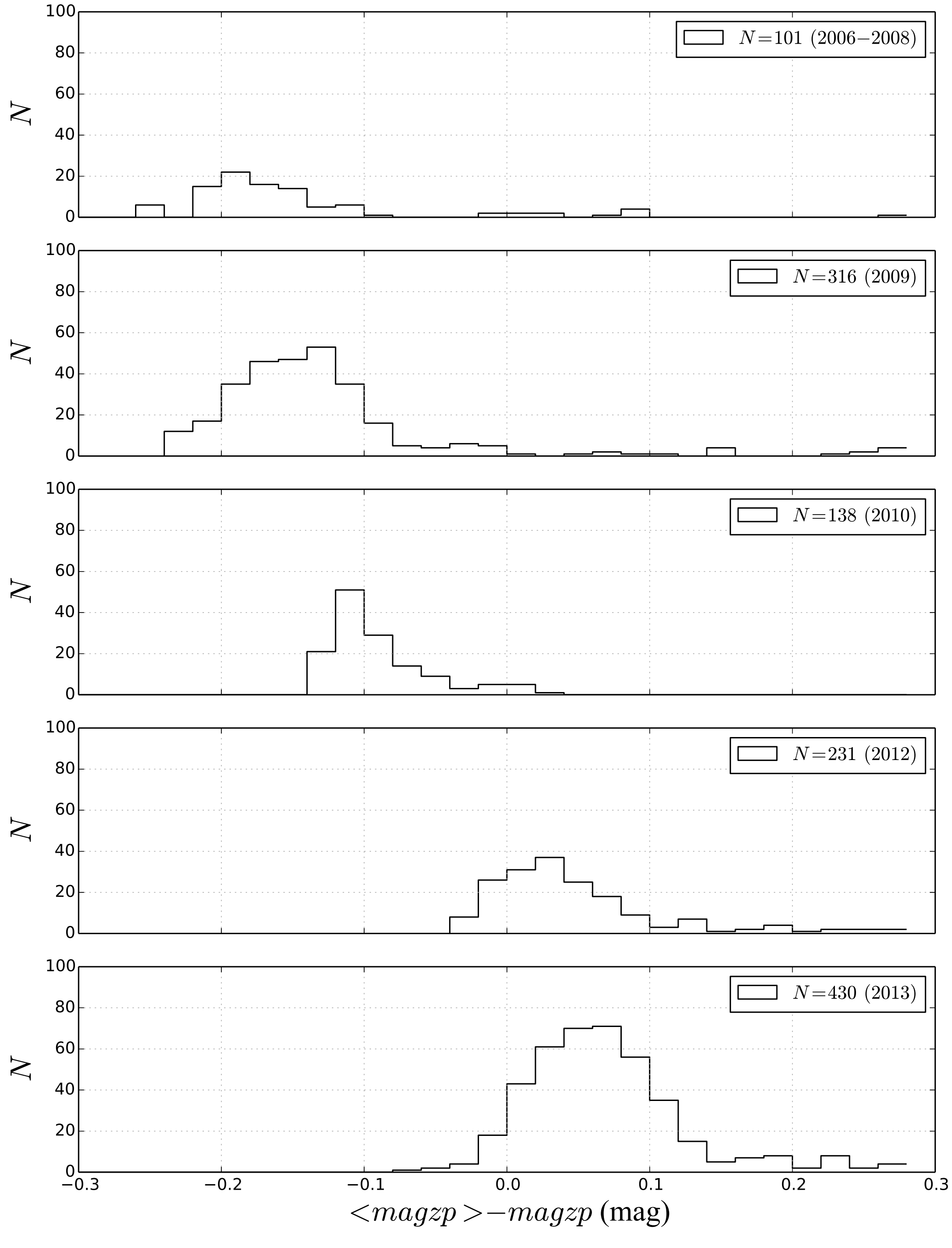

Figure 4.2: Distributions of the K_s-band photometric zero point magnitude from 2006 to 2013.

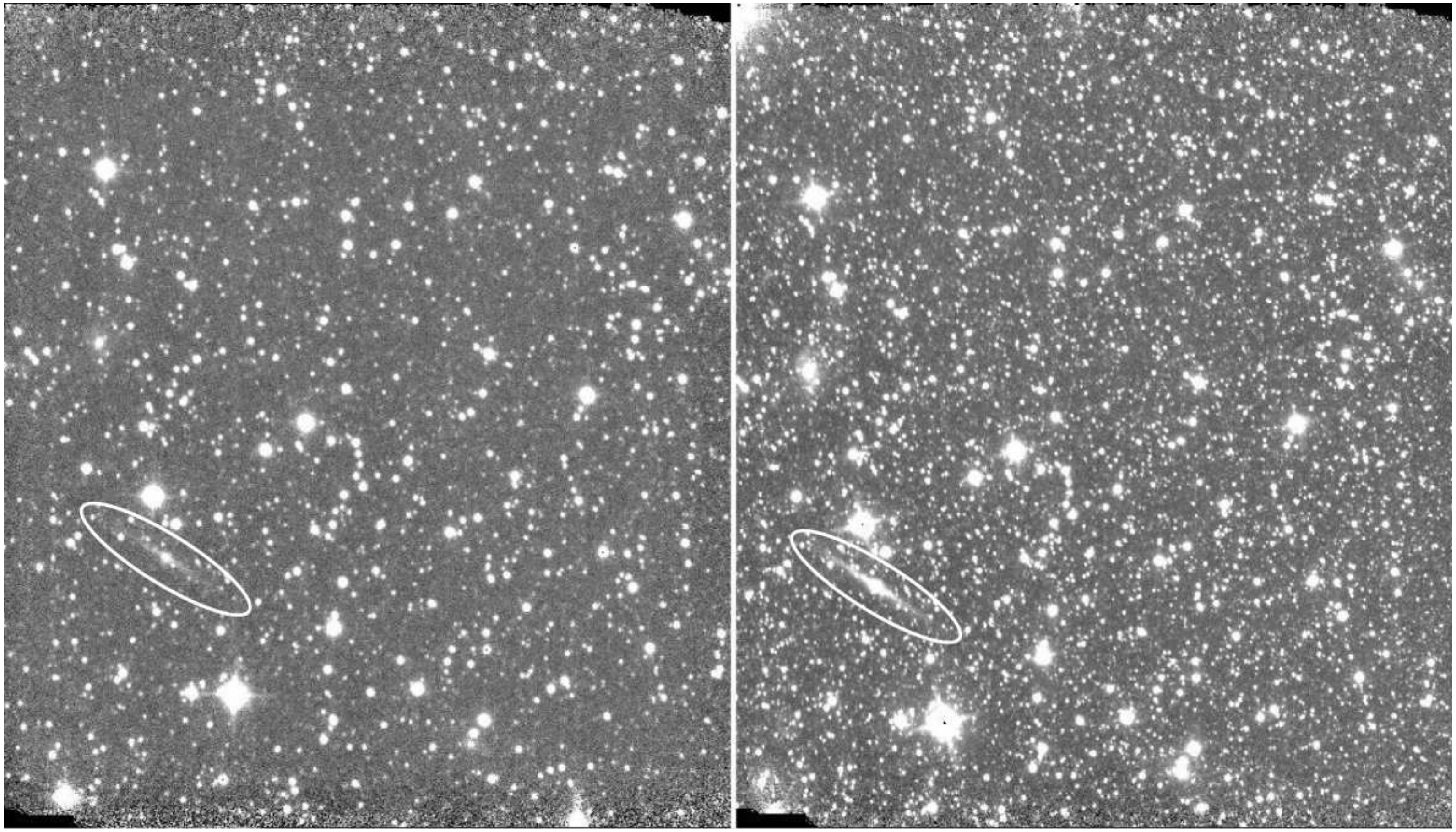

Figure 4.3: K_s-band photometric vs non-photometric images of the same field. Both images are 8.6 × 8.6 arcmin; the image on the left was observed under non-photometric conditions while the image on the right was re-observed under photometric conditions. The K_s-band seeing and zero point magnitude for the image on the left are 2.6 arcsec and 18.1 mag, respectively, while the K_s-band seeing and zero point magnitude for the image on the right are 0.9 arcsec and 20.1 mag, respectively. Note also the increase in resolved stars in the right image.

catalogue.

4.3.1 NIR Parametrization and catalogue

The main goal of this chapter is to provide accurate NIR photometric parameters for galaxies hidden behind the ZOA. These parameters will be used in the forthcoming NIR TF analysis. In this section we provide the required parameters. For consistency with Williams et al. (2014), we employ the same methods and naming for the whole survey as that described by Cutri et al. (2003). Table 4.2 and Fig. 4.4 present the photometry for and the postage stamp images of the brightest 100 galaxies in the catalogue, respectively, in order of isophotal K_{s20} fiducial elliptical aperture magnitude. The catalogue is presented in its entire form online. The NIR parameters listed in the catalogue are as follows:

Column (1) – unique ZOA ID formed from sexigesimal coordinates.

Column (2) – HIZOA ID as reported in the HIZOA survey publications (Donley et al. 2005; Staveley-Smith et al., 2015; Kraan-Korteweg et al., in prep.)[‡].

Column (3) – Survey name.

Columns (4 and 5) – Right Ascension (RA) and Declination (Dec.) in the J2000.0 epoch.

Columns (6 and 7) – Galactic coordinates [degree].

Column (8) – J-band ellipticity ($\epsilon = 1 - b/a$) measured as the mean value of the ellipticities of the ellipses fitted between the 1σ and 2σ, where σ is the sky rms.

Column (9) – Isophotal K_{s20} fiducial elliptical aperture semi-major axis [arcsec].

Columns (10–12) – J-, H-, and K_s-band K_{s20} fiducial elliptical aperture magnitudes and associated errors [mag].

Columns (13–15) – J-, H-, and K_s-band central surface brightness, measured as the magnitude of the mean flux within a radius $\leq$ 5 arcsec. [mag arcsec^{-2}].

Column (16) – E$(B-V)$, Galactic extinction as reported by Schlafly &

[‡] If the galaxy is not in the HIZOA catalogue, the 2MASX ID is provided instead.

Finkbeiner (2011).

Column (17) – SD, IRSF stellar density $\log(N_{K_s<14}/\mathrm{deg}^2)$ where $N_{K_s<14}$ is the number density of stars brighter than 14 mag in the K_s band.

Table 4.2: NIR coordinates, sizes, shapes and photometry of the brightest 100 galaxies in the catalogue in order of isophotal K_{s20} fiducial elliptical aperture magnitude. The full table is available online.

ZOA ID	HI Name	Survey	RA	DEC	l	b	ϵ_J	$r_{K_{s20fe}}$	$J_{K_{s20fe}}$	$H_{K_{s20fe}}$	$K_{sK_{s20fe}}$	μ_{cJ}	μ_{cH}	μ_{cKs}	$E(B-V)$	SD
			(J2000)		[deg]			[arcsec]	[mag]	[mag]	[mag]	[mag arcsec^{-2}]			[mag]	
(1)	(2)	(3)	(4)	(5)	(6)	(7)	(8)	(9)	(10)	(11)	(12)	(13)	(14)	(15)	(16)	(17)
ZOA141309.873-652020.76	J1413-65	HIZOA	213.291	−65.339	311.326	−3.808	0.44	87.05	7.50 ± 0.02	6.49 ± 0.02	6.09 ± 0.02	12.67	11.69	11.18	1.264	4.374
ZOA151434.147-525921.52	J1514-53	HIZOA	228.642	−52.989	323.594	4.043	0.77	136.09	8.86 ± 0.02	7.91 ± 0.02	7.42 ± 0.02	14.44	13.49	13.01	0.851	4.299
ZOA085728.473-391605.66	J0857-39	HIZOA	134.369	−39.268	261.500	4.100	0.10	45.77	9.18 ± 0.02	8.32 ± 0.02	7.95 ± 0.02	14.09	13.22	12.85	0.619	3.611
ZOA150928.962-523320.67	J1509-52	HIZOA	227.371	−52.556	323.155	4.810	0.79	98.73	9.24 ± 0.02	8.38 ± 0.02	7.97 ± 0.02	14.97	14.05	13.60	0.662	4.090
ZOA081706.065-272720.64	J0817-27	HIZOA	124.275	−27.456	246.973	4.481	0.41	59.84	9.17 ± 0.02	8.41 ± 0.02	8.11 ± 0.02	14.83	14.09	13.81	0.220	3.746
ZOA181427.987-022505.11	J1814-02	HIZOA	273.617	−2.418	26.526	7.099	0.47	47.82	10.04 ± 0.02	8.90 ± 0.02	8.50 ± 0.02	14.72	13.70	13.40	1.980	3.986
ZOA122238.290-583657.66	J1222-58	HIZOA	185.659	−58.616	299.180	4.046	0.69	60.30	9.71 ± 0.02	8.92 ± 0.02	8.60 ± 0.02	14.62	13.83	13.55	0.499	4.121
ZOA151413.880-464827.22	2MASX1514-464	2MASS	228.558	−46.808	326.808	9.338	0.53	114.03	10.75 ± 0.02	10.16 ± 0.02	8.60 ± 0.02	18.23	17.64	16.89	0.217	3.805
ZOA094916.505-475511.27	J0949-47A	HIZOA	147.319	−47.919	274.257	4.549	0.10	38.65	9.67 ± 0.02	8.97 ± 0.02	8.69 ± 0.02	14.37	13.62	13.36	0.301	3.797
ZOA145709.815-542331.46	J1457-54	HIZOA	224.291	−54.392	320.654	4.0957	0.51	53.80	10.04 ± 0.02	9.14 ± 0.02	8.69 ± 0.02	14.96	14.07	13.64	0.731	4.210
ZOA114606.371-562326.95	J1145-56	HIZOA	176.526	−56.391	293.937	5.336	0.27	54.68	9.99 ± 0.02	9.26 ± 0.02	8.82 ± 0.02	16.05	15.26	14.82	0.335	3.844
ZOA135138.534-583515.22	J1351-58	HIZOA	207.910	−58.588	310.724	3.370	0.52	47.27	10.23 ± 0.02	9.31 ± 0.02	8.87 ± 0.02	14.80	13.88	13.41	0.834	4.287
ZOA074752.048-184453.18	J0747-18	HIZOA	116.967	−18.748	236.009	3.374	0.82	84.90	10.06 ± 0.02	9.31 ± 0.02	8.91 ± 0.02	15.79	14.95	14.77	0.327	3.547
ZOA072210.950-055547.38	J0722-05	HIZOA	110.546	−5.930	221.732	4.088	0.78	48.64	9.99 ± 0.02	9.28 ± 0.02	8.99 ± 0.02	14.08	13.41	13.05	0.250	3.528
ZOA070103.346+015439.69	J0701+01	HIZOA	105.264	1.911	212.326	3.011	0.48	41.91	10.16 ± 0.02	9.37 ± 0.02	9.01 ± 0.02	15.09	14.34	13.93	0.520	3.563
ZOA143158.829-552758.82	J1431-55	HIZOA	217.995	−55.466	316.912	4.653	0.10	34.39	10.32 ± 0.02	9.46 ± 0.02	9.05 ± 0.02	15.65	14.75	14.31	0.731	4.091
ZOA080611.134-273140.86	J0806-27	HIZOA	121.546	−27.528	245.709	2.414	0.58	43.68	10.26 ± 0.02	9.51 ± 0.02	9.09 ± 0.02	14.84	14.10	13.67	0.420	3.731
ZOA074843.871-261445.62	J0748-26B	HIZOA	117.183	−26.246	242.586	−0.239	0.32	39.43	10.49 ± 0.02	9.64 ± 0.02	9.10 ± 0.02	15.53	14.56	14.04	0.482	3.723
ZOA163211.878-280530.82	J1632-28	HIZOA	248.050	−28.092	351.084	13.502	0.72	81.48	10.28 ± 0.02	9.45 ± 0.02	9.10 ± 0.02	15.64	14.80	14.46	0.525	3.536
ZOA141036.181-653457.76	J1410-65	HIZOA	212.651	−65.583	310.997	−3.958	0.52	46.18	10.35 ± 0.02	9.48 ± 0.02	9.14 ± 0.02	15.13	14.34	13.98	0.516	4.325
ZOA155524.078-581431.30	J1555-581	2MASS	238.850	−58.242	325.222	−3.570	0.37	65.37	11.32 ± 0.02	9.98 ± 0.02	9.16 ± 0.02	16.32	15.40	14.86	0.641	4.404
ZOA063554.386+110808.32	J0635+11	HIZOA	98.977	11.136	201.262	1.658	0.27	31.91	10.78 ± 0.02	9.63 ± 0.02	9.19 ± 0.02	15.67	14.70	14.29	1.310	3.518
ZOA083439.531-400855.61	J0834-40	HIZOA	128.665	−40.149	259.448	0.122	0.22	34.38	10.02 ± 0.02	9.52 ± 0.02	9.30 ± 0.02	15.30	14.61	14.51	1.823	3.838
ZOA132723.827-572922.23	J1327-57	HIZOA	201.849	−57.490	307.768	5.044	0.74	46.73	10.86 ± 0.02	9.82 ± 0.02	9.30 ± 0.02	15.93	14.75	14.09	0.697	3.980

Continued on Next Page...

Table 4.2 – Continued

ZOA ID	HI Name	Survey	RA	DEC	l	b	ϵ_J	$r_{K_{s20fe}}$	$J_{K_{s20fe}}$	$H_{K_{s20fe}}$	$K_{sK_{s20fe}}$	μ_{cJ}	μ_{cH}	μ_{cKs}	$E(B-V)$	SD
			(J2000)		[deg]			[arcsec]	[mag]	[mag]	[mag]	[mag arcsec^{-2}]			[mag]	
(1)	(2)	(3)	(4)	(5)	(6)	(7)	(8)	(9)	(10)	(11)	(12)	(13)	(14)	(15)	(16)	(17)
ZOA085838.795-423157.31	J0858-42	HIZOA	134.662	−42.533	264.125	2.141	0.45	43.00	11.95 ± 0.02	10.10 ± 0.02	9.35 ± 0.02	16.58	14.86	14.05	3.431	3.735
ZOA072456.870-093933.95	J0724-09	HIZOA	111.237	−9.659	225.354	2.942	0.29	32.86	10.48 ± 0.02	9.71 ± 0.02	9.41 ± 0.02	15.54	14.90	14.39	0.340	3.529
ZOA160349.297-605840.50	2MASX1603-605	2MASS	240.955	−60.978	324.235	−6.336	0.81	58.98	10.71 ± 0.02	9.85 ± 0.02	9.45 ± 0.02	15.62	15.02	14.67	0.275	4.036
ZOA094952.868-563235.55	J0949-56	HIZOA	147.470	−56.543	279.808	−2.054	0.24	45.57	11.43 ± 0.02	10.29 ± 0.02	9.58 ± 0.02	16.56	15.33	14.62	1.806	4.159
ZOA141710.092-553240.92	2MASX1417-553	2MASS	214.292	−55.545	314.915	5.320	0.85	58.28	11.27 ± 0.02	10.13 ± 0.02	9.58 ± 0.02	16.54	15.49	15.10	0.535	3.994
ZOA155422.988-612025.58	2MASX1554-612	2MASS	238.596	−61.340	323.130	−5.866	0.56	33.80	10.84 ± 0.02	10.11 ± 0.02	9.58 ± 0.02	15.45	15.09	14.44	0.348	4.042
ZOA141933.720-580850.19	J1419-58B	HIZOA	214.890	−58.147	314.363	2.755	0.59	52.89	11.00 ± 0.02	10.14 ± 0.02	9.59 ± 0.02	16.82	15.82	15.27	1.307	4.363
ZOA163140.118-280606.66	J1631-28	HIZOA	247.917	−28.101	350.997	13.584	0.27	35.29	10.83 ± 0.02	10.07 ± 0.02	9.59 ± 0.02	15.78	14.94	14.48	0.542	3.598
ZOA161710.946-581845.49	2MASX1617-581	2MASS	244.296	−58.313	327.304	−5.542	0.57	31.39	10.83 ± 0.02	10.05 ± 0.02	9.61 ± 0.02	15.11	14.33	13.80	0.260	4.203
ZOA101655.552-485252.32	2MASX1016-485	2MASS	154.231	−48.881	278.525	6.529	0.54	37.76	10.72 ± 0.02	9.74 ± 0.02	9.63 ± 0.02	16.01	15.29	14.91	0.183	3.659
ZOA160425.042-604415.93	2MASX1604-604	2MASS	241.104	−60.738	324.450	−6.205	0.77	40.77	10.73 ± 0.02	10.01 ± 0.02	9.65 ± 0.02	15.08	14.63	14.42	0.257	4.039
ZOA090033.110-392626.93	J0900-39	HIZOA	135.138	−39.441	262.020	4.438	0.39	37.83	10.79 ± 0.02	10.15 ± 0.02	9.67 ± 0.02	16.21	15.45	15.04	0.576	3.611
ZOA153603.059-594449.42	2MASXJ1536-5944	2MASS	234.013	−59.747	322.327	−3.226	0.46	41.50	10.92 ± 0.02	10.04 ± 0.02	9.67 ± 0.02	15.87	14.93	14.40	0.833	4.435
ZOA131033.767-580021.18	J1310-57	HIZOA	197.641	−58.006	305.472	4.772	0.27	27.20	10.81 ± 0.02	10.02 ± 0.02	9.68 ± 0.02	15.19	14.52	14.22	0.480	4.080
ZOA161319.695-562349.17	J1613-56	HIZOA	243.332	−56.397	328.261	−3.802	0.35	40.49	10.93 ± 0.02	10.69 ± 0.02	9.68 ± 0.02	16.15	15.39	14.87	0.464	4.425
ZOA074252.007-315959.79	J0742-31	HIZOA	115.717	−32.000	246.932	−4.2257	0.52	26.61	11.15 ± 0.02	10.38 ± 0.02	9.71 ± 0.02	15.39	14.72	14.15	0.714	3.757
ZOA101212.032-623159.40	J1012-62	HIZOA	153.050	−62.533	285.686	−5.121	0.62	39.84	10.84 ± 0.02	10.08 ± 0.02	9.71 ± 0.02	15.80	15.03	14.51	0.249	4.036
ZOA162101.624-360831.49	J1621-36	HIZOA	245.257	−36.142	343.413	9.765	0.55	38.44	10.84 ± 0.02	10.05 ± 0.02	9.71 ± 0.02	15.25	14.44	14.09	0.611	3.789
ZOA070056.215-114734.32	J0700-11	HIZOA	105.234	−11.793	224.511	−3.273	0.70	42.70	11.39 ± 0.02	10.29 ± 0.02	9.72 ± 0.02	16.21	15.12	14.61	0.680	3.595
ZOA072457.474-271516.87	J0724-27	HIZOA	111.240	−27.255	240.882	−5.366	0.36	41.90	11.78 ± 0.02	11.03 ± 0.02	9.72 ± 0.02	16.64	15.89	15.49	0.370	3.668
ZOA181530.143-025348.41	J1815-02	HIZOA	273.876	−2.897	26.220	6.647	0.10	32.73	11.41 ± 0.02	10.26 ± 0.02	9.72 ± 0.02	16.32	15.29	14.62	2.230	3.973
ZOA114948.692-640006.93	J1149-64	HIZOA	177.453	−64.002	296.241	−1.934	0.57	42.66	11.73 ± 0.02	10.42 ± 0.02	9.73 ± 0.02	17.05	15.76	15.05	2.098	4.382
ZOA141710.099-553238.77	J1416-55B	HIZOA	214.292	−55.544	314.916	5.320	0.86	68.61	11.23 ± 0.02	10.10 ± 0.02	9.73 ± 0.02	16.58	15.47	14.96	0.533	3.982
ZOA074141.201-223112.25	J0741-22	HIZOA	115.422	−22.520	238.558	0.239	0.80	48.26	11.31 ± 0.02	10.24 ± 0.02	9.74 ± 0.02	16.54	15.35	14.64	0.568	3.737
ZOA161710.749-581844.59	J1617-58	HIZOA	244.295	−58.313	327.304	−5.542	0.53	33.09	10.82 ± 0.02	10.04 ± 0.02	9.75 ± 0.02	15.19	14.39	14.00	0.258	4.159

Continued on Next Page...

Table 4.2 – Continued

ZOA ID	HI Name	Survey	RA	DEC	l	b	ϵ_J	$r_{K_{s20fe}}$	$J_{K_{s20fe}}$	$H_{K_{s20fe}}$	$K_{sK_{s20fe}}$	μ_{cJ}	μ_{cH}	μ_{cKs}	$E(B-V)$	SD
			(J2000)		[deg]			[arcsec]	[mag]	[mag]	[mag]	[mag arcsec^{-2}]			[mag]	
(1)	(2)	(3)	(4)	(5)	(6)	(7)	(8)	(9)	(10)	(11)	(12)	(13)	(14)	(15)	(16)	(17)
ZOA101220.012-471741.58	2MASX1012-471	2MASS	153.083	−47.295	276.983	7.402	0.81	68.92	11.15 ± 0.02	10.21 ± 0.02	9.76 ± 0.02	16.72	15.89	15.26	0.164	3.478
ZOA073008.083-220105.84	J0730-22	HIZOA	112.534	−22.018	236.817	−1.851	0.77	104.61	11.51 ± 0.02	10.04 ± 0.02	9.79 ± 0.02	17.94	16.76	16.38	1.557	3.695
ZOA075220.625-250840.47	J0752-25A	HIZOA	118.086	−25.145	242.052	1.022	0.56	33.38	10.92 ± 0.02	10.17 ± 0.02	9.79 ± 0.02	15.47	14.70	14.35	0.327	3.678
ZOA065010.633-111513.52	J0650-11	HIZOA	102.544	−11.254	222.835	−5.381	0.18	26.46	11.27 ± 0.02	10.36 ± 0.02	9.83 ± 0.02	15.75	14.90	14.42	0.960	3.493
ZOA182226.663-354035.70	J1822-35	HIZOA	275.611	−35.677	357.859	−10.062	0.65	37.90	10.98 ± 0.02	10.14 ± 0.02	9.84 ± 0.02	16.10	15.22	14.79	0.120	4.113
ZOA164634.204-390308.21	J1646-39	HIZOA	251.642	−39.052	344.676	4.067	0.24	39.69	11.94 ± 0.02	10.98 ± 0.02	9.85 ± 0.02	16.67	15.79	15.34	0.990	4.446
ZOA141604.868-651502.53	J1416-65	HIZOA	214.020	−65.250	311.644	−3.821	0.48	36.60	11.23 ± 0.02	10.32 ± 0.02	9.89 ± 0.02	15.77	14.86	14.45	0.662	4.314
ZOA100318.769-645803.19	2MASX1003-645	2MASS	150.828	−64.968	286.322	−7.668	0.58	29.86	10.93 ± 0.02	9.98 ± 0.02	9.90 ± 0.02	15.68	14.93	14.73	0.197	3.759
ZOA105345.693-625013.17	J1053-62	HIZOA	163.440	−62.837	289.956	−2.968	0.67	65.48	11.60 ± 0.02	10.68 ± 0.02	9.90 ± 0.02	17.78	16.80	16.23	0.714	4.234
ZOA080708.583-280309.50	J0807-28	HIZOA	121.786	−28.053	246.266	2.310	0.61	42.80	11.01 ± 0.02	10.29 ± 0.02	9.92 ± 0.02	16.69	16.02	15.56	0.460	3.676
ZOA133732.784-585414.06	J1337-58B	HIZOA	204.387	−58.904	308.867	3.436	0.28	33.07	11.33 ± 0.02	10.31 ± 0.02	9.92 ± 0.02	16.20	15.11	14.48	0.937	4.303
ZOA143927.759-552503.43	J1439-55	HIZOA	219.866	−55.418	317.910	4.281	0.22	30.55	11.17 ± 0.02	10.41 ± 0.02	9.97 ± 0.02	16.75	15.92	15.53	0.550	4.110
ZOA105859.839-502155.66	2MASX1058-501	2MASS	164.749	−50.365	285.236	8.603	0.13	24.61	11.03 ± 0.02	10.11 ± 0.02	9.98 ± 0.02	15.41	14.64	14.33	0.246	3.651
ZOA074901.358-261442.69	J0748-26A	HIZOA	117.256	−26.245	242.618	−0.182	0.27	26.65	11.49 ± 0.02	10.33 ± 0.02	9.99 ± 0.02	15.56	14.61	14.20	0.619	3.837
ZOA113728.729-644822.59	J1137-644	2MASS	174.370	−64.806	295.162	−3.056	0.21	26.51	11.96 ± 0.02	10.63 ± 0.02	10.00 ± 0.02	16.35	15.00	14.46	1.363	4.252
ZOA082837.437-371316.76	J0828-37	HIZOA	127.156	−37.221	256.391	0.904	0.66	36.26	11.42 ± 0.02	10.46 ± 0.02	10.03 ± 0.02	16.18	15.34	14.99	0.920	3.855
ZOA134456.207-654051.40	J1344-65	HIZOA	206.234	−65.681	308.408	−3.380	0.54	34.10	11.38 ± 0.02	10.47 ± 0.02	10.03 ± 0.02	16.09	15.23	14.68	0.870	4.326
ZOA132159.534-543645.62	2MASX1321-543	2MASS	200.498	−54.613	307.390	7.994	0.73	41.15	11.28 ± 0.02	10.45 ± 0.02	10.04 ± 0.02	16.63	15.84	15.52	0.349	3.786
ZOA164421.521-552937.33	J1644-55	HIZOA	251.090	−55.494	331.917	−6.333	0.83	41.24	11.41 ± 0.02	10.41 ± 0.02	10.04 ± 0.02	16.52	15.54	15.03	0.292	4.129
ZOA140835.888-532111.29	2MASX1408-532	2MASS	212.150	−53.353	314.411	7.790	0.33	33.68	11.00 ± 0.02	10.35 ± 0.02	10.05 ± 0.02	15.50	15.31	15.22	0.424	3.829
ZOA105842.989-501930.65	2MASX1058-501	2MASS	164.679	−50.325	285.177	8.620	0.82	45.60	11.40 ± 0.02	10.53 ± 0.02	10.08 ± 0.02	16.09	15.27	14.73	0.246	3.651
ZOA064400.636+122407.13	J0644+12	HIZOA	101.003	12.402	201.040	4.001	0.65	38.29	11.28 ± 0.02	10.55 ± 0.02	10.09 ± 0.02	15.70	15.07	14.46	0.440	3.409
ZOA182423.339-341054.15	J1824-34	HIZOA	276.097	−34.181	359.399	−9.758	0.36	25.92	11.08 ± 0.02	10.38 ± 0.02	10.09 ± 0.02	15.80	15.05	14.72	0.112	4.079
ZOA154526.828-605931.93	J1545-61	HIZOA	236.362	−60.992	322.508	−4.918	0.49	27.22	11.49 ± 0.02	10.58 ± 0.02	10.10 ± 0.02	16.00	14.97	14.41	0.611	4.140
ZOA123157.581-595058.07	J1231-595	2MASS	187.990	−59.850	300.485	2.930	0.28	28.59	11.50 ± 0.02	10.53 ± 0.02	10.11 ± 0.02	16.27	15.32	15.10	0.803	4.215

Continued on Next Page. . .

Table 4.2 – Continued

ZOA ID	HI Name	Survey	RA	DEC	l	b	ϵ_J	$r_{K_{s20fe}}$	$J_{K_{s20fe}}$	$H_{K_{s20fe}}$	$K_{sK_{s20fe}}$	μ_{cJ}	μ_{cH}	μ_{cKs}	$E(B-V)$	SD
			(J2000)		[deg]			[arcsec]	[mag]	[mag]	[mag]	[mag arcsec^{-2}]			[mag]	
(1)	(2)	(3)	(4)	(5)	(6)	(7)	(8)	(9)	(10)	(11)	(12)	(13)	(14)	(15)	(16)	(17)
ZOA151113.653-535743.36	J1511-535	2MASS	227.807	−53.962	322.664	3.466	0.12	21.61	11.39 ± 0.02	10.52 ± 0.02	10.11 ± 0.02	15.70	15.03	14.87	0.858	4.316
ZOA085809.386-454812.51	J0858-45A	HIZOA	134.539	−45.803	266.544	−0.062	0.30	28.25	12.14 ± 0.02	10.95 ± 0.02	10.12 ± 0.02	17.26	15.87	15.08	2.356	3.890
ZOA085828.676-451630.99	J0858-45B	HIZOA	134.619	−45.275	266.181	0.325	0.29	35.29	12.29 ± 0.02	10.94 ± 0.02	10.12 ± 0.02	17.97	16.54	15.77	3.148	3.819
ZOA133724.550-585221.57	J1337-58B	HIZOA	204.35229	−58.873	308.855	3.469	0.68	34.33	11.48 ± 0.02	10.51 ± 0.02	10.12 ± 0.02	15.54	14.67	14.28	0.937	4.303
ZOA154710.889-590408.56	J1547-59	HIZOA	236.795	−59.069	323.868	−3.538	0.39	47.97	11.32 ± 0.02	10.70 ± 0.02	10.13 ± 0.02	16.82	15.96	15.48	0.550	4.345
ZOA163617.005-421325.00	J1636-421	2MASS	249.071	−42.224	340.998	3.445	0.39	28.61	11.15 ± 0.02	10.54 ± 0.02	10.13 ± 0.02	16.10	15.30	14.72	1.669	4.401
ZOA165408.098-353438.65	J1653-35	HIZOA	253.534	−35.577	348.325	5.120	0.13	18.68	11.47 ± 0.02	10.68 ± 0.02	10.17 ± 0.02	15.53	15.12	14.29	0.930	4.395
ZOA140627.300-575142.26	J1406-57	HIZOA	211.614	−57.862	312.799	3.566	0.27	32.83	11.57 ± 0.02	10.62 ± 0.02	10.18 ± 0.02	16.46	15.50	15.13	0.628	4.171
ZOA160441.177-413947.62	J1604-41	HIZOA	241.172	−41.663	337.221	7.994	0.35	28.11	11.25 ± 0.02	10.55 ± 0.02	10.18 ± 0.02	16.32	15.53	15.17	0.559	3.887
ZOA090240.287-413502.67	J0902-413	2MASS	135.668	−41.584	263.902	3.328	0.52	28.06	11.53 ± 0.02	10.61 ± 0.02	10.19 ± 0.02	16.09	15.18	14.80	1.000	3.659
ZOA155335.142-614059.08	2MASX1553-614	2MASS	238.396	−61.683	322.836	−6.068	0.74	38.79	11.32 ± 0.02	10.51 ± 0.02	10.20 ± 0.02	16.10	15.50	15.47	0.287	4.020
ZOA182700.997-203159.00	J1826-20	HIZOA	276.754	−20.533	11.924	−4.088	0.70	41.25	11.59 ± 0.02	10.62 ± 0.02	10.20 ± 0.02	16.62	15.62	15.17	0.714	4.688
ZOA140621.248-602544.76	J1406-602	2MASS	211.589	−60.429	312.051	1.109	0.42	22.18	12.47 ± 0.02	10.97 ± 0.02	10.21 ± 0.02	16.55	15.26	14.53	2.962	4.638
ZOA134423.990-522211.32	2MASX1344-522	2MASS	206.100	−52.370	311.087	9.661	0.75	40.16	11.57 ± 0.02	10.64 ± 0.02	10.22 ± 0.02	16.65	15.79	15.43	0.387	3.632
ZOA170643.848-482357.97	2MASXJ1706-4823	2MASS	256.683	−48.399	339.642	−4.607	0.71	28.00	11.68 ± 0.02	10.79 ± 0.02	10.24 ± 0.02	16.10	15.27	14.60	0.747	4.363
ZOA080953.826-414136.58	J0809-41	HIZOA	122.474	−41.694	258.049	−4.600	0.84	66.41	12.03 ± 0.02	10.82 ± 0.02	10.25 ± 0.02	17.66	16.41	15.72	1.049	3.750
ZOA151548.734-600409.37	J1515-60B	HIZOA	228.953	−60.069	320.037	−2.083	0.17	32.38	12.09 ± 0.02	10.84 ± 0.02	10.25 ± 0.02	17.56	16.25	15.61	3.113	4.611
ZOA165805.966-211622.32	J1658-21A	HIZOA	254.525	−21.273	0.331	13.190	0.12	28.09	11.30 ± 0.02	10.52 ± 0.02	10.27 ± 0.02	16.21	15.52	15.39	0.300	3.667
ZOA105838.725-645044.49	J1058-645	HIZOA	164.661	−64.846	291.308	−4.551	0.16	22.02	11.53 ± 0.02	10.65 ± 0.02	10.28 ± 0.02	15.82	14.93	14.84	0.533	4.122
ZOA160449.497-414301.20	J1604-41	HIZOA	241.206	−41.717	337.204	7.937	0.44	36.21	11.42 ± 0.02	10.71 ± 0.02	10.29 ± 0.02	16.40	15.62	15.24	0.559	3.887
ZOA183155.989-314742.59	J1831-31	HIZOA	277.983	−31.795	2.280	−10.134	0.35	32.63	11.24 ± 0.02	10.57 ± 0.02	10.30 ± 0.02	16.16	15.49	15.21	0.146	4.054
ZOA063556.737+143557.75	J0635+14B	HIZOA	98.986	14.599	198.185	3.254	0.20	21.72	11.49 ± 0.02	10.66 ± 0.02	10.31 ± 0.02	15.74	14.92	14.65	0.570	3.529
ZOA120920.790-622912.31	J1209-62	HIZOA	182.337	−62.487	298.092	−0.011	0.36	22.97	13.08 ± 0.02	11.21 ± 0.02	10.31 ± 0.02	17.35	15.59	14.70	3.294	4.553
ZOA141232.785-563433.93	J1412-56A	HIZOA	213.137	−56.576	313.972	4.547	0.46	42.52	11.43 ± 0.02	10.62 ± 0.02	10.32 ± 0.02	17.21	16.41	16.07	0.559	4.149
ZOA072653.624-073252.01	J0726-07	HIZOA	111.723	−7.548	223.715	4.362	0.21	27.41	11.00 ± 0.02	10.64 ± 0.02	10.35 ± 0.02	16.59	16.08	15.80	0.240	3.492
ZOA100655.897-450248.59	2MASX1006-450	2MASS	151.733	−45.047	274.892	8.682	0.65	33.97	11.43 ± 0.02	10.72 ± 0.02	10.35 ± 0.02	16.53	15.93	15.52	0.132	3.504

Table 4.3: Summary of the characteristic properties of the catalogue.

Parameter	Mean	Max.	Min.
ϵ_J	0.42	0.90	0.10
$r_{K_{s20fe}}$ [arcsec]	15.57	136.08	0.51
$J_{K_{s20fe}}$ [mag]	14.28	22.08	7.50
$H_{K_{s20fe}}$ [mag]	13.39	22.65	6.49
$K_{sK_{s20fe}}$ [mag]	13.02	23.02	6.09
$E(B-V)$ [mag]	0.92	12.76	0.09
SD	3.95	5.32	3.28

4.3.2 Data presentation

Table 4.3 and Fig. 4.5 summarize the characteristic properties of the NIR catalogue. In Table 4.3 we list the mean, maximum and minimum for a number of parameters. These parameters are as follows:

- J-band ellipticity (ϵ_J)
- K_{s20} fiducial elliptical aperture semi-major axis ($r_{K_{s20fe}}$)
- J-, H-, and K_s-band K_{s20} fiducial elliptical aperture magnitudes ($J_{K_{s20fe}}$, $H_{K_{s20fe}}$, and $K_{sK_{s20fe}}$)
- Galactic extinction as reported by Schlafly & Finkbeiner (2011) ($E(B-V)$)
- IRSF stellar density of stars brighter than 14 mag in the K_s band (SD)

Fig. 4.5 shows histograms of all parameters except $E(B-V)$ and stellar density which are discussed in detail in the next section as part of the completeness.

The top panels, A, B, and C, of Fig. 4.5 show the distributions in Galactic longitude, shape and size. Panel A illustrates the success of this work in unveiling galaxies hidden behind the MW especially in over-dense regions like Puppis and the GA around $240° < l < 270°$ and $300° < l < 330°$ respectively. The drop in the number of sources toward the Galactic bulge is due to the LV (Kraan-Korteweg et al. 2008, Staveley-Smith et al. 2016). Panel B shows a fairly flat distribution of galaxy ellipticities, which is consistent with the expectation of a random sample of disk galaxies. However, for our final TF

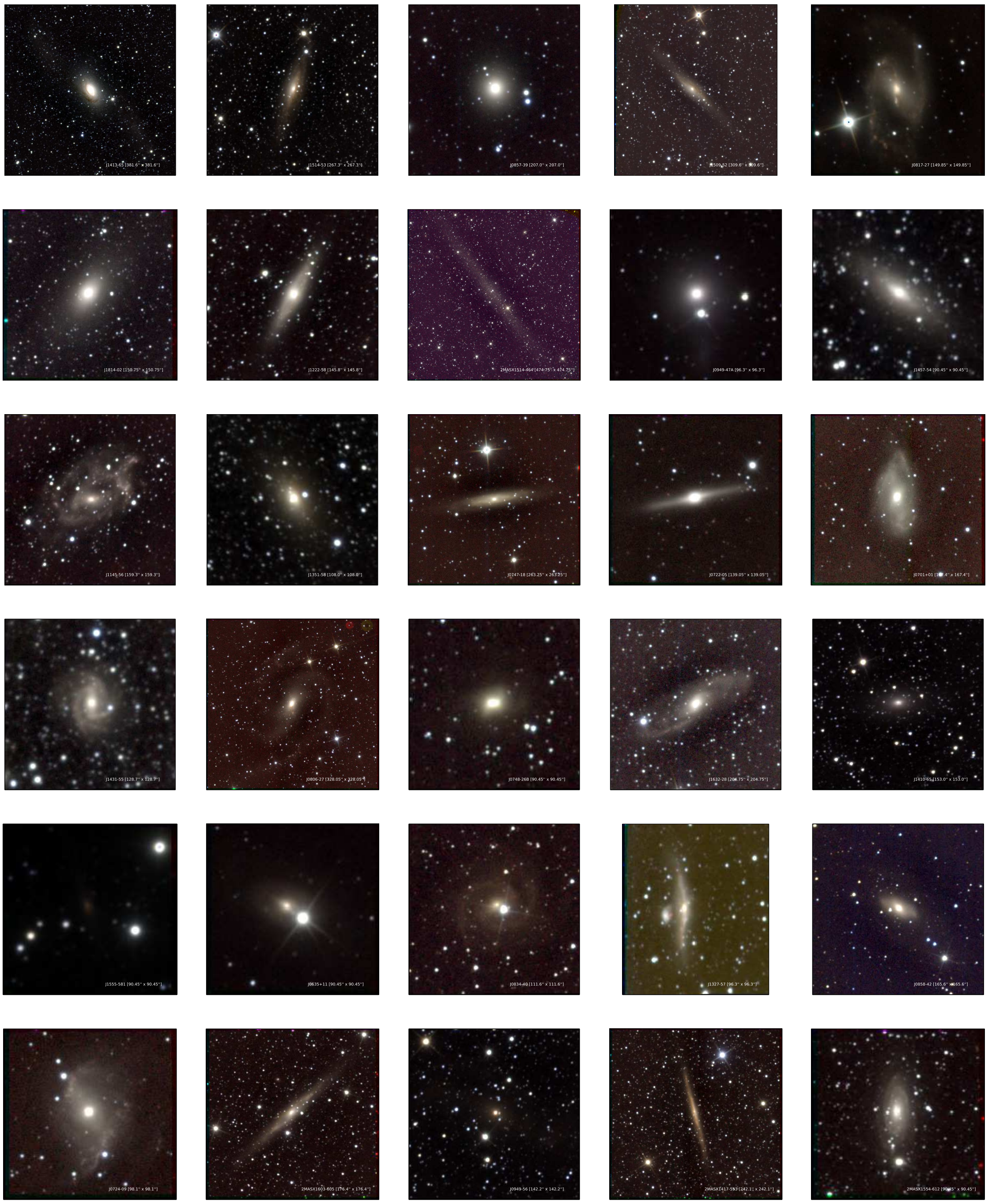

Figure 4.4: Postage stamp images of the brightest 100 galaxies in the catalogue in order of isophotal K_{s20} fiducial elliptical aperture magnitude. The colour composites are generated in the standard fashion: blue – J band, green – H band, and red – K_s band.

Figure 4.4: Continued

Figure 4.4: Continued

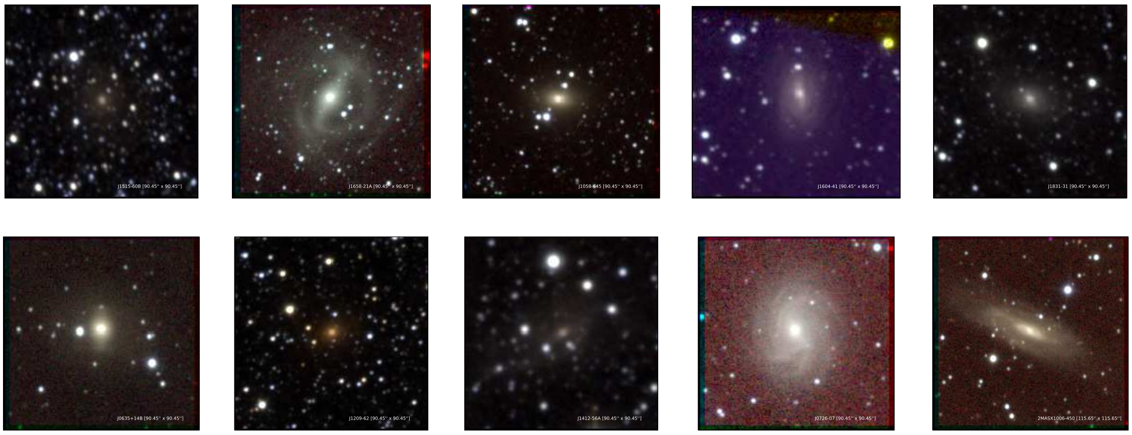

Figure 4.4: Continued

sample we use only edge-on galaxies after applying the axial ratio correction from Said et al. (2015). In panel C we plot a histogram of the distribution of the K_{s20} fiducial elliptical aperture semi-major axis. Panel C shows that only three galaxies in our sample have $r_{K_{s20fe}}$ larger than 100 arcsec and 21 galaxies are larger than 50 arcsec. The largest three galaxies are J1514-53, 2MASX1514-464, and J0730-22 which have $r_{K_{s20fe}}$ of 136, 114 and 104 arcsec, respectively.

In panels D, E, and F of Fig. 4.5, we show histograms of the J-, H-, and K_s-band K_{s20} fiducial elliptical aperture magnitudes. Based on the deep NIR survey of the Norma Wall (Riad 2010, Kraan-Korteweg et al. 2011), which used the same instrument with the same setup, we expect similar completeness limits of $J^\circ = 15.6$, $H^\circ = 15.3$, and $K_s^\circ = 14.8$ mag in the J, H, and K_s bands, respectively. However, these limits are only valid for $A_{K_s} < 1.0$ mag and $\log(N_{(K_s<14)}/deg^2) < 4.71$. Compared to other NIR surveys, this IRSF survey is 1 mag deeper than 2MASS in the J band and 2 mag deeper in the K_s band. Moreover, it is only 1 mag shallower than the UKIDSS Galactic Plane Survey (GPS; Lucas et al. 2008) and VISTA Variables in the Via Lactea (VVV; Amôres et al. 2012) in the K_s band. In Section 4.5.3 we present a full comparison with UKIDSS GPS galaxies. The three panels (D, E, and F) of Fig. 4.5 show that the detection rate drops rapidly for galaxies fainter than 16 mag. However, this survey is not magnitude limited in any sense. Panel F shows that our survey has 63 galaxies brighter than 10 mag.

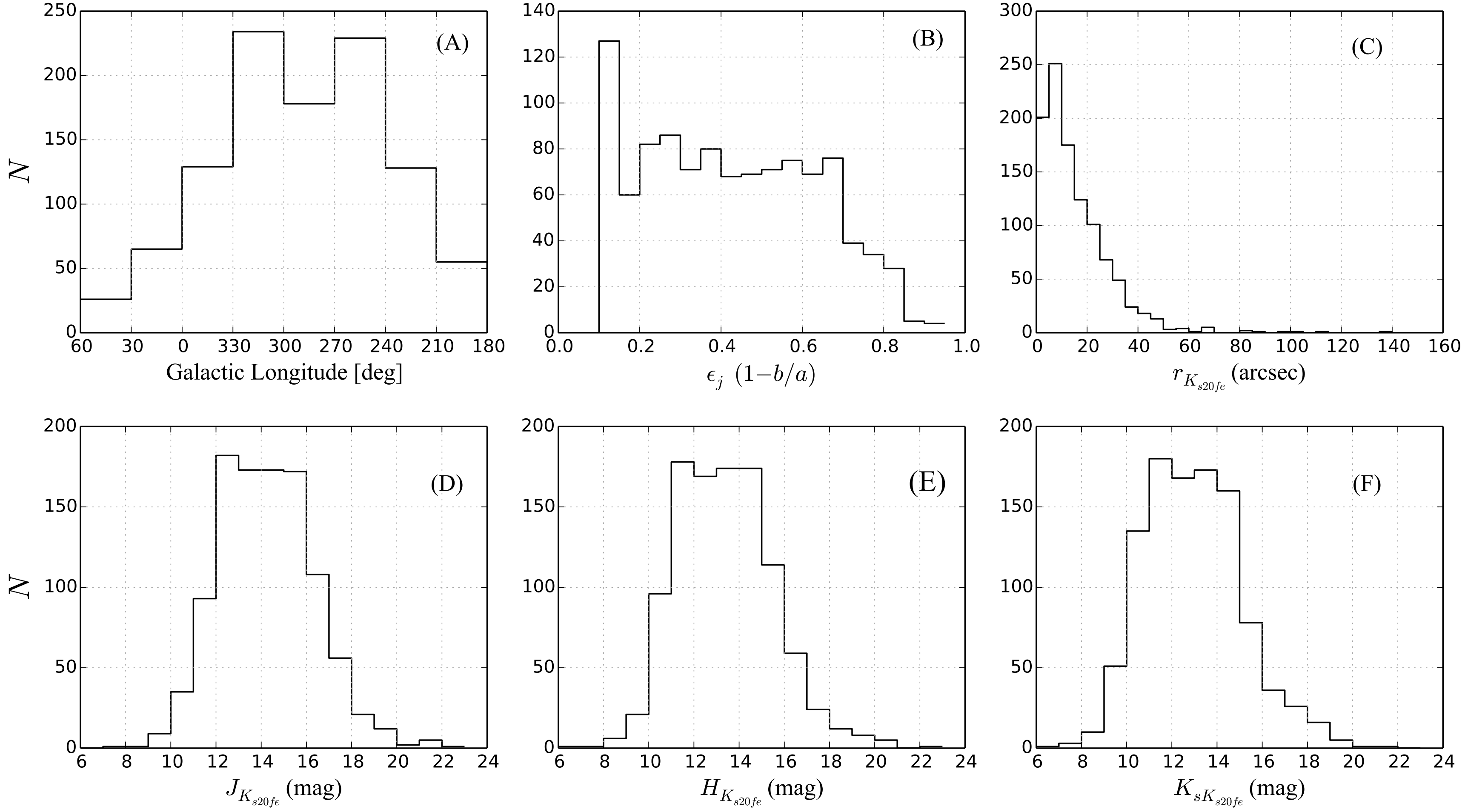

Figure 4.5: Summary of the characteristic photometric properties of the catalogue. The top panels A, B, and C show the distribution as a function of Galactic longitude, the shape, represented by (ϵ_J) the J-band ellipticity, and size, represented by ($r_{K_{s20fe}}$) K_{s20} fiducial elliptical aperture semi-major axis, of 1044 galaxies in the catalogue. The bottom panels D, E, and F show the distributions of the K_{s20} fiducial elliptical aperture magnitudes in the J, H, and K_s bands, respectively.

4.4 Completeness

In this section we discuss the completeness as a function of dust extinction, stellar density and H I mass. We divided the catalogue into three sub-samples according to their logarithm H I mass reported by Staveley-Smith et al. (2016). The first column in Fig. 4.6 shows galaxies with $\log M_{HI}[M_\odot] \geq 9.5$. The second column presents galaxies within the range of $8.5 \leq \log M_{HI}[M_\odot] < 9.5$. The third column shows galaxies with $\log M_{HI}[M_\odot] < 8.5$.

The top panels in Fig. 4.6 show the completeness as a function of the IRSF stellar density of stars brighter than 14 mag in the K_s band for the three sub-samples. The first two columns in the top panel show that detection rate is 100 per cent for massive galaxies ($\log M_{HI}[M_\odot] > 8.5$) in regions with stellar density of $\log(N_{K_s<14}/\mathrm{deg}^2) \leq 4$. This detection rate drops to 50 per cent for regions with $\log(N_{K_s<14}/\mathrm{deg}^2) > 4$. In contrast, the third column in the top panel shows that the detection rate of the least massive galaxies ($\log M_{HI}[M_\odot] < 8.5$) is 75 per cent complete in regions of $\log(N_{K_s<14}/\mathrm{deg}^2) \leq 4$ and only 30 per cent in regions with stellar density of $\log(N_{K_s<14}/\mathrm{deg}^2) > 4$. Most of these least massive galaxies are dwarfs and will be excluded from the TF analysis because they have the highest scatter in the TF relation.

Similar conclusions can be drawn from the bottom panels of Fig. 4.6 which show the completeness as a function of Galactic reddening along the line of sight (Schlafly & Finkbeiner 2011). The first two columns in the bottom panel show that the detection rate of the massive galaxies is nearly 90 per cent in regions of $E(B-V) \leq 1$ mag ($A_V \leq 3.1$ mag). Furthermore, we can still detect massive galaxies up to $E(B-V) = 7$ mag ($A_V = 21.7$ mag). On the contrary, the third column in the bottom panel shows that the detection of the least massive galaxies is not complete anywhere, not even in regions with $E(B-V) \leq 1$ mag ($A_V \leq 3.1$ mag).

We note that the measured photometric parameters (e.g, magnitude, size and shape) will be also affected by these trends and should be corrected before use in the TF analysis. Riad et al. (2010) discuss the effect of dust extinction on magnitude and size of galaxies and provide a correction model for extinction values up to $A_{K_s} = 3$ mag ($A_V = 25$ mag). While Said et al. (2015) simulate the effect of dust extinction on the shape (ellipticity) of galaxies and

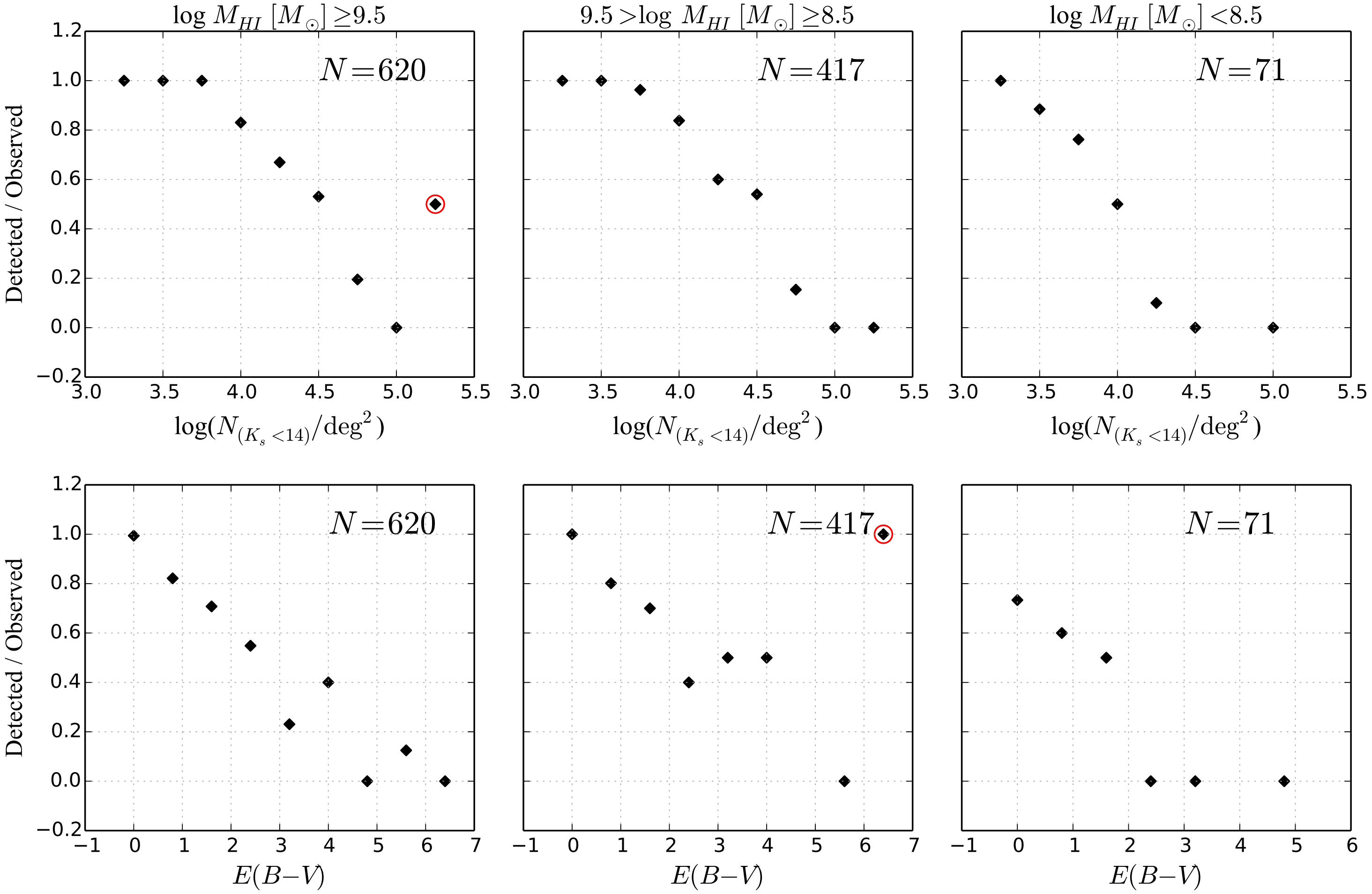

Figure 4.6: The completeness as a function of stellar density and dust extinction for different H I mass ranges. The three columns present different HI mass ranges. The top panels show the completeness as a function of the logarithm of the stellar density of stars brighter than 14 mag in the K_s band. The bottom panels show the completeness as a function of Galactic reddening along the line of sight. The outliers marked with the red circles are due to low numbers of galaxies in these two bins.

also provide a correction model to reproduce the intrinsic axial ratio from the observed value up to extinction levels of $A_J = 3$ mag ($A_V = 11$ mag). These corrections will be used to correct the magnitudes, sizes and shapes of galaxies before use in the TF analysis.

4.5 Counterparts and Comparisons

In this section we discuss the counterparts of our survey. We present the confirmed HIZOA counterparts then check for counterparts in the 2MASX (Jarrett et al. 2000) and UKIDSS GPS (Lucas et al. 2008) surveys. We also present a comparison of our photometry with both the shallower 2MASX and the deeper UKIDSS GPS surveys.

4.5.1 HIZOA counterparts

The pixel size of the final HIZOA cubes of 4 arcmin in RA and DEC makes the IRSF perfect for the follow-up observations given its 8.6×8.6 arcmin^2 field of view (after dithering). Centering the NIR camera on the HIZOA position has a high probability of locating the counterpart in the image. Thus, the detection of these H I sources depends only on their H I mass and the stellar density and dust extinction of the region in which they lie. Some NIR fields contain more than one possible counterpart to the H I galaxy and therefore need more attention. All sources identified as H I sources in the NIR fields were inspected by eye and information from their H I profiles used to identify the H I counterpart. A galaxy with double-horn H I profile was normally identified as an edge-on galaxy in the NIR image, while a galaxy with a Gaussian profile was usually identified with a face-on galaxy in the NIR image.

The final NIR catalogue contains counterpart galaxies to 674 sources from all three HIZOA catalogues (HIZOA-S; Staveley-Smith et al. 2016, HIZOA-N; Donley et al. 2005, GB; Kraan-Korteweg et al. 2008). A single counterpart was found for 527 galaxies, while more than one counterpart was found for 147 galaxies.

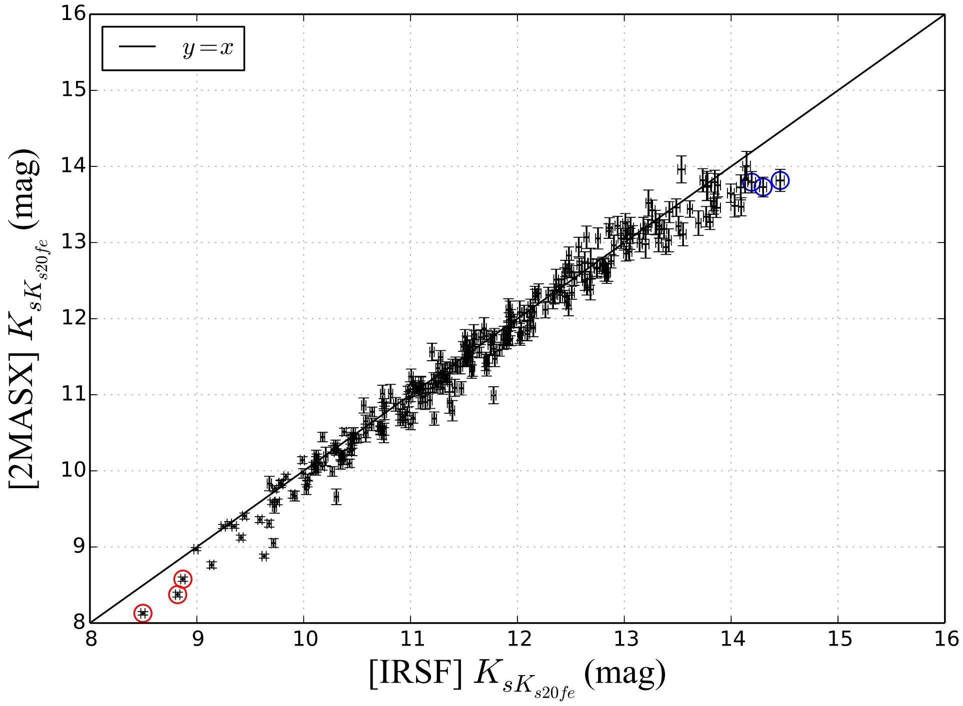

Figure 4.7: A comparison between the K_s-band K_{s20} fiducial elliptical aperture magnitudes in this catalogue and the same parameter reported in the 2MASX catalogue.

4.5.2 2MASS counterparts

Of the 1044 NIR galaxies in the final catalogue, 285 have counterparts in the 2MASX catalogue (180 HIZOA plus 105 2MASS). We used a search radius of only 1 arcsec because of the high positional accuracy of both 2MASS and the IRSF. In Fig. 4.7 we compare our measured K_s-band K_{s20} fiducial elliptical aperture magnitudes with the same parameter from the 2MASX catalogue (Jarrett et al. 2000; 2003) for these 285 galaxies.

Fig. 4.7 shows good agreement between the K_{s20} measured for this catalogue and the same parameter reported in the 2MASX catalogue. Small systematic deviations are visible for both faint galaxies ($>$ 14 mag) marked as blue circles and bright galaxies ($<$ 9 mag) marked as red circles. The deviation for bright galaxies is due to the difference of the pixel scale between these two instruments. The IRSF has pixel scale of 0.45 arcsec pixel^{-1} compared to 2.0 arcsec pixel^{-1} for the 2MASX survey. Small, faint stars superimposed

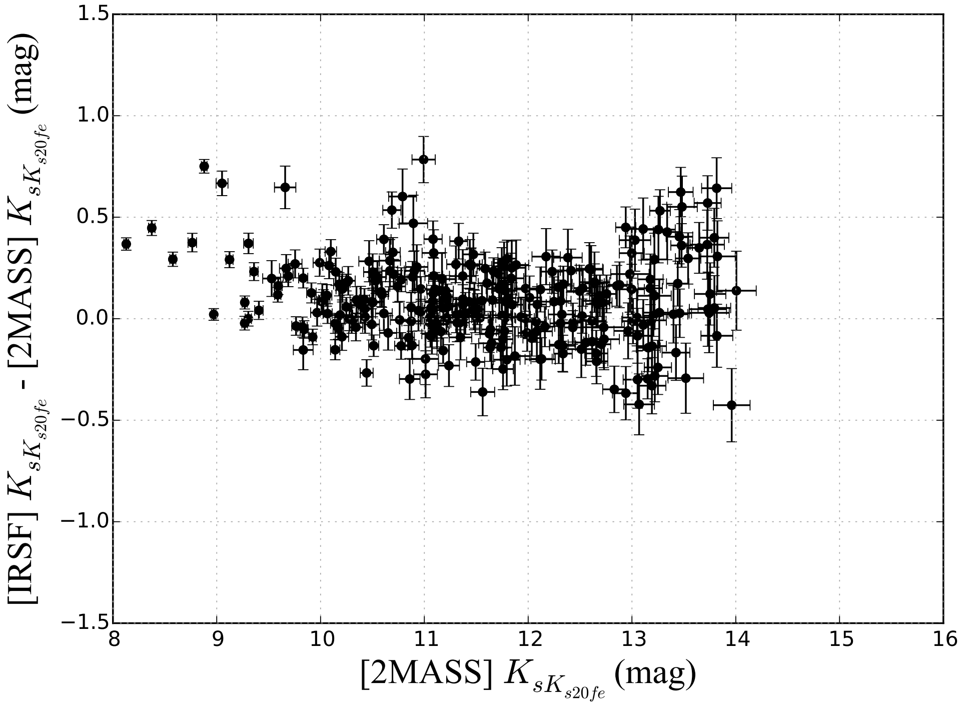

Figure 4.8: A detailed comparison between the K_s-band K_{s20} fiducial elliptical aperture magnitudes in this catalogue and the same parameter reported in the 2MASX catalogue.

on bright galaxies can not be resolved by 2MASX. Thus, the magnitudes of these galaxies are over-estimated because these stars are not subtracted from the image before measuring the photometry. The high resolution of the IRSF instrument leads to more effective star-subtraction and thus more accurate photometry which is vital when working in the ZOA. The deviation for faint galaxies is a bias due to the completeness limit of 2MASX. The scatter should to be on both sides of the one-to-one line but there are no 2MASX galaxies fainter than 14 mag. A detail comparison is also shown in Figure 4.8.

The uncertainties on the delta magnitude is calculated using the propagation of error.

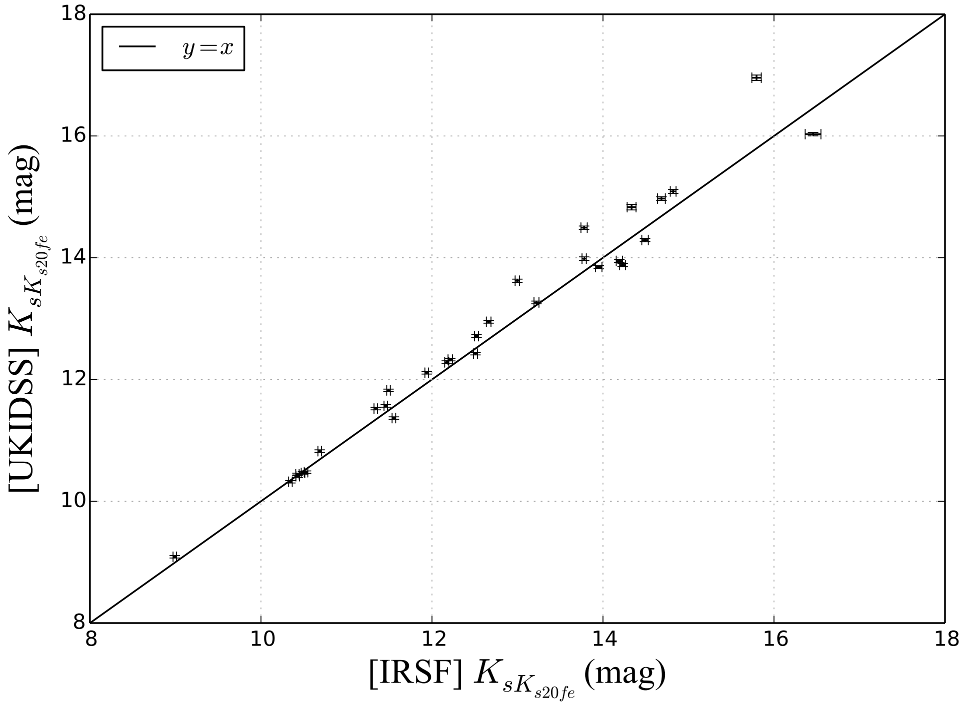

Figure 4.9: A comparison between the K_s-band K_{s20} fiducial elliptical aperture magnitudes measured from the IRSF images and the same parameter measured from the UKIDSS GPS images using a modified version of the IRSF photometry pipeline. The solid line is the one-to-one line.

4.5.3 UKIDSS counterparts

The UKIDSS GPS (Lucas et al. 2008) overlaps with the HIZOA survey in the northern extension published by Donley et al. (2005). We used the publically accessible *UKIDSS DR8 plus* data release to search for counterparts. Given the high positional accuracy of both the IRSF and UKIDSS GPS, the minimum available search radius of 3 arcsec was used. We found 30 confirmed counterparts in the UKIDSS GPS survey. A modified version of our IRSF photmetry pipeline was used to consistently measure the photometric parameters for these galaxies from the UKIDSS GPS images.

Fig. 4.9 shows the comparison between the K_s-band K_{s20} fiducial elliptical aperture magnitudes measured from the IRSF images and the same parameter measured from the UKIDSS GPS images. The solid line in Fig. 4.9 is the one-to-one line. Excellent agreement between the IRSF and UKIDSS

GPS photometry can be seen. The pixel scale for the UKIDSS GPS images is 0.4 arcsec pixel^{-1}, which is comparable to the IRSF pixel scale of 0.45 arcsec pixel^{-1}. The average seeing of 1.54 arcsec for the UKIDSS GPS images used in this comparison is similar to that of 1.38 arcsec for the IRSF survey. This agreement shows that the IRSF imaging does not suffer from foreground contamination, even after star removal, nor does it adversely under-estimate the isophotal flux of the ZOA galaxies. It is satisfying to see this agreement between photometric parameters because we plan to extend the current TF project to the northern ZOA using the UKIDSS GPS survey along with H I data from the Nançay Radio Telescope.

4.6 Summary

In this chapter, we present the observations, data reduction and final catalogue for 1044 NIR galaxies, in the J, H, and K_S bands, in the southern ZOA. The observations were conducted between 2006 and 2013 using the IRSF, a 1.4-m telescope situated at the South African Astronomical Observatory site in Sutherland. This resulted in observations of all galaxies in the three blind systematic deep HIZOA surveys (Donley et al. 2005, Kraan-Korteweg et al. 2008, Staveley-Smith et al. 2016).

The quality of the images is discussed in detail. The survey has an average seeing and zero point magnitude of 1.38 arcsec and 20.1 mag in the K_s band, respectively. These values agree well with those from previous surveys done with the same instrument (Riad 2010). The mean error of the measured isophotal magnitudes is 0.02 mag which is sufficient for the TF analysis.

The completeness as a function of stellar density and dust extinction was found to be dependent on the H I mass of each galaxy. The detection rate was found to be 100 per cent for massive galaxies ($\log M_{HI}[M_\odot] > 8.5$) in regions with stellar density of $\log(N_{K_s<14}/\mathrm{deg}^2) \leq 4$. However, for small galaxies ($\log M_{HI}[M_\odot] < 8.5$) the detection rate is 75 per cent in regions of $\log(N_{K_s<14}/\mathrm{deg}^2) \leq 4$. This detection rate drops to 50 per cent and 30 per cent for regions within $\log(N_{K_s<14}/\mathrm{deg}^2) > 4$ for massive and small galaxies, respectively. The same conclusion was found for the detection rate as a function of dust extinction. Although the detection rate was high for massive galaxies in regions up to $E(B-V) = 1$ mag ($A_v = 3.1$ mag), it was very low for small galaxies even in regions with very low dust extinction.

We identified 674 galaxies in the final NIR catalogue that have confirmed counterparts in the three HIZOA catalogues. Counterparts from similar NIR surveys are presented. We found 285 2MASX galaxies have counterparts in our final catalogue. However, only 30 galaxies in the UKIDSS Galactic Plane Survey have counterparts in our final NIR catalogue because UKIDSS GPS only overlaps with our survey in its northern extension.

A comparison of our IRSF pointed observations with the 2MASX and UKIDSS GPS surveys was performed for these galaxies. We found good agreement between the K_s-band K_{s20} fiducial elliptical aperture magnitude presented in this chapter and the same parameter reported in the 2MASX catalogue. We detect only small deviations for both faint galaxies (> 14 mag) and bright galaxies (< 9 mag). The deviation for bright galaxies is due to the difference of the pixel scale between IRSF and 2MASX instruments. While the deviation for the faint galaxies is a bias due to the completeness limit of 2MASX.

Good agreement was found between the K_s-band K_{s20} fiducial elliptical aperture magnitudes measured from the IRSF data and the UKIDSS GPS data. This agreement confirms that the IRSF images are of equal quality to the UKIDSS GPS images, which are one magnitude deeper. This indirectly implies that IRSF photometry does not suffer from foreground contamination, after star removal, nor does it under-estimate the isophotal flux of the ZOA galaxies. The measurement of UKIDSS photometry is regarded as a pilot project of our TF survey in the northern ZOA.

This chapter is the third in a series towards the full ZOA TF analysis. The data presented here will be used with the recently calibrated TF relation in Said et al. (2015) as well as the H I data presented in Said et al. (2016) to derive distances and peculiar velocities for inclined spiral galaxies in the southern ZOA. An extension of this project into the northern ZOA already started last year with the H I observations of bright inclined 2MASS galaxies using the Nançay Radio Telescope.

Chapter 5

H I mass function and peculiar velocities in the southern ZOA

In this Chapter, we use the calibrated Tully-Fisher relation, the deep NIR (J, H, and K_s-band) imaging, and the high signal-to-noise H I data to derive distances and peculiar velocities for a homogeneous sample of inclined spiral galaxies located behind the dust and stellar density of our own Galaxy. This sample consists of 287 galaxies covering the whole southern Zone of Avoidance ($|b| < 5°$), out to redshift $z \sim 0.03$. We construct the H I mass function using both $1/V_{max}$ and the two-dimensional stepwise maximum likelihood methods. 873 galaxies in the HIZOA survey that meet our selection criteria are included in the derivation of this H I mass function. The final parameters of the H I mass function are $\alpha = -1.30 \pm 0.05$, $\log(M^*_{HI}/M_\odot) = 9.97 \pm 0.04$, and $\phi^* = (5.2 \pm 0.8) \times 10^{-3}$ Mpc^{-3}. Comparisons of these parameters with values from the literature show that the faint-end slope agrees within the uncertainties with both ALFALFA and HIPASS surveys, while the knee of the H I mass function agrees better with the ALFALFA survey than the HIPASS survey. The H I mass function allows predictions for the Malmquist bias. We also present the distribution of the derived logarithmic distance ratio $\log(d_z/d^*_{TF})$ and its associated error. The distribution of the logarithmic distance ratio is almost a Gaussian centered around $\log(d_z/d^*_{TF}) = 0.1$ with more positive peculiar velocities than the 2MTF distribution which is also Gaussian but centered around $\log(d_z/d^*_{TF}) = 0.0$. The associated errors are smaller than the 2MTF errors because of the deeper and higher angular resolution of the

IRSF observations compared to 2MASS. We use these peculiar velocities to describe the motion of galaxies in and around the three major LSS feature in the HIZOA survey, i.e. Puppis, the GA, and the LV. We first review the three most prominent large-scale structures in the southern ZOA, in particular what was newly learned about them from the HIZOA redshift survey. We map the peculiar velocity field around these structures out to redshift $z \sim 0.03$. We find an indication of outflow in the Puppis region, clear infall into the Great Attractor, and draining of the Local Void. The here derived velocity field is compared to the 2MTF observations, 2MRS, and PSCz reconstructions.

5.1 Introduction

The Hubble law states that the recession velocity of a galaxy is directly proportional to its distance:

$$cz = H_0 r, \tag{5.1}$$

where cz is the recession velocity of that galaxy, r is its distance, and H_0 is the Hubble parameter, whose value remains as a source of ambiguity between the local measurements ($H_0 = 73.24 \pm 1.74$ km s^{-1} Mpc^{-1}; Riess et al. 2011; 2016, Efstathiou 2014) and the model-dependent measurements from the Planck temperature data ($H_0 = 67.8 \pm 0.9$ km s^{-1} Mpc^{-1}; Planck Collaboration et al. 2014a; 2016). However, we do not live in a perfectly smooth and homogeneous universe and most of the galaxies in the Universe violate this law by having velocities above or below their expected Hubble velocities. This can be accommodated in a modified Hubble law as follows:

$$cz = H_0 r + \hat{r} \cdot [v(r) - v(0)], \tag{5.2}$$

where $\hat{r}$ is the unit vector in the direction of that galaxy, $v(r)$ the galaxy peculiar velocity, and $v(0)$ is the observer peculiar velocity in the same reference frame. Peculiar velocities arise as a result of the gravity of over-dense regions formed by the gravitational instability of tiny initial perturbations in the uniform background. In linear perturbation theory the density fluctuations are small,

$$\delta(r) = \frac{\rho(r) - \rho_0}{\rho_0} < 1 \tag{5.3}$$

where δ is the density contrast, ρ is the mass density field, and ρ_0 is the mean mass density. In this regime, peculiar velocities are directly proportional to the gravitational acceleration (Peebles 1980; 1993, Strauss & Willick 1995):

$$v(r) = \frac{H_0 f}{4\pi} \int d^3r' \delta(r') \frac{r' - r}{|r' - r|^3}, \tag{5.4}$$

with km s^{-1} as the unit for distance which makes Hubble parameter in Eq. 5.4 equal to unity. f is the growth rate of the perturbations[*]. Equation 5.4 shows that through measurement of the peculiar velocities we can imply the fluctuation of the mass density and the growth of the perturbations.

Following Lahav et al. (1991) the growth rate f can be parametrized as a function of the cosmological density parameter Ω and the cosmological constant Λ

$$f(\Omega, \Lambda)_{z=0} = \Omega^{\gamma} + \frac{\Lambda}{210 H_0^2}(1 + \frac{\Omega}{2}) \tag{5.5}$$

where for a flat Λ cold dark matter model, $\gamma = 0.55$ (Wang & Steinhardt 1998). Therefore, in addition to obtaining constraints on cosmological parameters we can search for other alternative models of gravity.

In this Chapter we aim to measure distances and peculiar velocities to all inclined spiral galaxies in the southern ZoA that have high-quality NIR images and robustly determined H I profiles. This will form the first part of the main project of providing the first ever truly all-sky peculiar velocity survey by combining data from this thesis and data from the northern ZoA with the 2MTF data. By the end of this project we wish to give a definite answers to two main questions:

1. Whether the bulk flow resulting from our all-sky, large, and homogeneous sample is consistent with the predictions from the Λ cold dark matter model (Nusser & Davis 2011, Turnbull et al. 2012, Hong et al. 2014, Scrimgeour et al. 2016) or we do not live in Λ cold dark matter universe and should test alternative models (Kashlinsky et al. 2008, Watkins et al. 2009, Feldman et al. 2010)

2. Whether the discrepancy between the dipole of the CMB which is a

---

[*] The derivation of equation 5.4 from the continuity equation can be found in Peebles (1993) (section gravitational instability in Chapter 5) or in Strauss & Willick (1995) (Section 2.2)

Doppler effect due to the Sun's motion (Hinshaw et al. 2009, Planck Collaboration et al. 2014b) and the peculiar velocity induced from an all-sky sample is because of the ZoA (Kraan-Korteweg & Lahav 2000, Loeb & Narayan 2008) or is it because of the depth of surveys Bilicki et al. (2011), Nusser et al. (2014) or both (Kraan-Korteweg et al. 2017).

This Chapter is organized as follows: In Sect. 5.2 a brief summary of the newly calibrated Tully-Fisher relation and its associated intrinsic scatter is presented. In Sect. 5.3, we discuss the H I and NIR ZOA data sample which will be used in our calculations. Sect. 5.4 presents our method of calculating the distances and peculiar velocities which includes a discussion of the Malmquist bias correction method. The latter is based on the derivation of the HIZOA H I mass function and the completeness of our sample. We further present the compilation of TF-based distances and peculiar velocities of southern ZOA galaxies after applying correction of all statistical biases. In Sect. 5.5 we review the large-scale structures in the southern ZOA that were uncovered with the HIZOA survey. In Sect. 5.6 we present the velocity field around these major large-scale structures in our ZOA-TF sample. In Sect. 5.7 we discuss the resulting flow fields and compare it to the predicted velocity field from reconstructions, such as 2MRS and PSCz. Our results are summarized in Sect. 5.8.

5.2 Tully-Fisher Template Relation

In Chapter 2, we re-calibrated the Tully-Fisher relation using the isophotal magnitudes in J, H, and K_s-band of 888 galaxies (Said et al. 2015). The isophotal TF re-calibration is necessary because most of the published TF relations are based on total magnitudes which are not attainable in the ZoA (or other dust obscured areas) because of dust extinction and high stellar density. While the sample used for the calibration contains only galaxies at high Galactic latitudes, all parameters and methods should be consistent with the sample used for the measurements of TF-based distances and peculiar velocities. After applying all corrections for magnitudes and H I 21-cm linewidths, Said et al. (2015) found the final isophotal TF relations to have the form:

$$\begin{aligned} M_J - 5\log h &= -20.951 - 9.261(\log W - 2.5), && (5.6a)\\ M_H - 5\log h &= -21.682 - 9.288(\log W - 2.5), && (5.6b)\\ M_{K_s} - 5\log h &= -21.861 - 10.369(\log W - 2.5). && (5.6c) \end{aligned}$$

After very careful considerations of all sources of uncertainty in the above relations the intrinsic scatter of these relations have the form of:

$$\begin{aligned} \epsilon_{int,J} &= 0.46 - 0.90(\log W - 2.5), && (5.7a)\\ \epsilon_{int,H} &= 0.47 - 0.94(\log W - 2.5), && (5.7b)\\ \epsilon_{int,K_s} &= 0.46 - 0.83(\log W - 2.5). && (5.7c) \end{aligned}$$

Equations 5.6 & 5.7 will be used as a benchmark or standard tool in deriving the distances and peculiar velocities of galaxies in our ZOA-TF sample as introduced in the coming section. Equation 5.7 demonstrate that the actual intrinsic scatter of the isophotal TF is smaller than the one based on total magnitudes for low surface brightness galaxies (detailed comparison can be found in Chapter 2).

5.3 ZOA DATA

The required two sets of raw data to calculate the TF based distances and peculiar velocities are:

1. H I 21-cm observations of spiral galaxies in the ZOA from which to extract the redshift and the rotational velocity
2. follow-up deep NIR imaging of the H I sources to measure the apparent magnitude of each galaxy.

The coming subsections present the corrections that needed to be made to arrive at the data set that is consistent with the parameters for the NIR isophotal TF calibration.

5.3.1 H I data

The first data set is the 21 cm H I-line spectra of 394 inclined, $(b/a)^\circ < 0.5$, spiral galaxies selected from the HIZOA survey (Staveley-Smith et al. 2016) was put together by re-observing a substantial sub-sample of galaxies using the narrow band on Parkes radio telescope to improve the velocity resolution (Said et al. 2016). The average signal-to-noise ratio for this H I survey was 14.7 which is adequate for TF studies.

Five different types of line-widths are measured, which are:

1. W_{P20}: the linewidth at 20% of the peak flux−rms,
2. W_{M50}: the linewidth at 50% of the mean flux,
3. W_{P50}: the linewidth at 50% of the peak flux−rms,
4. W_{F50}: the linewidth at 50% of the peak flux−rms, measured with a polynomial fit to both sides of the profile,
5. W_{2P50}, the linewidth at 50% of the peak flux−rms measured at each of the two peaks.

The full presentation of this data set can be found in Chapter 3 of this thesis. To be consistent with the calibration method, we used the linewidth W_{F50} and the equation given by Springob et al. (2007) to correct for inclination:

$$W = [\frac{w_{F50} - \Delta_s}{1+z} - \Delta_t]\frac{1}{\sin i} \tag{5.8}$$

where Δ_t is the amount of turbulent motion and Δ_s is the instrumental correction. For the fraction of turbulent motion, $\Delta_t = 6.5$ km s^{-1} is used, and for the instrumental correction $\Delta_s = 2\Delta v\lambda$ (Springob et al. 2005). The parameter λ is a piece-wise defined function of signal-to-noise ratio (SNR) and channel separation:

$$\lambda = \lambda_1(\Delta v) \qquad \log(\text{SNR}) < 0.6, \tag{5.9a}$$
$$\lambda = \lambda_2(\Delta v) + \lambda_2'(\Delta v)\log(\text{SNR}) \; 0.6 < \log(\text{SNR}) \leq 1.1, \tag{5.9b}$$
$$\lambda = \lambda_3(\Delta v) \qquad \log(\text{SNR}) > 1.1. \tag{5.9c}$$

Table 5.1: Velocity width instrumental correction parameters

(Δv) (km s $^{-1}$)	Smoothing	$\lambda_1(\Delta v)$	$\lambda_2(\Delta v)$	$\lambda_2'(\Delta v)$	$\lambda_3(\Delta v)$
< 5	H	0.005	-0.468	0.785	0.395
5-11	H	$0.04\Delta v - 0.18$	$0.05\Delta v - 0.72$	$-0.03\Delta v + 0.92$	$0.02\Delta v + 0.28$
> 11	H	0.227	-0.1523	0.623	0.533
< 5	B	0.020	-0.4705	0.820	0.430
5-11	B	$0.05\Delta v - 0.24$	$0.04\Delta v - 0.67$	$0.02\Delta v + 0.72$	$0.06\Delta v - 0.12$
> 11	B	0.332	-0.2323	0.940	0.802

Table 5.1 shows the values of λ as given in (Springob et al. 2005). The inclination i is derived from the J-band ellipticity $\epsilon_J = 1 - (b/a)_J$ via

$$\cos^2 i = \frac{(1-\epsilon)^2 - q_0^2}{1 - q_0^2} \tag{5.10}$$

following Giovanelli et al. (1997). The parameter $(a/b)_J$ is the J-band axial ratio fit to the 3σ isophote (the isophote which corresponds to a surface brightness that is $\sim$ 3 times above the background noise). The J-band axial ratio $(b/a)_J$ is the best tracer of the inclination, it suffers less from the effect of the bulge than the H, and K_s-bands when the 3 σ isophote is close to the center (Masters et al. 2003).

Additionally, the peculiar velocities need to be in the CMB frame. We transform the heliocentric velocity v_{hel} to v_{CMB} using the model given by Fixsen et al. (1996):

$$v_{\text{CMB}} = v_{\text{hel}} + v_{\text{apex}}[\sin b \sin b_{\text{apex}} + \cos b \cos b_{\text{apex}} \cos(l - l_{\text{apex}})] \tag{5.11}$$

where $v_{\text{apex}} = 371.0$ km s^{-1}, $l_{\text{apex}} = 264^\circ\!.14$, and $b_{\text{apex}} = 48^\circ\!.26$ are the velocity and Galactic coordinates of the apex vector describing the relative motion of the Sun with respect to the CMB.

5.3.2 NIR data

The second data set consists of the deep NIR photometric imaging of all the HIZOA galaxies. Said et al. (2016) presents a deep near-infrared (NIR; J, H, and K_s bands) photometric catalogue of sources from the Parkes H I Zone of Avoidance (HIZOA) survey. Observations were conducted of over a thousand galaxies using the Japanese Infrared Survey Facility (IRSF), a 1.4-m telescope situated at the South African Astronomical Observatory site in Sutherland.

Full representation of this data set can be found in Chapter 4. The corrections to the absolute magnitudes is calculated in the same manner as for the template relations as:

$$M_{\rm corr} - 5{\rm log}h = m_{\rm obs} - A_X - I_X - k_X - 5{\rm log}v_{\rm CMB} - 15, \tag{5.12}$$

where the parameters A_X, I_X, and k_X indicate corrections to extinction due to dust in our Galaxy, internal extinction to the galaxy itself, and a cosmological k-correction, respectively.

For Galactic extinction we used the correction provided in Riad et al. (2010). For internal extinction, we used the correction from Said et al. (2015). For the k-correction we used the procedure given by Poggianti (1997) and used by Masters et al. (2008) and Said et al. (2015). The correction model for the axial ratio b/a due to dust extinction derived by Said et al. (2015) is also applied. Additional corrections for the morphological type dependence adopted (Said et al. 2015).

5.4 TF based distances and peculiar velocities

With the above mentioned three ingredients in hand, the absolute magnitude can be derived from the rotational velocity with the template relation. This then leads to a distance independent of redshift using the distance modulus.

5.4.1 Calculating the logarithmic distance ratio

Following Hong et al. (2014) and Springob et al. (2016), we work with the logarithmic distance ratio instead of the linear peculiar velocities because the distance errors are log-normal. We define the logarithmic distance ratios to have the form of:

$$\log(d_z/d^*_{TF}) = \frac{-\Delta M}{5}, \tag{5.13}$$

where $\Delta M = M_{obs} - M(W)$. Figure 5.1 shows the TF relations in the J, H, and K_s-band from which we calculate ΔM. The dashed lines in the three panels are the three template TF relations in J, H, and K_s bands (equations 5.6). The dark shaded area shows the intrinsic scatter in the TF relations (equations 5.7) and the light shaded area denotes three times the intrinsic scatter, $\pm 3\epsilon_{int}$. In Figure 5.1 we cut out outlier galaxies from our sample, i.e. the one beyond 3σ.

d^*_{TF} is the distance to the galaxy derived from the TF relation, it is not yet corrected for selection bias. The corresponding distributions of the uncorrected logarithmic distance ratio $\log(d_z/d^*_{TF})$ in J, H, and K_s bands are shown in Fig. 5.2. This figure shows that the distributions in all three bands are almost identical with the peak between 0.0 and 0.1 and the median value for the $\log(d_z/d^*_{TF})$ are 0.05, 0.04, and 0.05 for J, H, and K_s bands, respectively. For the rest of this Chapter, we will combine the three bands by using the median.

Figure 5.3 shows a histogram of the distribution of the logarithmic distance ratio derived by combining three wavebands J, H, and K_s for each galaxy, it is not yet corrected for the selection bias.

We used the propagation of errors to calculate the error on the logarithmic distance ratios $\log(d_z/d^*_{TF})$:

$$\sigma_{\log(d_z/d^*_{TF})} = \frac{\sigma_{\Delta M}}{5} \tag{5.14a}$$

$$\sigma^2_{\Delta M} = \sigma^2_M + \sigma^2_{M(W)} \tag{5.14b}$$

$$\sigma^2_M = \sigma^2_{obs} + (\frac{5}{v_{CMB}\ln 10})^2 \sigma^2_{v_{CMB}} \tag{5.14c}$$

$$\sigma^2_W = (\frac{1}{1+z})^2 \sigma^2_{W_{F50}} + (W\frac{\cos i}{\sin i})^2 \sigma^2_i \tag{5.14d}$$

$$\sigma^2_i = (\frac{1-\epsilon}{1-q_0^2}\frac{1}{\cos i \sin i})^2 \sigma^2_\epsilon \tag{5.14e}$$

$$\sigma^2_{M(W)} = (\frac{b}{W\ln 10})^2 \sigma^2_W + \epsilon^2_{int}. \tag{5.14f}$$

Figure 5.4 shows the distribution of the error of the logarithmic distance ratios $\log(d_z/d^*_{TF})$ uncorrected for the selection bias, derived by combining data from all three wavebands J, H, and K_s.

5.4.2 HI mass function and Malmquist bias Correction

The logarithmic distance ratios $\log(d_z/d^*_{TF})$ derived in the previous subsection and its associated errors are subject to Malmquist bias and careful corrections

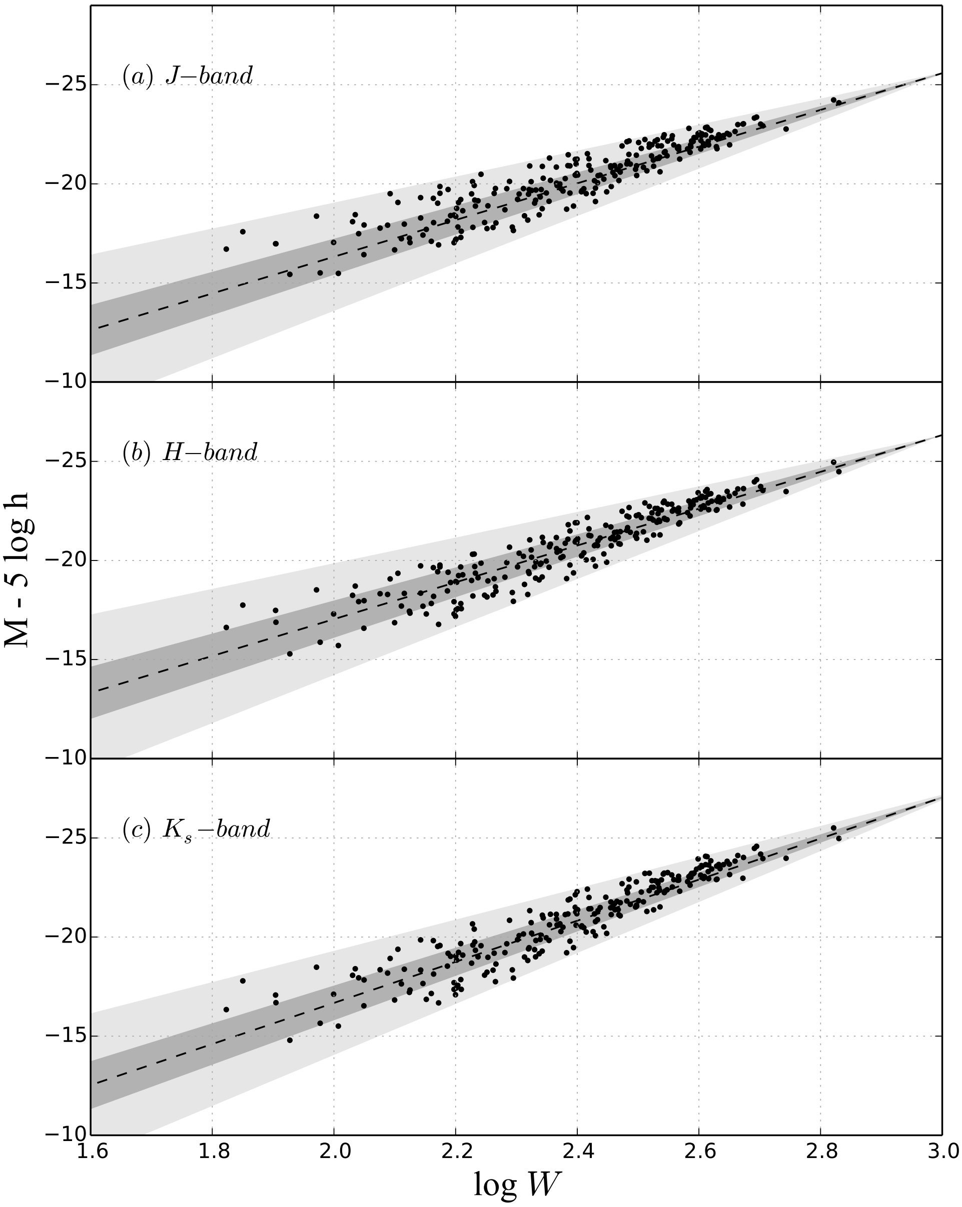

Figure 5.1: Tully-Fisher relation for the ZOA galaxies. The dashed line denotes the TF relations in J, H, and K_s-band (equations 5.6). The dark shaded area shows the intrinsic scatter (equations 5.7) and the light shaded area represents three times the TF intrinsic scatter.

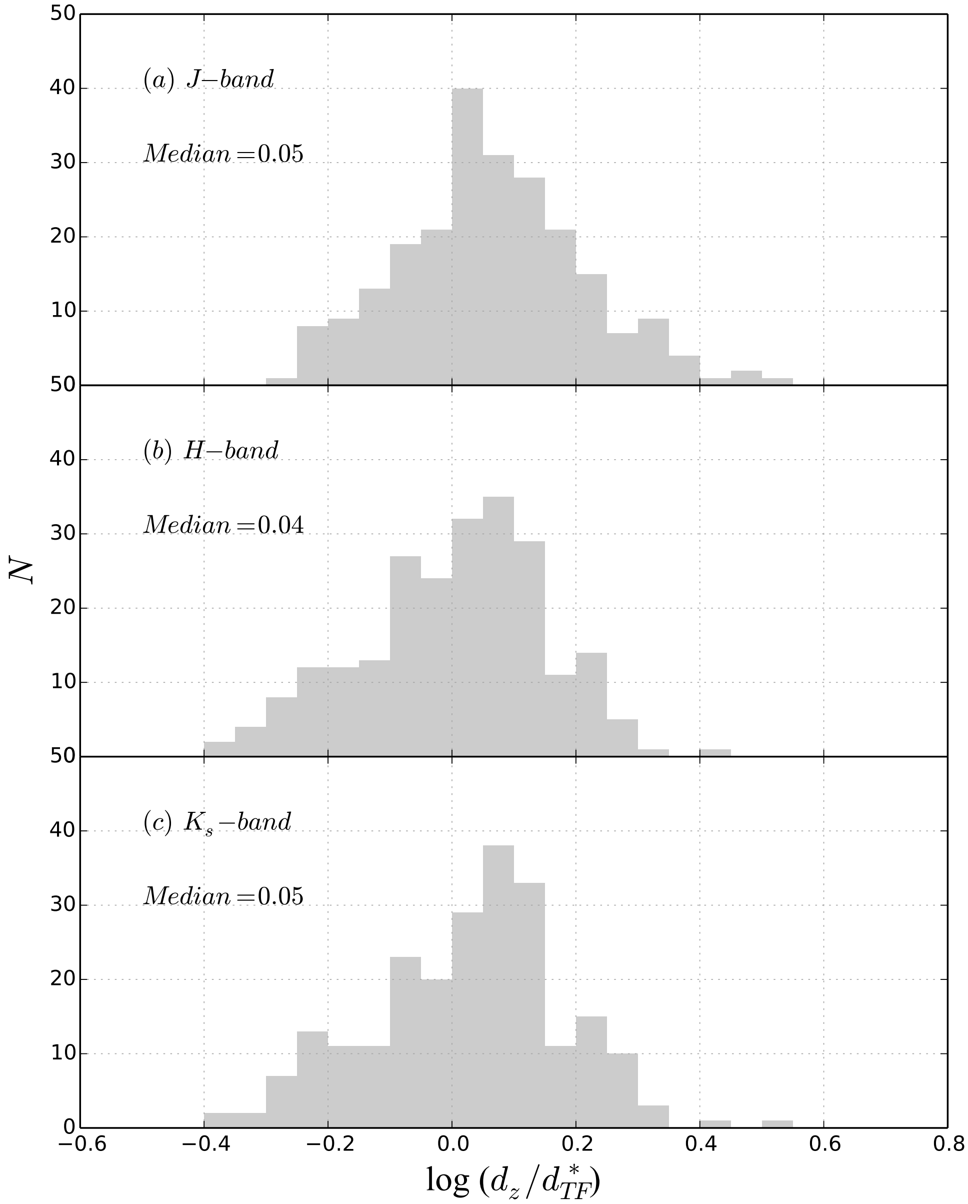

Figure 5.2: The distribution of the uncorrected logarithmic distance ratio $\log(d_z/d^*_{TF})$ in J, H, and K_s bands. The median value of the logarithmic distance ratio $\log(d_z/d^*_{TF})$ in each band is printed on the left-hand side of each panel.

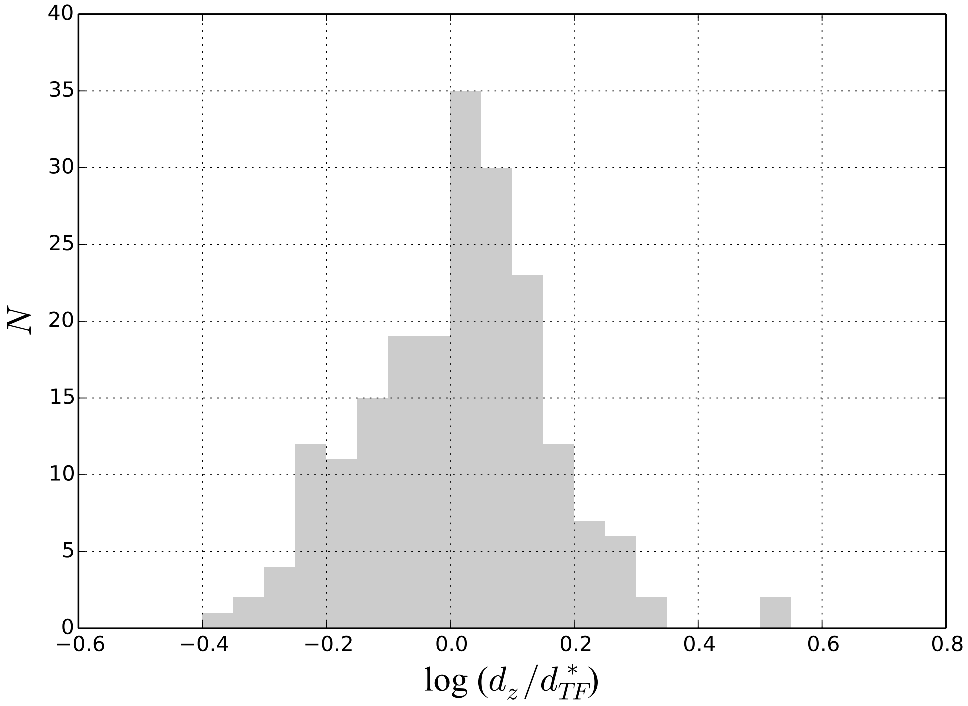

Figure 5.3: The distribution of the uncorrected logarithmic distance ratio $\log(d_z/d^*_{TF})$ derived by combining all three wavebands J, H, and K_s, i.e. for each galaxy we use the median of the three peculiar velocity measurements.

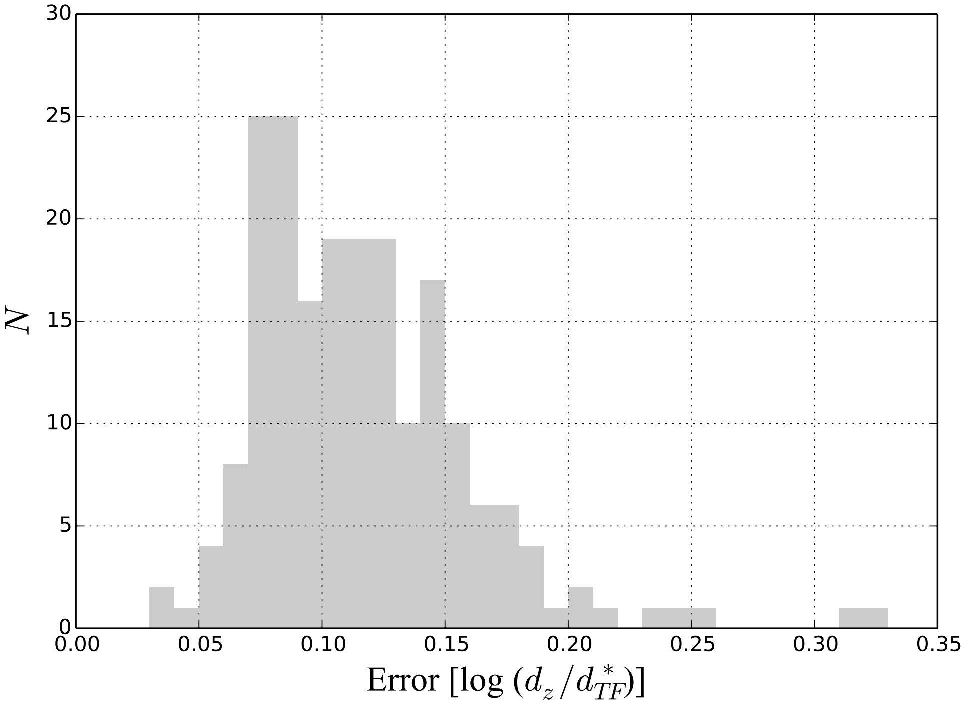

Figure 5.4: The distribution of the uncorrected error of the logarithmic distance ratios $\log(d_z/d^*_{TF})$ derived by combining all three J, H, and K_s wavebands.

are needed before using them for any cosmological applications. There are two types of Malmquist bias: the inhomogeneous Malmquist bias and the homogeneous Malmquist bias. Working in redshift space instead of real space makes the inhomogeneous Malmquist bias negligible (Strauss & Willick 1995).

In this section we will deal only with the homogeneous Malmquist bias. This type of selection bias is a consequence of two effects: (1) volume effect and (2) selection effect (see, Springob et al. 2016 for more details about both effects). We adopt a similar procedure as used in the 2MTF, i. e., construct an H I mass function (instead of a luminosity function) and calculating the fraction of the sample that is included in our final TF sample for a given H I flux bin (instead of magnitude bin).

Derivation of the HIZOA H I mass function

We use the H I mass function because our sample is based on a systematic H I survey, i.e., HIZOA. We derive the H I mass function for all galaxies in the HIZOA survey that meet our selection criteria. The HIZOA survey has been previously characterised with three completeness limits: (1) flux limit, (2) mean flux density limit and (3) the hybrid limit (see Table 4 in Staveley-Smith et al. 2016). We used the V/V_{max}-test (Schmidt 1968) to measure the uniformity of the galaxy distribution within the survey volume for each limit. The mean of the statistic V/V_{max} was 0.407 ± 0.009, 0.454 ± 0.009, and 0.344 ± 0.008 for flux limit, mean flux density limit, and the hybrid limit, respectively. The expected mean V/V_{max} value for a complete and homogeneous sample is 0.5. Values smaller than 0.5 mean that the sample is more incomplete at larger distances than at lower distances or that the galaxy density is lower.

The $1/V_{max}$ (Schmidt 1968) method has been widely used because of its simplicity. The number density of galaxies is simply calculated by summing the $1/V_{max}$ in bins of H I masses as follows:

$$\phi(M_{HI})_j = \frac{1}{\Delta M_{HI}} \sum \frac{1}{V_{max,i}}, \tag{5.15}$$

where $\phi(M_{HI})_j$ is the number density of galaxies in bin $j = 1, 2, ..., N_{M_{HI}}$ and $N_{M_{HI}}$ is the number of bins of H I masses. $V_{max,i}$, is the maximum volume a galaxy $i = 1, 2, ..., N_g$ can be detected in and calculated as

$$V_{max,i} = \frac{4\pi f_{sky}}{3}\left(\frac{M_{HI,i}}{2.356\times 10^5 S_{lim} W_{50,i}}\right)^{3/2} \tag{5.16}$$

$S_{lim} = 22$ mJy represents the mean flux density completeness limit of the HIZOA survey (Donley et al. 2005, Staveley-Smith et al. 2016), f_{sky} is the fraction of the sky covered by the survey, and $M_{HI,i}$ is given by,

$$M_{HI,i} = 2.356\times 10^5 D_i^2 F_{HI,i}, \tag{5.17}$$

where D_i is the distance in megaparsecs and $F_{HI,i}$ is the flux integral.

We fit a Schechter function (Schechter 1976) of the form:

$$\Phi(M_{HI}) = \ln 10\phi^*(\frac{M_{HI}}{M_*})^{\alpha+1} e^{-\frac{M_{HI}}{M_*}}, \tag{5.18}$$

to the derived H I mass function. The best fit parameters are $\alpha = -1.35\pm 0.04$, $\log(M^*_{HI}/M_\odot) = 9.94\pm 0.24$, and $\phi^* = (10.65\pm 4.11)\times 10^{-3}$ Mpc^{-3}.

The main problem of the $1/V_{max}$ method is its sensitivity to large-scale structures because it assumes that galaxies are uniformly distributed in space. The HIZOA survey is far from uniform because it encompasses many large-scale structures such as the Great Attractor and the Local Void. This means that these structures will affect each bin in different ways. Therefore, we also derived the HIMF using the two-dimensional stepwise maximum likelihood method (2DSWML: Loveday 2000, Zwaan et al. 2003; 2005).

The 2DSWML method is independent of density fluctuations. This method finds the maximum likelihood solutions for the number density of galaxies ϕ_{jk} as a function of H I mass and velocity width by iterating from an initial guess as:

$$\phi_{jk} = \frac{\sum_{i=1}^{N_g} \delta(M_i - Mj, W_i - W_k)}{\sum_{i=1}^{N_g} \frac{H_{ijk}\Delta M\Delta W}{\sum_{l=1}^{N_M}\sum_{m=1}^{N_W} \phi_{lm} H_{ilm}\Delta M\Delta W}}, \tag{5.19}$$

where δ_{ijk} is a function equals one if a galaxy i belongs to the H I mass bin j and velocity width bin k, and equals zero otherwise. The function H_{ijk} equals the fraction available of the bin jk in which a galaxy i resides (Zwaan et al.

2003).

Equation 5.19 can be interpreted in different ways. The denominator for example, presents the effective volume available to galaxies in bin jk, and can be modified to find the effective volume available to each galaxy as in Zwaan et al. (2005). Marginalizing Eq. 5.19 over the velocity width W gives the H I mass function (Martin et al. 2010, Jones et al. 2016) while marginalizing over the H I mass M_{HI} gives the velocity width function (Papastergis et al. 2011). In this Chapter I will focus only on the HIMF.

We used Eq. 5.19 to evaluate the effective volume available to each single galaxy that meets the selection criteria of the TF analysis after applying the completeness function of the HIZOA survey. Figure 5.5 shows the galaxy density distribution in the $M_{HI} - W_{50}$ plane colour-coded by the reciprocal of the effective volume available to each galaxy in logarithmic scale. There is a clear strong correlation between the line-width and the effective volume. The histogram of the line-width on the right-hand side of the plot shows that our sample contains a fair distribution of large and small galaxies in a Gaussian shape.

We then marginalized ϕ_{jk} over the velocity width to calculate the HIMF as:

$$\phi_j = \sum_{k=1}^{N_W} \phi_{jk} \Delta W \tag{5.20}$$

Figure 5.6 shows the result of this process. The dots present the number space density in H I mass bins, the solid line is the best fit Schechter function of the form presented in Eq. 5.18, and the error bars are the Poisson errors. The final parameters of the H I mass function are:

- $\alpha = -1.30 \pm 0.05$
- $\log(M^*_{HI}/M_\odot) = 9.97 \pm 0.04$
- $\phi^* = (5.2 \pm 0.8) \times 10^{-3}$ Mpc^{-3}

The normalization is not needed for the Malmquist bias correction. For comparison, we add to Fig. 5.6 the Zwaan et al. (2003) results as a dotted line and Martin et al. (2010) as a dashed line. The faint-end slope derived here agrees, within the uncertainty, with both Zwaan et al. (2003) and Martin et al.

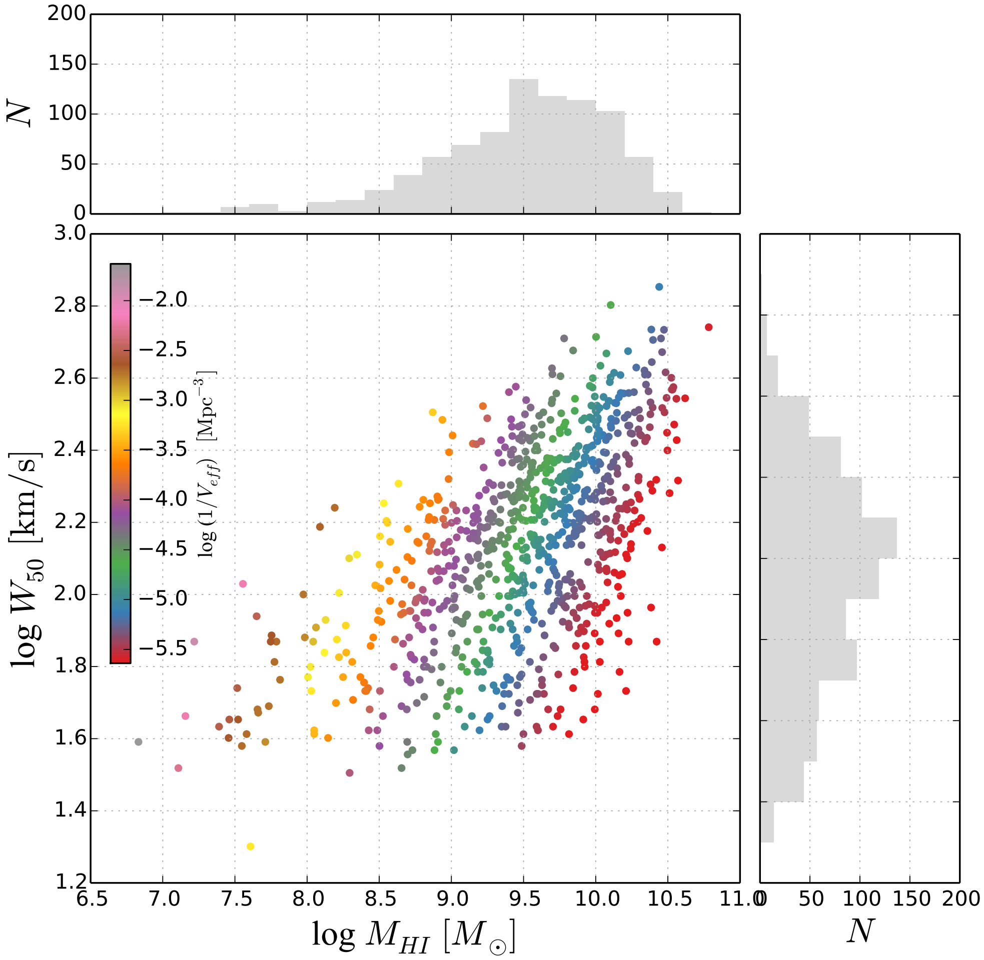

Figure 5.5: Galaxy density distribution in the $M_{HI} - W_{50}$ plane. Each dot presents a galaxy colour-coded by the reciprocal of the effective volume in which it can be found. This effective volume is calculated via the two-dimensional stepwise maximum likelihood method.

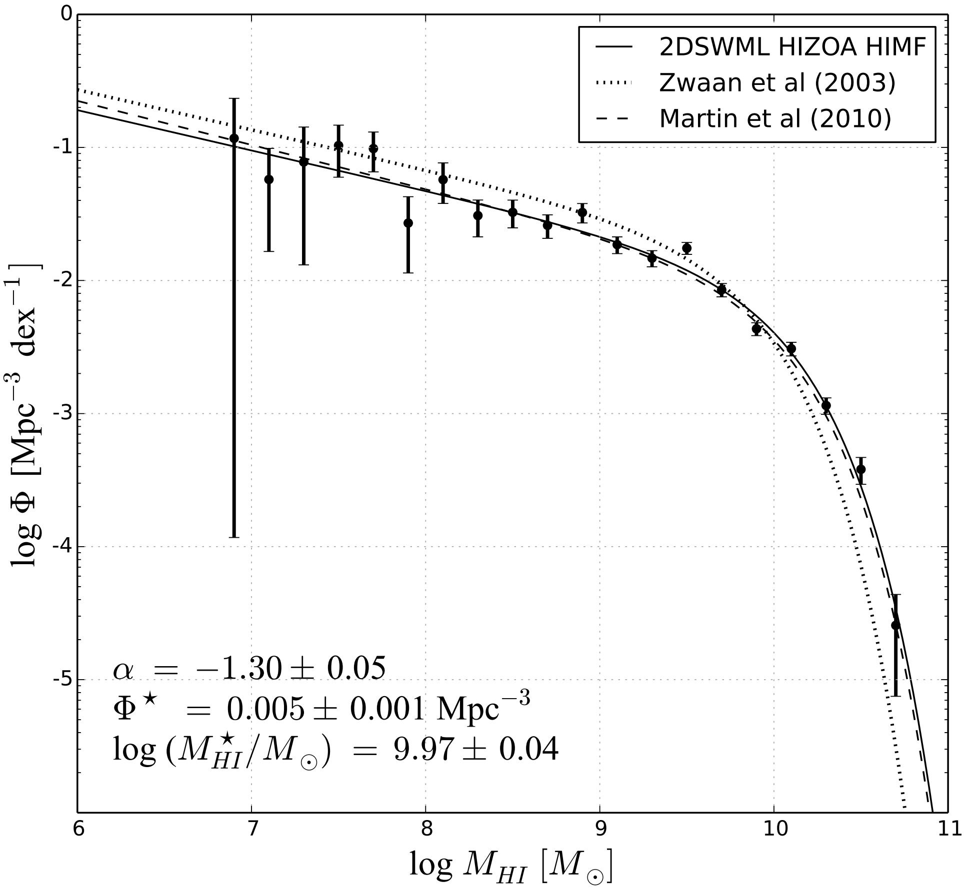

Figure 5.6: HIZOA H I mass function derived via the two-dimensional stepwise maximum likelihood method. For comparison, the H I mass function of HIPASS BGC (dotted line; Zwaan et al. 2003) and ALFALFA 40% (dashed line; Martin et al. 2010) are displayed as well.

(2010) but not with Zwaan et al. (2005) who derives a steeper slope. Again the knee of the H I mass function derived here agrees with the Martin et al. (2010) results but neither with Zwaan et al. (2003) nor Zwaan et al. (2005), see Fig. 5.6. This is because the HIZOA survey is $2-3$ times more sensitive than HIPASS (Staveley-Smith et al. 2016). The difference between $1/V_{max}$ and 2DSWML parameters confirms the Martin et al. (2010) results that the effect of the large-scale structure correction is very small on $\log(M^*_{HI}/M_\odot)$ but are 10% on α and 30% on ϕ^*.

For the rest of this Chapter we will restrict our analysis to the 2DSWML results.

Completeness

Completeness is the fraction of the target sample compared to all of the HIZOA galaxies that meet our selection criteria for a given flux bin. Figure 5.7 shows histograms of the initial sample (dark-gray) compared to the final observed sample (light-gray). We have only plotted galaxies above the HIZOA flux limit.

We calculate the fraction as a function of flux bin and fit a quadratic function to the points. We smooth our data before fitting the quadratic function using 3.5σ clipping procedure. Figure 5.8 shows the completeness as a function of flux density, with the best quadratic fit. This figure shows a perfect fit except for two points at 1.4 and 1.6 Jy km s^{-1} which are marked as outliers by the 3.5σ clipping fitting procedure.

Applying the Malmquist bias correction

For each galaxy we derived the probability distribution of the uncorrected logarithmic distance ratio assuming a normal distribution with 1σ of error. For each logarithmic distance we weight the probability by the reciprocal of the completeness integrated over the H I mass function, evaluated at the logarithmic distance in question. Then we fit a Gaussian to the new probability distribution to get the corrected logarithmic distance and the corrected logarithmic error. The corrected logarithmic distances and errors are shown in Figs. 5.9 & 5.10, respectively.

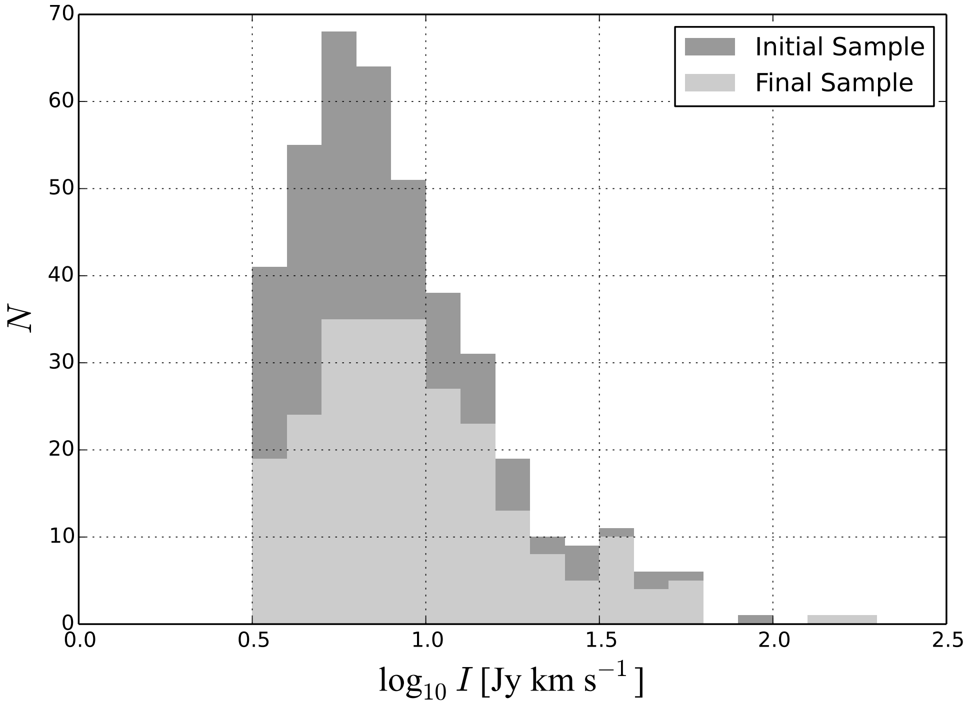

Figure 5.7: The fraction of the initial sample that is included in our final TF based distance sample for a given flux bin.

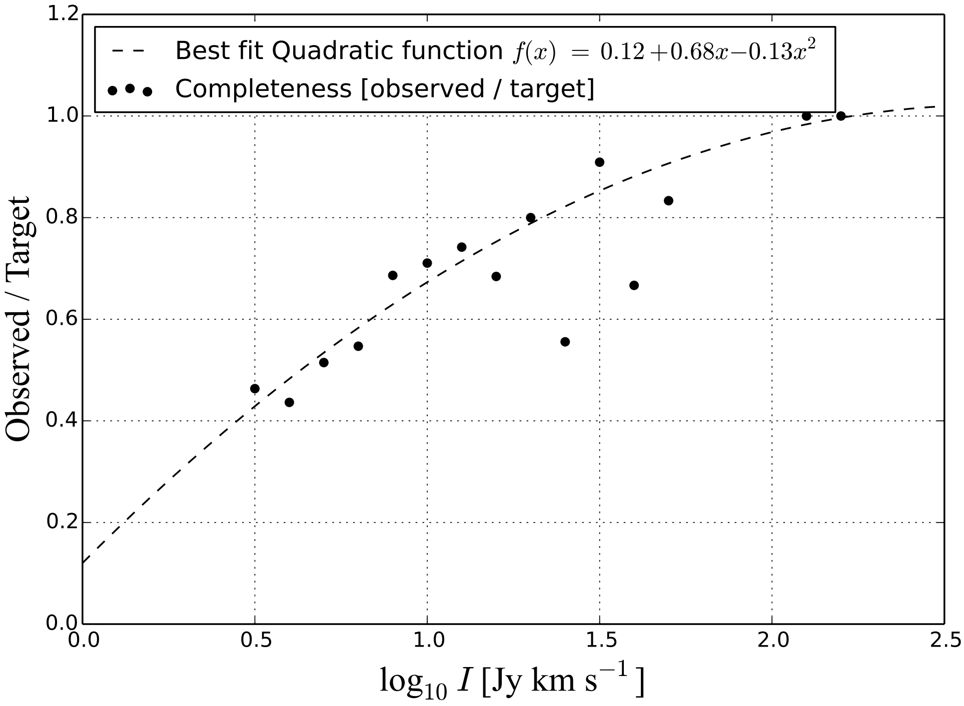

Figure 5.8: Quadratic function represent the completeness of our final TF sample. We smoothed our data before using 3.5σ clipping fitting procedure to avoid the outliers.

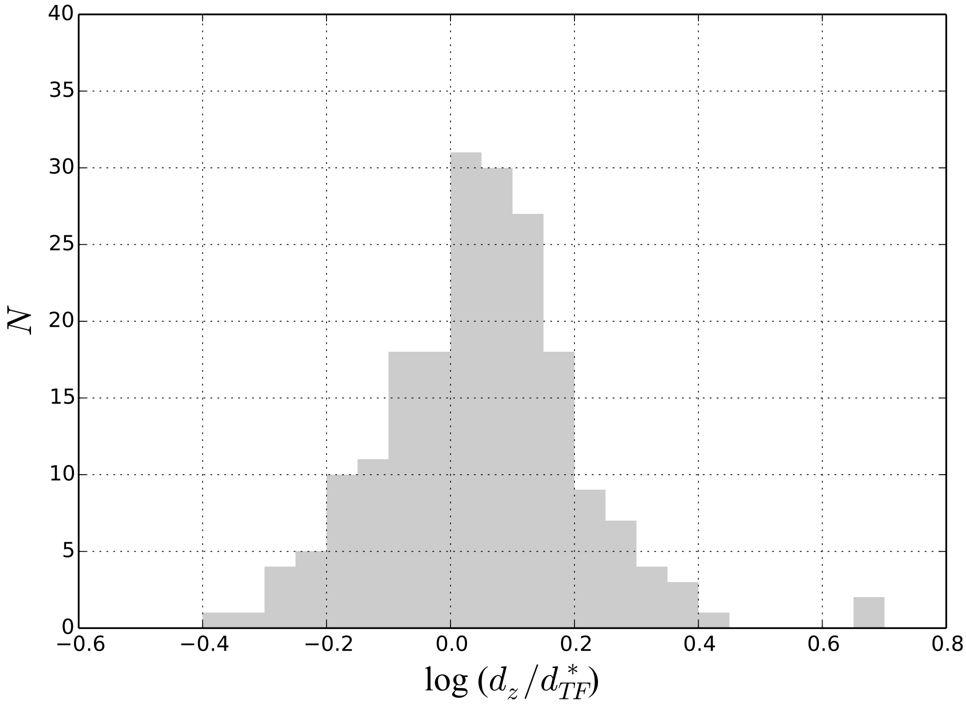

Figure 5.9: The distribution of the logarithmic distance ratio $\log(d_z/d^*_{TF})$ for the median of the three wavebands J, H, and K_s after applying the Malmquist bias correction.

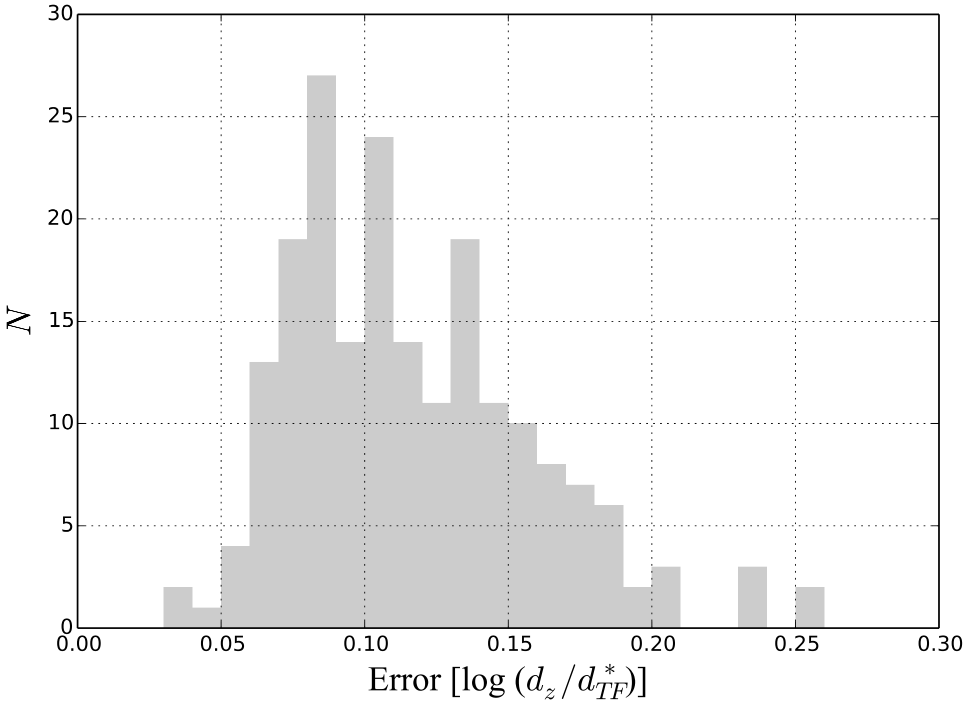

Figure 5.10: The distribution of the error of the logarithmic distance ratio $\log(d_z/d^*_{TF})$ by combining all three wavebands J, H, and K_s after applying the Malmquist bias correction.

The distribution of the logarithmic distance ratio $\log(d_z/d^*_{TF})$ is almost Gaussian in the range of $\log(d_z/d^*_{TF})$ from -0.4 to $+0.4$ with the peak centered at $\log(d_z/d^*_{TF}) = 0.1$. The 2MTF distribution is very similar to our results, but the peak of their Gaussian is at $\log(d_z/d^*_{TF}) = 0.0$. We interpret this shift in the peak as more positive peculiar velocities in our sample than the 2MTF sample. The errors of the logarithmic distance ratios in our sample is smaller than the 2MTF sample because of the new IRSF NIR observations, which are 2 mag deeper than 2MASS in the K_s-band and use more resolved IRSF images with a pixel scale of 0.45 arcsec pixel^{-1} compared to 2.0 arcsec pixel^{-1} for 2MASS images.

In the next Sections, we will use these distances and peculiar velocities to study the flow field in the ZOA and compare it with the predictions from reconstruction models.

5.5 Large-Scale Structures in the ZOA

Redshift surveys are a great tool to learn about the large-scale structure of galaxies and cosmography in the local Universe. They can be used to construct the density field from the 3-dimensional distribution of the galaxies. Most of these surveys are carried out by using optical spectra such as Center of Astrophysics redshift surveys CFA1 (de Lapparent et al. 1986), CFA2 (Huchra et al. 1999), *IRAS* PSCz (Saunders et al. 2000), 2dF (Colless et al. 2001), SDSS (Aihara et al. 2011), 6dFGS (Jones et al. 2009), and 2MRS (Huchra et al. 2012). The main difficulty for these surveys at low Galactic latitudes is the dust extinction and stellar density.

However, radio observations are not affected by dust or stellar confusion. We can use the H I 21-cm emission line for redshift surveys. The accuracy of these redshifts from radio surveys are much better than the redshifts extracted from optical surveys. The main limitation is that these radio surveys are limited to spiral galaxies because early-type galaxies are gas-poor.

In the last few decades, a number of systematic H I 21-cm redshift surveys have been carried out using large radio telescopes such as Parkes to carry out HIPASS (Barnes et al. 2001) and HIZOA (Staveley-Smith et al. 2016) surveys, Arecibo for ALFALFA (Giovanelli et al. 2005), and ALFAZOA (Henning et al.

2017), and Westerbork for WSRT-ZoA (Ramatsoku et al. 2016).

These redshift surveys are extremely useful to learn about the large-scale structures of galaxies in the nearby Universe and the density field. However, they can not differentiate the peculiar velocity of a galaxy from the total observed velocity. Therefore, peculiar velocity surveys are needed to obtain the velocity field, such as 6dFGSv (Springob et al. 2014), and 2MTF (Springob et al. 2016). Comparing the density field derived from the redshift surveys with the velocity field derived from the peculiar velocity surveys allows us to test the gravitational instability paradigm (Davis et al. 2011).

The peculiar velocity sample used in this thesis is based on the Parkes H I Zone of Avoidance (HIZOA) survey. This H I survey consists of three components, i.e. the main southern H I survey (HIZOA; Staveley-Smith et al. 2016), the Northern Extension (NE; Donley et al. 2005) and the Galactic Bulge (GB; Kraan-Korteweg et al. 2008). Staveley-Smith et al. (2016) combine these three surveys and discuss the most prominent LSS in connection to the features that cross the ZOA, such as the Puppis filament, the Great Attractor, and the Local Void. We will highlight these three structures and their importance to the dynamic cosmic web in the next subsections.

5.5.1 Puppis Region

We first describe the Puppis region, which is a crowded region and contains three main components, the Puppis 1 group, Puppis 2 cluster, and Puppis filament. Figure 5.11 shows a redshift wedge of the Puppis region (Staveley-Smith et al. 2016). In Fig. 5.11, we can see that Puppis region extend from $v_{LG} \sim 700$ to $v_{LG} \sim 4000$ km s^{-1} and from $l \sim 230°$ to $l \sim 260°$. The nearby Puppis group is called Puppis 1 (marked with the red circle) is at $v_{LG} \sim 700$ and $l \sim 245°$. The main Puppis cluster, called Puppis 2 (marked also with red circle), is at a slightly higher redshift of $v_{LG} \sim 1400$ km s^{-1} and almost the same longitude of $l \sim 245°$. The third component of the Puppis region is called Puppis filament and extend from $v_{LG} \sim 1500$ to $v_{LG} \sim 3500$. At 7000 km s^{-1} (not shown in the above figure) is the Puppis 3 cluster which is also prominent, and first described in Chamaraux & Masnou (2004).

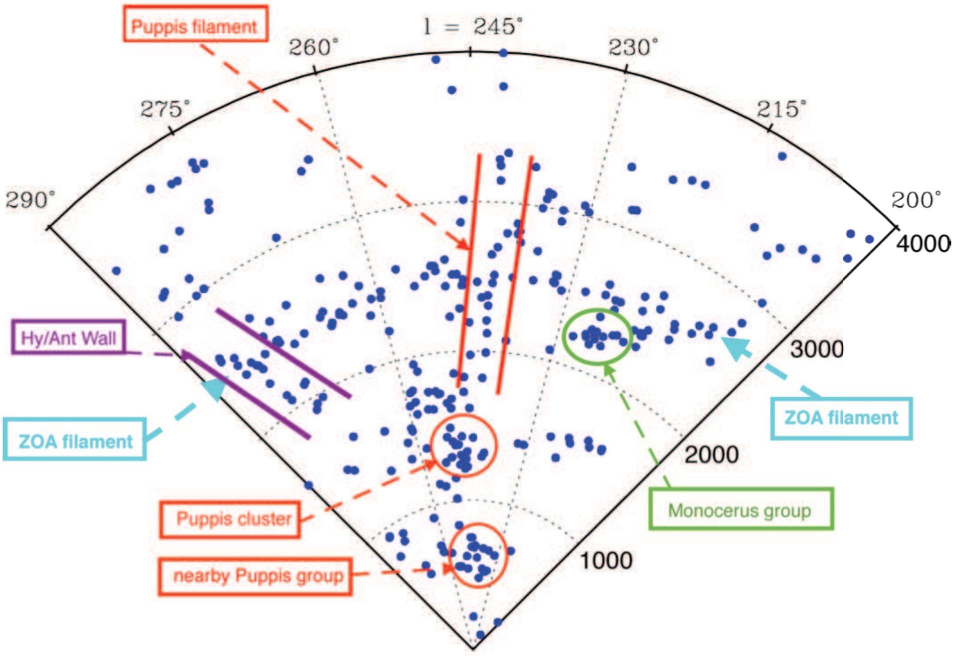

Figure 5.11: Redshift wedge of the Puppis region. The image is taken from Staveley-Smith et al. (2016)

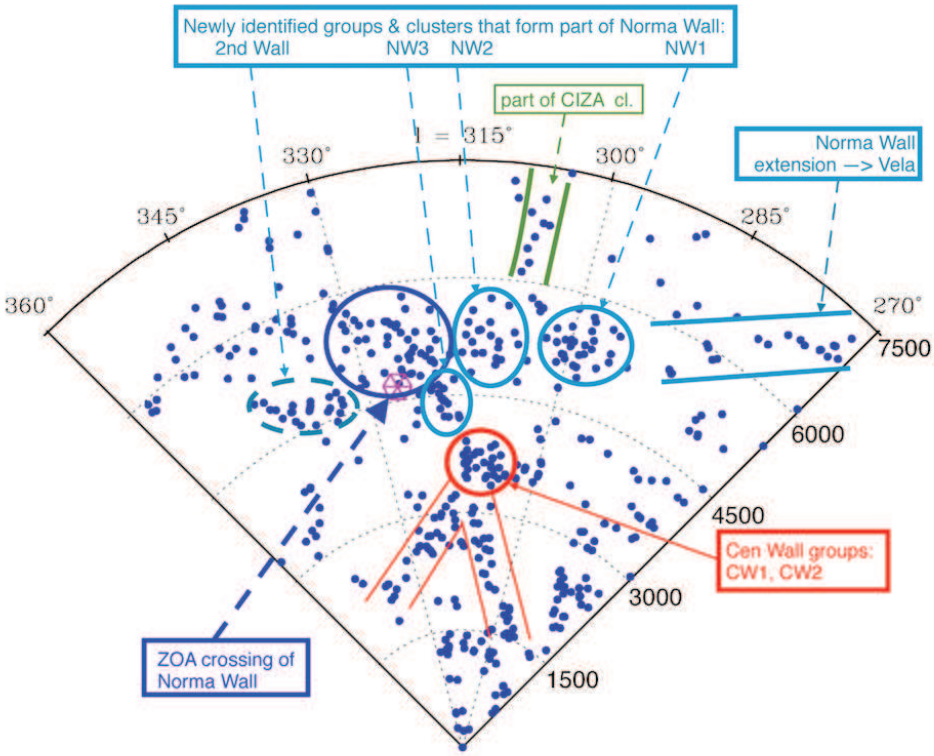

Figure 5.12: Redshift wedge of the Great Attractor region. The image is taken from Staveley-Smith et al. (2016)

5.5.2 Great Attractor Region

The second structure in the HIZOA survey (Staveley-Smith et al. 2016) is the Great Attractor Wall crossing. This region dominates both the HIZOA redshift survey and the peculiar velocity sample used in this thesis (see Fig. 3.2). Figure 5.12 presents the redshift wedge of the Great Attractor region (Staveley-Smith et al. 2016). It shows that the Great Attractor region extends from $v_{LG} \sim 1500$ to $v_{LG} \sim 7500$ km s^{-1} and from $l \sim 270°$ to $l \sim 330°$. This figure also shows the Norma Wall extension towards Vela near $l \sim 270°$.

5.5.3 Local Void

The third large-scale structure is the Local Void. The LV extends from $l \sim 330°$ to $l \sim 45°$ and spreads over a volume out to $v_{LG} \lesssim 6000$ (Tully & Fisher 1987, Donley et al. 2005, Kraan-Korteweg et al. 2008). The southern part of the LV lies within the main HIZOA survey (Staveley-Smith et al. 2016), whereas the northern part of is covered by the northern extension (Donley et al. 2005). The Galactic bulge extension is conducted because the LV stretches to Galactic latitude of about ±40° (Kraan-Korteweg et al. 2008; Kraan-Korteweg et al. in prep.). This will improve our knowledge of the LV and of the Sagittarius Void (Fairall 1998) at $l \sim 350^\circ$, $b \sim 0^\circ$, and $cz \sim 4500$ km s^{-1}, and the Ophiuchus Cluster (Hasegawa et al. 2000) at $l \sim 0^\circ$, $b \sim 9^\circ$, and $cz \sim 9000$ km s^{-1}.

5.6 Velocity Field in the ZoA

Following the description of the three main structures that dominate the southern ZOA. We will now explore the velocity field in and around these three LSS.

Figure 5.13 shows the distribution of our ZOA TF sample in Galactic coordinates which is about 33% of the total HIZOA galaxy sample. Each dot in the top-panel represents a galaxy colour-coded by its redshift cz in km s^{-1} units. Galaxies in the bottom panel are colour-coded by its logarithmic distance ratio $\log(d_z/d^*_{TF})$. The top-panel also shows the approximate positions and velocities of Puppis, GA, and LV as white rectangles. In the next subsections, we will discuss the motion of galaxies inside and around each one of these large-scale structure features separately.

5.6.1 Puppis Region

The Puppis region extends from $l \sim 230^\circ$ to $l \sim 260^\circ$ and contains galaxies with radial velocity up to $cz \leq 4000$ km s^{-1}. The bottom panel of Fig. 5.13 shows that galaxies in the Puppis region are having a combination of both negative and positive peculiar velocities. Most of the darkblue dots (≤ 3000 km s^{-1}) in the top panel have weak negative peculiar velocities in the bottom-panel. However, most of the lightblue to red dots (≥ 3000 km s^{-1}), further away, have positive peculiar velocities. This may be an indication of outflow from the Puppis region and will be investigated further using a smoothed version of the velocity field.

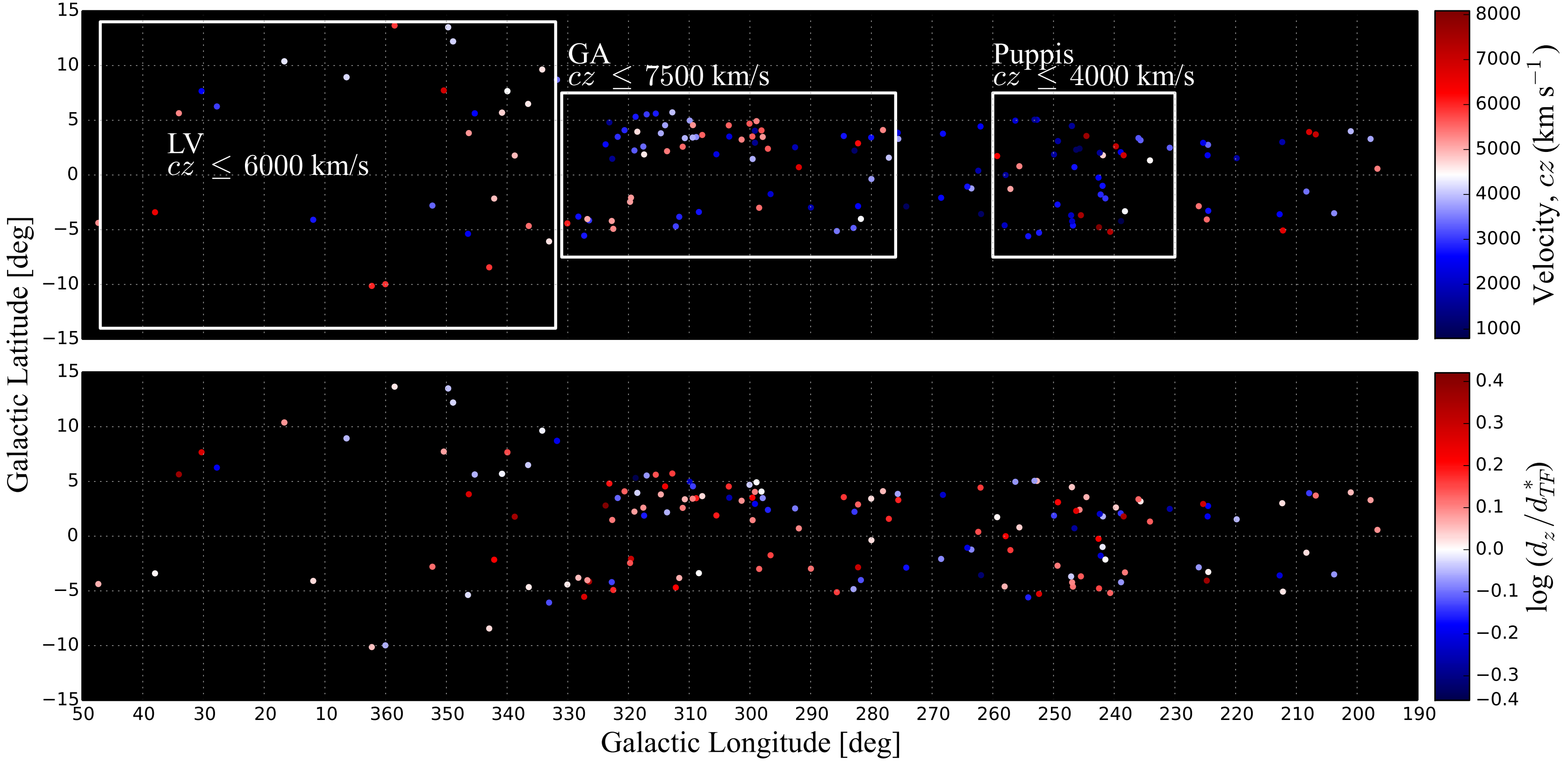

Figure 5.13: Distribution of our ZOA TF galaxies in Galactic latitude (l) and longitude (b). Galaxies are colour-coded by redshift cz in the top panel and by the logarithmic distance ratio $\log(d_z/d^*_{TF})$ in the bottom panel. The approximate positions of Puppis, GA, and LV are marked with white rectangles.

5.6.2 Great Attractor Region

The Great Attractor region spreads over large area from $l \sim 270°$ to $l \sim 330°$ and expands to redshifts of $cz \leq 7500$ km s^{-1}. Galaxies in the GA region dominate our ZOA peculiar velocity sample. Almost all galaxies on the nearby side of the GA (blue galaxies in the top panel) have positive peculiar velocities (see bottom panel). This is a clear indication of infall into the GA region. This infall was previously seen by several authors and led to the discovery of the GA itself (Lynden-Bell et al. 1988). Galaxies on the far side of the GA (red galaxies in the top panel) have either zero or very weak negative peculiar velocities (see the concentration at $l = 300°$ and $b = 4°$). This an indication of the back side boundary of the GA region.

5.6.3 Local Void

The Local Void ranges from $l \sim 330°$ to $l \sim 45°$ over a range of redshift of $cz \leq 6000$. Most of the galaxies in the bottom-panel in this region are colour-coded with either white or lightblue. This implies that they have either zero or very weak negative peculiar velocities, i.e. a slow outflow of Local Void galaxies. This result confirms the draining of the Local Void by Rizzi et al. (2017) which uses the luminosity of stars at the tip of the red giant to determine the distances of two galaxies in the LV. They found that these two galaxies are moving away from the center of the LV which is in line with our result.

5.7 Smoothed Flow Field in the ZOA

For the discussion in this section, we transform the Galactic longitude and latitude (l, b) and redshift to the Super Galactic Cartesian coordinates (SGX, SGY, SGZ) as defined in de Vaucouleurs et al. (1976) and Tully (1988). The main reason for working in this coordinate system is that it allows a comparison of our results the 2MTF observations (Springob et al. 2016), 2MRS (Erdoğdu et al. 2006b), and PSCz (Branchini et al. 1999) reconstructions. Table 5.2 lists the most notable large-scale structures in/near our sample. We used the approximate center of each LSS to calculate their supergalactic Cartesian coordinates

Table 5.2: The approximate coordinates of the most notable large-scale structures in/near our sample

Name	l °	b °	cz (km s^{-1})	SGX h^{-1} Mpc	SGY h^{-1} Mpc	SGZ h^{-1} Mpc
Hydra cluster	270	26	3500	−28	23	−28
Puppis region	245	0	2500	−10	3	−31
Norma cluster	325	−7	4707	−61	−9	8

(SGX, SGY, SGZ).

We divide our sample into three slices of SGZ to distinguish between the motion of galaxies around the three structures in the southern ZOA. Figures 5.14, 5.15, and 5.16 present the velocity field in slices of $SGZ < -20h^{-1}$ Mpc, $-20 < SGZ < 20h^{-1}$ Mpc, and $SGZ > 20h^{-1}$ Mpc, respectively. In all three figures the velocity field is given in logarithmic distance ratios unit $\log(d_z/d^*_{TF})$. Red represents positive peculiar velocity and blue represents negative peculiar velocity. These figures display the velocity field smoothed with a Gaussian kernel of radius 4 h^{-1} Mpc as in Carrick et al. (2015) and Springob et al. (2016), in the logarithmic distance ratios unit $\log(d_z/d^*_{TF})$.

The top panel of Fig. 5.14 shows the amplitude of the velocity field where the colour-bar on the right-hand side indicates the scale of the peculiar velocity. The bottom panel is a duplication of the top panel with a shallower colour for easier display of the most prominent LSS. Figure 5.14 displays clear indication of positive peculiar velocity towards negative SGX and positive SGY hence in the direction of the Hydra cluster (see the red arrow). In contrast, we see a lot of negative peculiar velocities in the Puppis region as indicated in the bottom panel by the blue arrow.

Figure 5.15 shows the velocity field in the $-20 < SGZ < 20h^{-1}$ Mpc slice which contains the Norma cluster, the richest cluster in the Great Attractor region. Very strong infall towards negative SGX and SGY is observed, thus in the direction of Norma (see bottom panel). This infall does not stop at Norma but continues in the same direction towards negative SGX and SGY and maybe an indication of a much bigger attractor further away as shown in Figure 5.15 and also Figure 5.13. On the positive side of the SGY plane we see more negative peculiar velocities, suggestive of a back-side infall from

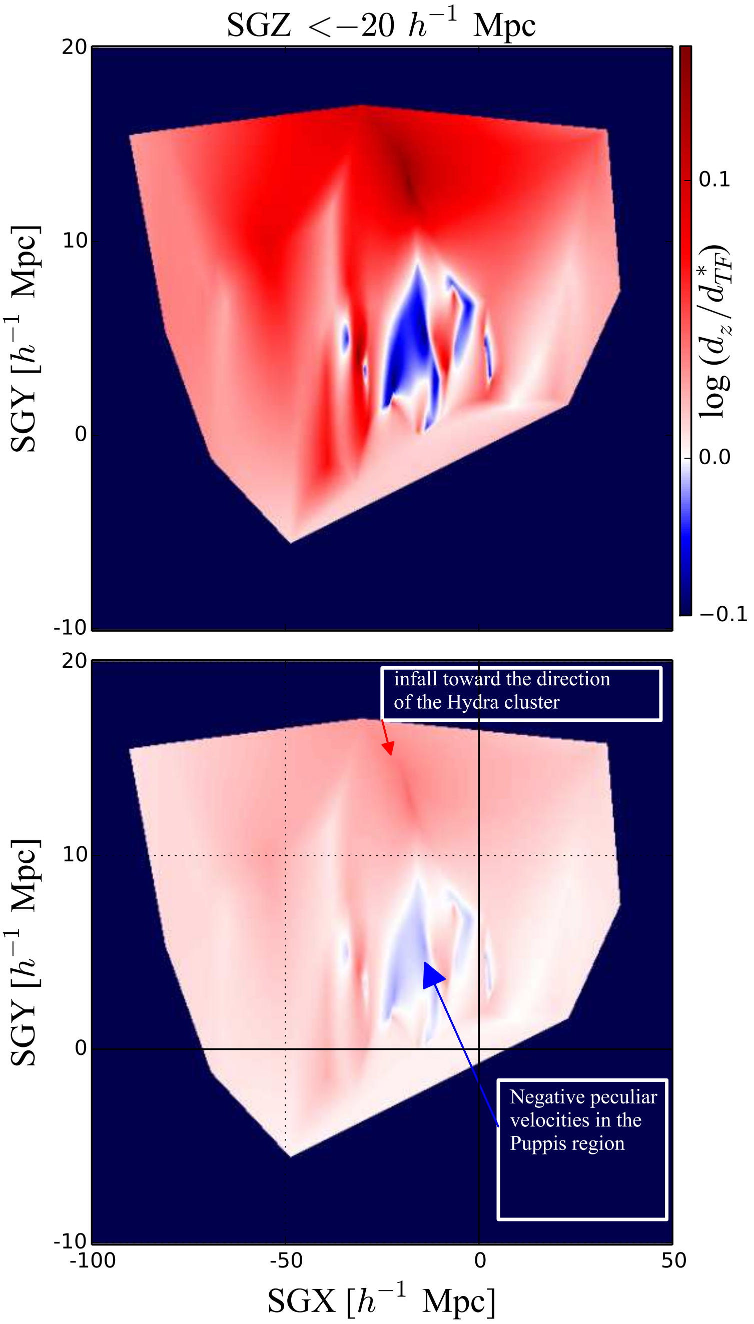

Figure 5.14: The velocity field (smoothed with a Gaussian kernel of radius 4 h^{-1} Mpc) in units of logarithmic distance ratio $\log(d_z/d_{TF}^*)$ of galaxies in the $SGZ < -20h^{-1}$ Mpc slice. Red represents positive peculiar velocity, whereas blue represents negative peculiar velocity. There is a clear indication of positive peculiar velocity towards the direction of the Hydra cluster. There are a lot of negative peculiar velocities in the Puppis region, which is an indication of an outflow. Note the different ranges for x-axis and y-axis, this is because we survey only the ZOA. See also Figure 5.17 for a better visualization.

the far side of the GA on the positive side of the Galactic Plane. This is also clearly seen in Fig. 5.13. Galaxies with the highest redshift in the GA region (see top panel above the GP) have negative peculiar velocities in the bottom panel.

Figure 5.16 shows the velocity field in the $SGZ > 20h^{-1}$ Mpc slice. In this slice we see strong positive peculiar velocities in all directions but no negative peculiar velocities.

Although our survey covers a small area, we can compare the resulting ZOA flow field with other velocity field observations and reconstructions. Figure 4 by Springob et al. (2016) (reproduced here as the bottom panels of Fig. 5.17) combined the velocity field as derived by 2MTF (Hong et al. 2014), the 2MASS Redshift Survey (2MRS; Erdoğdu et al. 2006b), and the IRAS Point Source Catalog Redshift Survey (PSCz; Branchini et al. 1999) in three slices of SGZ similar to Figs. 5.14, 5.15, and 5.16. For direct comparison, we reproduced the ZOA slices using the exact same scale used by Springob et al. (2016) and added them at the top of of their figure.

The left-hand slice (Fig. 5.17; $SGZ < -20h^{-1}$ Mpc) agrees with the 2MTF observations which is the second panel of Fig. 5.17. It does not agree with either the 2MRS or PSCs reconstructions. In the middle slice (Fig. 5.17; $-20 < SGZ < 20h^{-1}$ Mpc), the results of the ZOA, 2MTF observations, 2MRS, and PSCz reconstructions all agree on the infall towards Norma. The back-side infall into the GA is only identified in this work. In the right-hand slice (Fig. 5.17; $SGZ > 20h^{-1}$ Mpc), our flows agree with the 2MTF observations, 2MRS, and PSCz reconstructions only at $SGX < -50h^{-1}$ Mpc. However, there are clear disagreements at the center of the $SGX-SGY$ plane with the three of them. This disagreement is because these three studies do not have any data in the ZOA. The 2MRS and PSCz reconstructions used some extrapolation to fill in the ZOA.

The ZOA flow fields support the notion that extrapolations across the ZOA are not sufficient in acquiring a reliable map of the mass density distribution hidden behind the Milky Way.

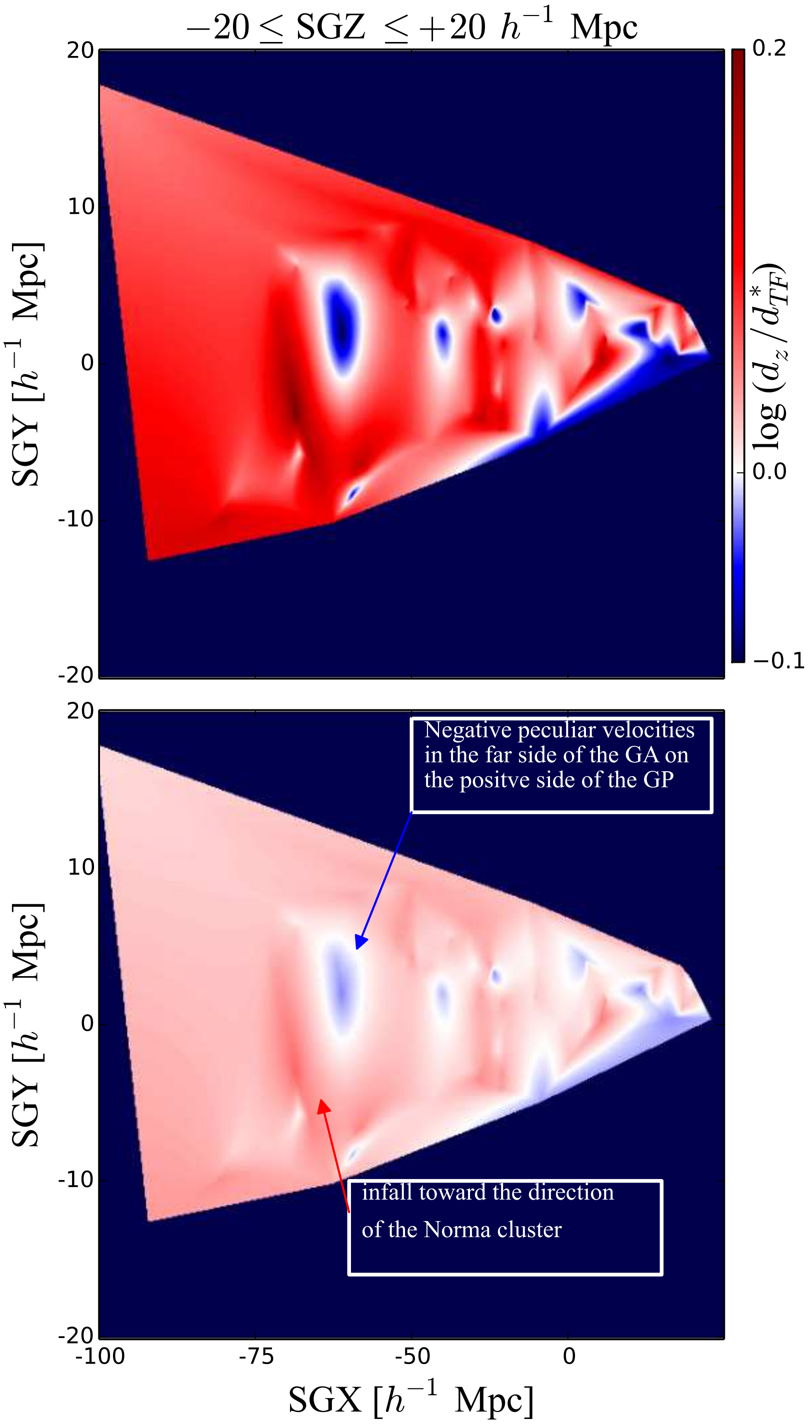

Figure 5.15: The velocity field in the logarithmic distance ratios unit $\log(d_z/d^*_{TF})$ of galaxies in the $20 < SGZ < -20h^{-1}$ Mpc slice. Smoothing, and colours are the same as in Fig. 5.14. There is a strong positive peculiar velocities toward the direction of the Norma cluster and beyond. Also there is a back side infall from the far side of the GA. Note the different ranges for x-axis and y-axis, this is because we survey only the ZOA. See also Figure 5.17 for a better visualization.

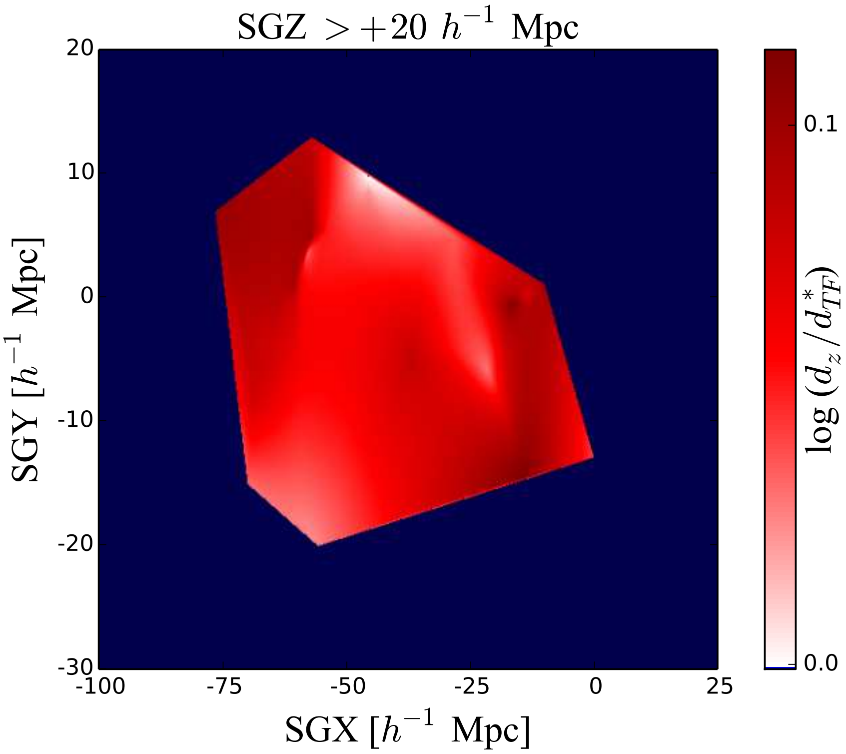

Figure 5.16: The velocity field in the logarithmic distance ratios unit $\log(d_z/d^*_{TF})$ of galaxies in the $SGZ > 20h^{-1}$ Mpc slice. Smoothing, and colours are the same as in Fig. 5.14. Strong positive peculiar velocities in all direction are shown. Note the different ranges for x-axis and y-axis, this is because we survey only the ZOA. See also Figure 5.17 for a better visualization.

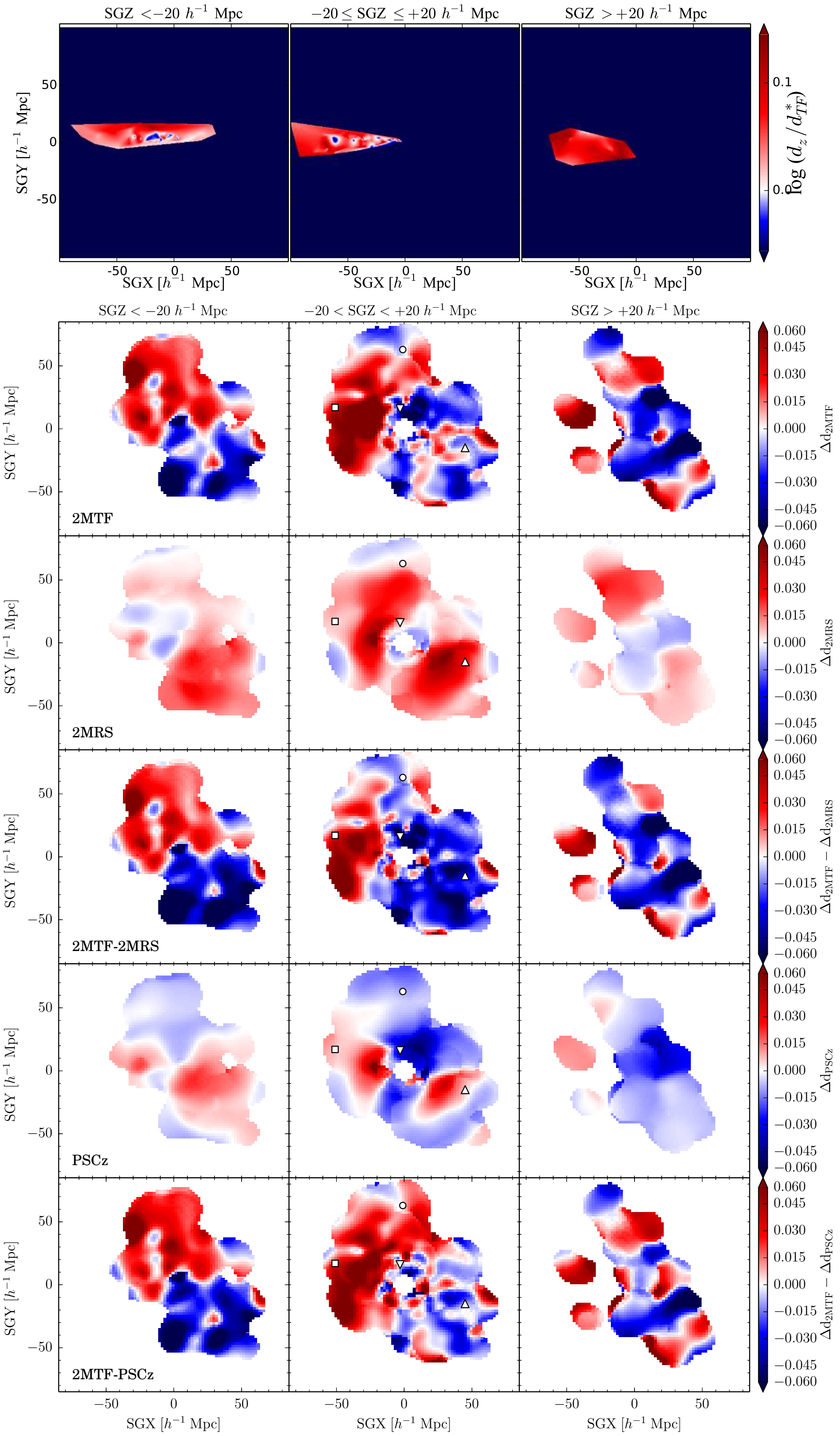

Figure 5.17: The velocity field as derived by this thesis, 2MTF, 2MRS, and PSCz in three slices of SGZ. The bottom panel is taken from Springob et al. (2016).

5.8 Summary

In this Chapter we measured the distances and peculiar velocities of inclined spiral galaxies hidden behind our own Milky Way. We reviewed the calibrated Tully-Fisher relations in the J, H, and K_s bands. Then we presented our method on how to prepare and correct the raw data to be used in the calculation of the distances and peculiar velocities in the Zone of Avoidance. In the process of calculating the TF based distances and peculiar velocities we choose to work with the logarithmic distance ratio instead of the linear peculiar velocities because the distance errors are log-normal. We also worked with redshift space rather than real space to avoid the inhomogeneous Malmquist bias. However, to correct for the homogeneous Malmquist bias we constructed H I mass function using both $1/V_{max}$ and the two-dimensional stepwise maximum likelihood methods. All galaxies in the HIZOA survey that meet our selection criteria ($N = 873$ galaxies) are included in the derivation of this H I mass function. The final parameters of the H I mass function are $\alpha = -1.30 \pm 0.05$, $\log(M^*_{HI}/M_\odot) = 9.97 \pm 0.04$, and $\phi^* = (5.2 \pm 0.8) \times 10^{-3}$ Mpc^{-3}. Comparisons of these parameters with values from the literature were performed. We found that the faint-end slope derived here agrees, within the uncertainty, with both HIPASS BGC and ALFALFA. However, the knee of the H I mass function derived here agrees with the ALFALFA H I mass function better than with the HIPASS H I mass function. We also derived the completeness as the fraction of the initial sample included into our final sample for a given flux bin. We corrected the logarithmic distance ratios $\log(d_z/d^*_{TF})$ for Malmquist bias using both the HIZOA H I mass function and the completeness function. Comparing the distribution of the logarithmic distance ratio $\log(d_z/d^*_{TF})$ of our sample with the 2MTF sample shows that we have more positive peculiar velocities in our sample than the 2MTF. The associated uncertainties are smaller than 2MTF due to the deeper and more resolved IRSF NIR images compared to the 2MASS.

We used these corrected logarithmic distance ratios to describe the velocity field in and around the three prominent LSS features in the southern ZOA.

We first showed the position and the extent of these three LSS features as in the HIZOA redshift surveys. We then described the peculiar velocities in and around these three features.

In the Puppis region, we see a combination of both negative and positive peculiar velocities. Galaxies of the nearby side of this region tend to have negative peculiar velocities, whereas galaxies on the far side of the Puppis region mostly have positive peculiar velocities. This is an indication that galaxies are moving away from the center of the Puppis region.

There is a strong infall towards the Great Attractor. Most of the galaxies have positive peculiar velocities. Few galaxies at the very far end of the GA velocity range ($cz \sim 7500$) have zero or weak negative peculiar velocities. This may indicate the far back-side boundary of the GA region.

Most of the galaxies in the LV have zero or negative peculiar velocities, which implies that the LV is either expanding or draining. This result confirms the recent result by Rizzi et al. (2017) which shows that two galaxies are moving away from the center of the LV.

We also derived the velocity field in slices of the Super Galactic Cartesian coordinates SGZ to compare our results with Springob et al. (2014; 2016) who use that same coordinates system. In each slice of SGZ we tested the motion of galaxies around the approximate positions of features of large scale structures.

We found clear positive peculiar velocities toward the direction of Hydra cluster. We also found strong positive peculiar velocities toward the direction of the Norma cluster, while the galaxies in the Puppis region have negative peculiar velocities.

We compared our velocity field to the 2MTF observations (Hong et al. 2014, Springob et al. 2016), and the 2MRS (Erdoğdu et al. 2006b) and the PSCz (Branchini et al. 1999) reconstructions. The velocity field derived in this thesis agrees, at low redshift, with the 2MTF observations but disagrees with both the 2MRS, and the PSCz reconstructions. However, all four velocity fields agree on the observed infall into the Norma cluster. At high redshift, our results disagree with 2MTF, 2MRS, and PSCz.

Chapter 6

Conclusion

6.1 Summary

This PhD thesis uses the NIR Tully-Fisher relation, H I 21-cm narrow-band observations, and deep NIR imaging to explore the flow field in the southern Zone of Avoidance. The galaxy sample we use is based on the blind systematic deep Parkes H I Zone of Avoidance survey.

We used the isophotal instead of total magnitude to re-construct the Tully-Fisher (TF) template relations using 888 spiral galaxies. This is the same sample used by the 2MTF team to calibrate the total TF relation. We used the isophotal and not total magnitudes because they can be measured easily in the ZOA and they are more consistent between different surveys than the total magnitudes. The scatter of the isophotal and total TF relations are almost identical for large and fast rotator galaxies. However, for dwarf and slow rotator galaxies the scatter of the isophotal TF relation is smaller than the total TF relations.

We showed that galaxies appear rounder with increasing obscuration level using both real data and simulated images. To correct for this effect, we derived a model that can reproduce the actual axial ratio from the observed one up to extinction level of $A_V \sim 11$ mag

We presented new H I profiles and velocity widths for a selected sample of inclined spiral galaxies from the HIZOA. These galaxies define a sample for use in determining the peculiar velocities using the near-infrared TF relation. This was achieved by re-observing these galaxies using the narrow band on

Parkes radio telescope to obtain better velocity resolution. The average signal-to-noise ratio for this H I survey was 14.7 which is adequate for TF studies. Five different types of line-widths are presented to select the most robust one. The Pearson's sample correlation coefficient was used to quantify the correlation between all derived linewidths. Conversion equations between these five linewidths were derived using a Bayesian mixture model to avoid any bias toward the outliers and to allow combination of data from different surveys.

We presented deep NIR (J, H, and K_s bands) images of all HIZOA detections. Observations were conducted using the Japanese Infrared Survey Facility (IRSF), a 1.4-m telescope situated at the South African Astronomical Observatory site in Sutherland and resulted in over a thousand galaxies. The average K_s-band seeing, sky background, and isophotal magnitude errors for the survey are 1.38 arcsec, 20.1 mag, and ~ 0.02 mag, respectively. We compared our results with counterparts from the 2MASX and UKIDSS GPS surveys. We found good agreement between the K_s-band K_{s20} fiducial elliptical aperture magnitude presented in our catalogue and the same parameter reported in the 2MASX catalogue. We detect only small deviations for both faint galaxies (> 14 mag) and bright galaxies (< 9 mag). The deviation for bright galaxies is due to the difference of the pixel scale between IRSF and 2MASX instruments. While the deviation for the faint galaxies is a bias due to the completeness limit of 2MASX. We also found good agreement between the K_s-band K_{s20} fiducial elliptical aperture magnitudes measured from the IRSF data and the same parameter measured from the UKIDSS GPS data. This confirms that the IRSF images are of equal quality to the UKIDSS GPS images, which are one magnitude deeper.

We used these NIR and H I data with the recently calibrated TF relation to derive distances and peculiar velocities for inclined spiral galaxies in the southern ZOA. We chose to work with the redshift space instead of real space to avoid having to correct for the inhomogeneous Malmquist bias. However, to correct for the homogeneous Malmquist bias we constructed H I mass function using both $1/V_{max}$ and the two-dimensional stepwise maximum likelihood methods. All galaxies in the HIZOA survey that meet our selection criteria are included in the derivation of this H I mass function. The final parameters of the H I mass function are $\alpha = -1.30 \pm 0.05$, $\log(M^*_{HI}/M_\odot) = 9.97 \pm 0.04$, and $\phi^* = (5.2 \pm 0.8) \times 10^{-3}$ Mpc^{-3}. Comparing these parameters with values from the literature, we found that the faint end slope derived here agrees with both HIPASS BGC and ALFALFA. However, the knee of the H I mass function agrees with the ALFALFA results but not with the HIPASS results. We have presented the compilation of TF based distances and peculiar velocities in the southern ZOA after applying all corrections. We mapped the velocity field to describe the motion of galaxies around the major large-scale structures, and the cosmography out to redshift $z \sim 0.03$. We found a clear positive peculiar velocities toward the direction of Hydra cluster and Shapley Supercluster. We also found strong positive peculiar velocities toward the direction and beyond Norma cluster. However, negative peculiar velocities were found in the Puppis region. We compared our velocity field to the 2MTF observations, 2MRS, and PSCz reconstructions.

These distances and peculiar velocities will be used in the future with the data from the northern ZOA and data from the 2MASS Tully-Fisher survey to provide the first all sky TF based distances and peculiar velocities survey.

6.2 Future work

6.2.1 All-sky peculiar velocity survey, 2MTF+

In this thesis, we showed the feasibility to extend the peculiar velocity analysis and provide the first ever truly all-sky peculiar velocity survey by:

1. Constructing TF template relation that works in and out of the ZOA (Said et al. 2015)

2. Derive transformation relations between five types of line-widths to include H I observations from different surveys without applying any corrections (Said et al. 2016)

3. Build a reduction pipeline for NIR observations, both IRSF and UKIDSS data (Said et al. 2016)

We will make this NIR reduction pipe-line more general to include the two ESO public surveys, VISTA Variables in the Via Lactea (VVV) and

VISTA Hemisphere Survey (VHS) to derive the most accurate photometry to all bright-inclined galaxies with H I detection in the southern hemisphere. In the northern hemisphere, we will use UKIDSS data.

In 2009, Prof. Kraan-Korteweg and collaborators started an observing programme to obtain H I redshifts for all bright galaxies in the 2MASS Extended Source Catalog (2MASX; Jarrett et al. 2000) with $K_s^o < 11.25$ mag in the ZoA ($|b| < 10°$) which do not have any previous redshift determinations (van Driel et al. 2009). A new collaboration led by Prof. Kraan-Korteweg started last year to obtain deeper and higher velocity-resolution H I data. These narrow-band observations started this year using the Nançay Radio Telescope, France.

The next step is to extend this work by combining it with the 2MTF survey and provide the first ever truly all-sky peculiar velocity survey. We will use this survey to compare the dipole of the CMB which is a Doppler effect due to the Sun's motion (Hinshaw et al. 2009, Planck Collaboration et al. 2014b) with the LG peculiar velocity induced from our sample. Such analysis used to be limited due to the lack of observations in the ZoA (Loeb & Narayan 2008).

6.2.2 *WISE* Tully-Fisher relation

We would like to benefit from the large sample used to derive the TF template relation in Said et al. (2015) to re-calibrate the TF template relation using the far IR WISE *W1* and *W2* bands. Deriving WISE *W1* and *W2* TF templates in a way consistent with the NIR J, H, and K_s bands TF templates would provide a unique five bands TF relations. These relations will be used to understand the physical sources of this scatter in the TF relation.

Such a study will help us understand the models of galaxy formation because, while *WISE* is more sensitive to star forming regions, NIR is more sensitive to the old stellar population: *i.e.* through NIR we see the galaxy in the present and through *WISE* we see it in the future. This will also explain the systematic deviation of small dwarf galaxies from the TF relation (e.g., Are these dwarf galaxies a result of a different formation mechanism? Or are they just smaller versions of large galaxies?)

6.2.3 Environmental dependence of the H I Mass Function

Part of of this thesis is to deal with the Malmquist bias which is a consequence of two effects: (1) volume effect and (2) selection effect. To correct for these effects, one should use either luminosity function or H I mass function, depending on the parent survey. In this thesis we use the H I mass function because our sample is derived from the HIZOA survey (Staveley-Smith et al. 2016). We derived the H I mass function for all galaxies in the H I survey with both $1/V_{max}$ and the two-dimensional stepwise maximum likelihood (2DSWML) methods. During this process we came a cross the question of the dependence of the H I mass function on the environmental density. For example, Zwaan et al. (2005) used the HIPASS catalogue (Meyer et al. 2004) to test whether the shape of the H I mass function depends on local galaxy density. They found that the slope of the H I mass function becomes steeper toward higher density regions. In contrast, Jones et al. (2016) used a much larger sample from the ALFALFA 70% catalogue (Giovanelli et al. 2005, Haynes et al. 2011) and found the exact opposite result. They found no significant change in the slope but instead they found that the knee of the H I mass function to be dependent on environment.

To address this question we would like to derive the H I mass function for specific regions like GA or Local Void and compare, which is our next step by using the HIZOA survey (Staveley-Smith et al. 2016).

Bibliography

Aaronson M., Bothun G., Mould J., Huchra J., Schommer R. A., Cornell M. E., 1986, ApJ , 302, 536

Aaronson M., Huchra J., Mould J., 1979, ApJ , 229, 1

Aihara H. et al., 2011, ApJS , 193, 29

Amôres E. B. et al., 2012, AJ , 144, 127

Andreon S., 2002, A&A, 382, 495

Avila-Reese V., Firmani C., Hernández X., 1998, ApJ , 505, 37

Balkowski C., Bottinelli L., Chamaraux P., Gouguenheim L., Heidmann J., 1974, A&A, 34, 43

Barnes D. G. et al., 2001, MNRAS , 322, 486

Bernstein G. M., Guhathakurta P., Raychaudhury S., Giovanelli R., Haynes M. P., Herter T., Vogt N. P., 1994, AJ , 107, 1962

Bilicki M., Chodorowski M., Jarrett T., Mamon G. A., 2011, ApJ , 741, 31

Bouché N., Schneider S. E., 2000, in Kraan-Korteweg R. C., Henning P. A., Andernach H., eds, Astronomical Society of the Pacific Conference Series Vol. 218, Mapping the Hidden Universe: The Universe behind the Mily Way - The Universe in HI. p. 111

Branchini E. et al., 1999, MNRAS , 308, 1

Burstein D., Haynes M. P., Faber M., 1991, Nature , 353, 515

Cameron L. M., 1990, A&A, 233, 16

Campbell L. A. et al., 2014, MNRAS , 443, 1231

Cappellari M. et al., 2013, MNRAS , 432, 1862

Cardelli J. A., Clayton G. C., Mathis J. S., 1989, ApJ , 345, 245

Carrick J., Turnbull S. J., Lavaux G., Hudson M. J., 2015, MNRAS , 450, 317

Catinella B., Haynes M. P., Giovanelli R., 2005, AJ , 130, 1037

Chamaraux P., Masnou J.-L., 2004, MNRAS , 347, 541

Colless M. et al., 2001, MNRAS , 328, 1039

Colless M., Saglia R. P., Burstein D., Davies R. L., McMahan R. K., Wegner G., 2001, MNRAS , 321, 277

Courteau S., Dutton A. A., van den Bosch F. C., MacArthur L. A., Dekel A., McIntosh D. H., Dale D. A., 2007, ApJ , 671, 203

Courteau S., Faber S. M., Dressler A., Willick J. A., 1993, ApJL , 412, L51

Courtois H. M., Tully R. B., 2015, MNRAS , 447, 1531

Courtois H. M., Tully R. B., Fisher J. R., Bonhomme N., Zavodny M., Barnes A., 2009, AJ , 138, 1938

Courtois H. M., Tully R. B., Héraudeau P., 2011, MNRAS , 415, 1935

Courtois H. M., Tully R. B., Makarov D. I., Mitronova S., Koribalski B., Karachentsev I. D., Fisher J. R., 2011, MNRAS , 414, 2005

Cutri R. M. et al., 2003, 2MASS All Sky Catalog of point sources.

Davis M., Nusser A., Masters K. L., Springob C., Huchra J. P., Lemson G., 2011, MNRAS , 413, 2906

de Lapparent V., Geller M. J., Huchra J. P., 1986, ApJL , 302, L1 de Vaucouleurs G., de Vaucouleurs A., Corwin Jr. H. G., 1976, Second reference catalogue of bright galaxies. Containing information on 4,364 galaxies with references to papers published between 1964 and 1975.

Djorgovski S., Davis M., 1987, ApJ , 313, 59

Donley J. L. et al., 2005, AJ , 129, 220

Dressler A., Faber S. M., Burstein D., Davies R. L., Lynden-Bell D., Terlevich R. J., Wegner G., 1987, ApJL , 313, L37

Driver S. P., Popescu C. C., Tuffs R. J., Liske J., Graham A. W., Allen P. D., de Propris R., 2007, MNRAS , 379, 1022

Duffy A. R., Meyer M. J., Staveley-Smith L., Bernyk M., Croton D. J., Koribalski B. S., Gerstmann D., Westerlund S., 2012, MNRAS , 426, 3385

Efstathiou G., 2014, MNRAS , 440, 1138

Einasto J., Joeveer M., Saar E., 1980, MNRAS , 193, 353

Emerson J. P. et al., 2004, in Quinn P. J., Bridger A., eds, Society of Photo-Optical Instrumentation Engineers (SPIE) Conference Series Vol. 5493, Optimizing Scientific Return for Astronomy through Information Technologies. pp 401–410

Erdoğdu P. et al., 2006a, MNRAS , 368, 1515

Erdoğdu P. et al., 2006b, MNRAS , 373, 45

Faber S. M., Dressler A., Davies R. L., Burstein D., Lynden-Bell D., 1987, in Faber S. M., ed., Nearly Normal Galaxies. From the Planck Time to the Present. pp 175–183

Faber S. M., Jackson R. E., 1976, ApJ , 204, 668

Fairall A. P., ed. 1998, Large-scale structures in the universe

Feldman H. A., Watkins R., Hudson M. J., 2010, MNRAS , 407, 2328

Fernie J. D., 1969, PASP , 81, 707

Fisher J. R., Tully R. B., 1981, ApJS , 47, 139

Fixsen D. J., Cheng E. S., Gales J. M., Mather J. C., Shafer R. A., Wright E. L., 1996, ApJ , 473, 576

Focardi P., Marano B., Vettolani G., 1984, A&A, 136, 178

Foreman-Mackey D., Hogg D. W., Lang D., Goodman J., 2013, PASP , 125, 306

Freedman W. L. et al., 2001, ApJ , 553, 47

Giovanelli R., Haynes M. P., 1982, AJ , 87, 1355

Giovanelli R., Haynes M. P., Herter T., Vogt N. P., da Costa L. N., Freudling W., Salzer J. J., Wegner G., 1997, AJ , 113, 53

Giovanelli R., Haynes M. P., Herter T., Vogt N. P., Wegner G., Salzer J. J., da Costa L. N., Freudling W., 1997, AJ , 113, 22

Giovanelli R. et al., 2005, AJ , 130, 2598

Giovanelli R., Haynes M. P., Salzer J. J., Wegner G., da Costa L. N., Freudling W., 1994, AJ , 107, 2036

Han M., 1992, ApJ , 391, 617

Hasegawa T. et al., 2000, MNRAS , 316, 326

Hauschildt M., 1987, A&A, 184, 43

Haynes M. P., Giovanelli R., Chamaraux P., da Costa L. N., Freudling W., Salzer J. J., Wegner G., 1999, AJ , 117, 2039

Haynes M. P. et al., 2011, AJ , 142, 170

Henning P. A. et al., 2017, in American Astronomical Society Meeting Abstracts. p. 137.08

Henning P. A. et al., 2008, in Minchin R., Momjian E., eds, American Institute of Physics Conference Series Vol. 1035, The Evolution of Galaxies Through the Neutral Hydrogen Window. pp 246–248

Henning P. A. et al., 2010, AJ , 139, 2130

Hewett P. C., Warren S. J., Leggett S. K., Hodgkin S. T., 2006, MNRAS , 367, 454

Hinshaw G. et al., 2009, ApJS , 180, 225

Hogg D. W., Bovy J., Lang D., 2010, preprint (arXiv:1008.4686)

Holmberg E., 1958, Meddelanden fran Lunds Astronomiska Observatorium Serie II, 136, 1

Holwerda B. W., Keel W. C., Williams B., Dalcanton J. J., de Jong R. S., 2009, AJ , 137, 3000

Hong T. et al., 2014, MNRAS , 445, 402

Hong T. et al., 2013, MNRAS , 432, 1178

Huchra J. P. et al., 2012, ApJS , 199, 26

Huchra J. P., Vogeley M. S., Geller M. J., 1999, ApJS , 121, 287

Ivezić Ž., Connolly A., Vanderplas J., Gray A., 2014, Statistics, Data Mining and Machine Learning in Astronomy. Princeton University Press

Jacoby G. H. et al., 1992, PASP , 104, 599

Jarrett T.-H., Chester T., Cutri R., Schneider S., Rosenberg J., Huchra J. P., Mader J., 2000, AJ , 120, 298

Jarrett T. H., Chester T., Cutri R., Schneider S., Skrutskie M., Huchra J. P., 2000, AJ , 119, 2498

Jarrett T. H., Chester T., Cutri R., Schneider S. E., Huchra J. P., 2003, AJ , 125, 525

Jarrett T. H. et al., 2007, AJ , 133, 979

Jones D. H. et al., 2009, MNRAS , 399, 683

Jones M. G., Papastergis E., Haynes M. P., Giovanelli R., 2016, MNRAS , 457, 4393

Kannappan S. J., Fabricant D. G., Franx M., 2002, AJ , 123, 2358

Karachentsev I. D., Kaisina E. I., Kashibadze O. G., 2016, ArXiv:1611.02574

Karachentsev I. D., Mitronova S. N., Karachentseva V. E., Kudrya Y. N., Jarrett T. H., 2002, A&A, 396, 431

Kashlinsky A., Atrio-Barandela F., Kocevski D., Ebeling H., 2008, ApJL , 686, L49

Kirby E. M., Jerjen H., Ryder S. D., Driver S. P., 2008, AJ , 136, 1866

Koribalski B. S. et al., 2004, AJ , 128, 16

Kormendy J., Djorgovski S., 1989, ARA&A , 27, 235

Kraan-Korteweg R. C., 2005, in Röser S., ed., Reviews in Modern Astronomy Vol. 18, Reviews in Modern Astronomy. pp 48–75

Kraan-Korteweg R. C., Cameron L., Tammann G. A., 1986, in Madore B. F., Tully R. B., eds, NATO ASIC Proc. 180: Galaxy Distances and Deviations from Universal Expansion. pp 65–72

Kraan-Korteweg R. C., Cameron L. M., Tammann G. A., 1988, ApJ , 331, 620

Kraan-Korteweg R. C., Cluver M. E., Bilicki M., Jarrett T. H., Colless M., Elagali A., Böhringer H., Chon G., 2017, MNRAS , 466, L29

Kraan-Korteweg R. C., Henning P. A., Schröder A. C., 2002, A&A, 391, 887

Kraan-Korteweg R. C., Lahav O., 2000, A&A Rev., 10, 211

Kraan-Korteweg R. C., Riad I. F., Woudt P. A., Nagayama T., Wakamatsu K., 2011, ArXiv e-prints

Kraan-Korteweg R. C., Shafi N., Koribalski B. S., Staveley-Smith L., Buckland P., Henning P. A., Fairall A. P., 2008, Outlining the Local Void with the Parkes HI ZOA and Galactic Bulge Surveys. p. 13

Kraan-Korteweg R. C., Woudt P. A., Cayatte V., Fairall A. P., Balkowski C., Henning P. A., 1996, Nature , 379, 519

Lagattuta D. J., Mould J. R., Staveley-Smith L., Hong T., Springob C. M., Masters K. L., Koribalski B. S., Jones D. H., 2013, ApJ , 771, 88

Lahav O., Lilje P. B., Primack J. R., Rees M. J., 1991, MNRAS , 251, 128

Loeb A., Narayan R., 2008, MNRAS , 386, 2221

Loveday J., 2000, MNRAS , 312, 557

LSST Science Collaboration et al., 2009, ArXiv e-prints

Lucas P. W. et al., 2008, MNRAS , 391, 136

Lynden-Bell D., Faber S. M., Burstein D., Davies R. L., Dressler A., Terlevich R. J., Wegner G., 1988, ApJ , 326, 19

Macri L. M., 2001, PhD thesis, Harvard University

Magoulas C. et al., 2012, MNRAS , 427, 245

Martin A. M., Papastergis E., Giovanelli R., Haynes M. P., Springob C. M., Stierwalt S., 2010, ApJ , 723, 1359

Masters K. L., Crook A., Hong T., Jarrett T. H., Koribalski B. S., Macri L., Springob C. M., Staveley-Smith L., 2014, MNRAS , 443, 1044

Masters K. L., Giovanelli R., Haynes M. P., 2003, AJ , 126, 158

Masters K. L. et al., 2010, MNRAS , 404, 792

Masters K. L., Springob C. M., Haynes M. P., Giovanelli R., 2006, ApJ , 653, 861

Masters K. L., Springob C. M., Huchra J. P., 2008, AJ , 135, 1738

Masters K. L., Springob C. M., Huchra J. P., 2014, AJ , 147, 124

McGaugh S. S., 2005, ApJ , 632, 859

McGaugh S. S., Schombert J. M., Bothun G. D., de Blok W. J. G., 2000, ApJL , 533, L99

McIntyre T. P., Henning P. A., Minchin R. F., Momjian E., Butcher Z., 2015, AJ , 150, 28

Mei S. et al., 2007, ApJ , 655, 144

Meyer M. J. et al., 2004, MNRAS , 350, 1195

Mutabazi T., Blyth S. L., Woudt P. A., Lucey J. R., Jarrett T. H., Bilicki M., Schröder A. C., Moore S. A. W., 2014, MNRAS , 439, 3666

Nagayama T. et al., 2003, in Iye M., Moorwood A. F. M., eds, Proc. SPIEVol. 4841, Instrument Design and Performance for Optical/Infrared Ground-based Telescopes. pp 459–464

Nagayama T. et al., 2004, MNRAS , 354, 980

Nagayama T. et al., 2006, MNRAS , 368, 534

Neill J. D., Seibert M., Tully R. B., Courtois H., Sorce J. G., Jarrett T. H., Scowcroft V., Masci F. J., 2014, ApJ , 792, 129

Nusser A., Davis M., 2011, ApJ , 736, 93

Nusser A., Davis M., Branchini E., 2014, ApJ , 788, 157

O'Neil K., Bothun G. D., Schombert J., 2000, AJ , 119, 136

Opik E., 1922, ApJ , 55, 406

Papastergis E., Martin A. M., Giovanelli R., Haynes M. P., 2011, ApJ , 739, 38

Pastrav B. A., Popescu C. C., Tuffs R. J., Sansom A. E., 2013a, A&A, 553, A80

Pastrav B. A., Popescu C. C., Tuffs R. J., Sansom A. E., 2013b, A&A, 557, A137

Peebles P. J. E., 1980, The large-scale structure of the universe

Peebles P. J. E., 1993, Principles of Physical Cosmology

Pierce M. J., Tully R. B., 1988, ApJ , 330, 579

Pierini D., 1999, A&A, 352, 49

Pizagno J. et al., 2007, AJ , 134, 945

Planck Collaboration et al., 2014a, A&A, 571, A16

Planck Collaboration et al., 2016, A&A, 594, A13

Planck Collaboration et al., 2014b, A&A, 571, A27

Poggianti B. M., 1997, A&AS, 122, 399

Press W. H., Teukolsky S. A., Vetterling W. T., Flannery B. P., 1992, Numerical recipes in FORTRAN. The art of scientific computing

Ramatsoku M., , 2012, MSc thesis, University of Cape Town

Ramatsoku M. et al., 2016, MNRAS , 460, 923

Riad I. F., 2010, PhD thesis, , Univ. of Cape Town, South Africa, (2010)

Riad I. F., Kraan-Korteweg R. C., Woudt P. A., 2010, MNRAS , 401, 924

Riess A. G. et al., 2011, ApJ , 730, 119

Riess A. G. et al., 2016, ApJ , 826, 56

Rizzi L., Tully R. B., Makarov D., Makarova L., Dolphin A. E., Sakai S., Shaya E. J., 2007, ApJ , 661, 815

Rizzi L., Tully R. B., Shaya E. J., Kourkchi E., Karachentsev I. D., 2017, ApJ , 835, 78

Rothberg B., Saunders W., Tully R. B., Witchalls P. L., 2000, ApJ , 533, 781

Said K., Kraan-Korteweg R. C., Jarrett T. H., 2014, SAIP, in press.

Said K., Kraan-Korteweg R. C., Jarrett T. H., 2015, MNRAS , 447, 1618

Said K., Kraan-Korteweg R. C., Jarrett T. H., Staveley-Smith L., Williams W. L., 2016, MNRAS , 462, 3386

Said K., Kraan-Korteweg R. C., Staveley-Smith L., Williams W. L., Jarrett T. H., Springob C. M., 2016, MNRAS , 457, 2366

Sakai S., Mould J. R., Huchra J. P., Hughes S., Macri L. M., Kennicutt Jr. R. C., 2000, in Courteau S., Willick J., eds, Astronomical Society of the Pacific Conference Series Vol. 201, Cosmic Flows Workshop. p. 129

Sault R. J., Teuben P. J., Wright M. C. H., 1995, in Shaw R. A., Payne H. E., Hayes J. J. E., eds, Astronomical Society of the Pacific Conference Series Vol. 77, Astronomical Data Analysis Software and Systems IV. p. 433

Saunders W. et al., 2000, MNRAS , 317, 55

Schechter P., 1976, ApJ , 203, 297

Schlafly E. F., Finkbeiner D. P., 2011, ApJ , 737, 103

Schlegel D. J., Finkbeiner D. P., Davis M., 1998, ApJ , 500, 525

Schmidt M., 1968, ApJ , 151, 393

Schröder A. C., Kraan-Korteweg R. C., Henning P. A., 2009, A&A, 505, 1049

Schröder A. C., Mamon G. A., Kraan-Korteweg R. C., Woudt P. A., 2007, A&A, 466, 481

Scrimgeour M. I. et al., 2016, MNRAS , 455, 386

Silk J., 1997, ApJ , 481, 703

Skrutskie M. F. et al., 2006, AJ , 131, 1163

Sorce J. G. et al., 2013, ApJ , 765, 94

Springob C. M., Haynes M. P., Giovanelli R., Kent B. R., 2005, ApJS , 160, 149

Springob C. M. et al., 2016, MNRAS , 456, 1886

Springob C. M. et al., 2014, MNRAS , 445, 2677

Springob C. M., Masters K. L., Haynes M. P., Giovanelli R., Marinoni C., 2007, ApJS , 172, 599

Staveley-Smith L., Kraan-Korteweg R. C., Schröder A. C., Henning P. A., Koribalski B. S., Stewart I. M., Heald G., 2016, AJ , 151, 52

Staveley-Smith L. et al., 1996, PASA , 13, 243

Strauss M. A., Willick J. A., 1995, Phys. Rep., 261, 271

Sunyaev R. A., Zeldovich Y. B., 1972, Comments on Astrophysics and Space Physics, 4, 173

Tonry J. L., Dressler A., Blakeslee J. P., Ajhar E. A., Fletcher A. B., Luppino G. A., Metzger M. R., Moore C. B., 2001, ApJ , 546, 681

Trumpler R. J., 1930, PASP , 42, 214

Tuffs R. J., Popescu C. C., Völk H. J., Kylafis N. D., Dopita M. A., 2004, A&A, 419, 821

Tully R. B., 1988, Nearby galaxies catalog

Tully R. B. et al., 2013, AJ , 146, 86

Tully R. B., Courtois H. M., Sorce J. G., 2016, AJ , 152, 50

Tully R. B., Fisher J. R., 1977, A&A, 54, 661

Tully R. B., Fisher J. R., 1987, Atlas of Nearby Galaxies

Tully R. B., Pierce M. J., 2000, ApJ , 533, 744

Tully R. B., Pierce M. J., Huang J.-S., Saunders W., Verheijen M. A. W., Witchalls P. L., 1998, AJ , 115, 2264

Tully R. B., Rizzi L., Shaya E. J., Courtois H. M., Makarov D. I., Jacobs B. A., 2009, AJ , 138, 323

Tully R. B., Shaya E. J., Karachentsev I. D., Courtois H. M., Kocevski D. D., Rizzi L., Peel A., 2008, ApJ , 676, 184

Turnbull S. J., Hudson M. J., Feldman H. A., Hicken M., Kirshner R. P., Watkins R., 2012, MNRAS , 420, 447

Valentijn E. A., 1990, Nature , 346, 153

van den Bosch F. C., 2000, ApJ , 530, 177

van Driel W., Schneider S. E., Kraan-Korteweg R. C., Monnier Ragaigne D., 2009, A&A, 505, 29

Verheijen M. A. W., 2001, ApJ , 563, 694

Wang L., Steinhardt P. J., 1998, ApJ , 508, 483

Watkins R., Feldman H. A., 2015, MNRAS , 447, 132

Watkins R., Feldman H. A., Hudson M. J., 2009, MNRAS , 392, 743

Williams W. L., Kraan-Korteweg R. C., Woudt P. A., 2014, MNRAS , 443, 41

Williams W. L., Woudt P. A., Kraan-Korteweg R. C., 2011, Ten years of Infrared Survey Facility and the Future, eds. T. Nagayama, S. Sato, and K. Wakamatsu, 98 (arXiv:1107.1096)

Willick J. A., 1990, ApJL , 351, L5

Woudt P. A., Fairall A., Kraan-Korteweg R. C., Lucey J., Schröder A., Burstein D., McCall M. L., 2005, in Fairall A. P., Woudt P. A., eds, Astronomical Society of the Pacific Conference Series Vol. 329, Nearby Large-Scale Structures and the Zone of Avoidance. p. Fairall

Woudt P. A., Kraan-Korteweg R. C., Fairall A. P., 1999, A&A, 352, 39

Woudt P. A., Kraan-Korteweg R. C., Lucey J., Fairall A. P., Moore S. A. W., 2008, MNRAS , 383, 445

Zwaan M. A., Meyer M. J., Staveley-Smith L., Webster R. L., 2005, MNRAS , 359, L30

Zwaan M. A. et al., 2003, AJ , 125, 2842

Zwaan M. A., van der Hulst J. M., de Blok W. J. G., McGaugh S. S., 1995, MNRAS , 273, L35